PET imaging with zirconium-89 labeled antibodies to guide cancer therapy

Thijs Oude Munnink

CM6.

PET imaging with zirconium-89 labeled antibodies to guide cancer therapy

Thijs Oude Munnink

Stelling n behorende bij het proefschrift van Thijs Oude Munnink:

"PET aging with zirconium-89 labeled antibodies to guide cancer therapy"

1. Moleculaire beeldvorming met gelabelde antilichamen draagt bij aan de ontwikkeling van nieuwe antikankermedicijnen (dit proefschrift).
2. Radioactief gelabelde antilichamen kunnen het effect uitlezen van medicijnen op processen in een tumorcel, door gebruik te maken van een target dat door de cel wordt uitgescheiden, zoals VEGF (dit proefschrift).
3. Het signaal van een tracer die aan een receptor op de celmembraan bindt is afhankelijk van zowel de expressie als de dynamiek van deze receptor (dit proefschrift).
4. Antilichamen dringen binnen in hersenmetastasen (dit proefschrift).
5. Door trastuzumab op kg lichaamsgewicht te doseren wordt bij het gemetastaseerde mammacarcinoom (aanvankelijk) een deel van patiënten onderbehandeld (dit proefschrift).
6. Het niet specifieke Fc-domein van een specifiek therapeutisch antilichaam bepaalt voor een groot deel het gedrag van het antilichaam in mensen.
7. ^{89}Zr-PET tijdens een fase 1 studie met een nieuw antilichaam kan helpen de juiste dosering voor een fase 2 studie te bepalen.
8. Moleculaire beeldvorming tijdens fase 2 studies kan bijdragen aan het identificeren van individuen die het meeste baat zullen hebben en kan zo de kans op een negatieve uitkomst tijdens een fase 3 studie verminderen.
9. Geen enkele tyrosinekinaseremmer of antilichaam is opgenomen op de lijst met essentiële geneesmiddelen van de Wereldgezondheidsorganisatie (versie 2011).
10. Voor 10 miljard USD per jaar (minder dan 0,5% van de jaarlijkse uitgaven aan gezondheidszorg in de VS) kan het wereldwijde aantal sterfgevallen door diarree van 1.390.000 in 2010 worden teruggebracht naar 334.000 in 2015 (Walker et al, PLoS Medicine 2011).
11. De huidige explosieve toename van de wereldbevolking is een demografische transitie tengevolge van een tijdelijke disbalans tussen het aantel geboortes en het aantal sterfgevallen (Bloom, Science 2011).
12. Een te hoge pH in je experiment kan het milieu van een onderzoeker flink zuur maken.
13. Zirconium-89 gelabelde antilichamen zijn 'hot'.

Oude Munnink, Thijs Herman
PET imaging with zirconium-89 labeled antibodies to guide cancer therapy.
Thesis, University of Groningen, The Netherlands

ISBN: 978-90-367-5084-4

Financial support for the research presented in this thesis was granted by the Dutch Cancer Society (grant RUG 2007-3739).

Printing of this thesis was financially supported by: University of Groningen, University Medical Center Groningen, Graduate School for Drug Exploration (GUIDE), Stichting Werkgroep Interne Oncologie, Roche, MSD, Boehringer-Ingelheim, Novartis, Genzyme, GlaxoSmithKline, Amgen BV, IBA Pharma SA, Von Gahlen and Stichting Ina Veenstra-Rademaker.

Pfizer

Cover: The abundant number of new targeted anticancer drugs that are currently in development has been described as a 'tsunami of drugs'. PET imaging might be able to canalize this tsunami of new anticancer drugs by selecting the most promising candidates and by selecting the patients most likely to benefit.

Cover design: Mariëtte Oude Munnink
Printed by: Ipskamp Drukkers, Enschede, The Netherlands

RIJKSUNIVERSITEIT GRONINGEN

PET imaging with zirconium-89 labeled antibodies to guide cancer therapy

Proefschrift

ter verkrijging van het doctoraat in de
Medische Wetenschappen
aan de Rijksuniversiteit Groningen
op gezag van de
Rector Magnificus, dr. E. Sterken,
in het openbaar te verdedigen op
woensdag 5 oktober 2011
om 14.30 uur

door

Thijs Herman Oude Munnink

geboren op 16 februari 1980
te Hengelo (Ov.)

Promotores:	Prof. dr. E.G.E. de Vries
	Prof. dr. R.A.J.O. Dierckx
Copromotores:	Dr. M.N. Lub-de Hooge
	Dr. A.H. Brouwers
	Dr. C.P. Schröder
Beoordelingscommissie:	Prof. dr. E. van der Wall
	Prof. dr. P. Flamen
	Prof. dr. J.H. Beijen

Contents

Paranimfen:
Dr. W.B. Nagengast
Drs. H.M.G. Kooiker

Chapter 1:

General introduction

Background

Cancer treatment strategies consist of surgery, radiotherapy and systemic treatment. Chemotherapeutic drugs aiming directly or indirectly at DNA damage and thereby inducing tumor cell cycle arrest and apoptosis, are the cornerstone of systemic cancer treatment. In addition, nowadays several new systemic therapies arise from research on tumor biology and subsequent drug discovery. Tumor biology research identifies new molecular pathways that underlie uncontrolled tumor growth, invasion and metastasis. These molecular pathways are activated by genetic and epigenetic dysregulation of tumor protein expression and often require a multistep process of sequential alterations in several oncogenes, tumor suppressor genes, or microRNA genes.[1] It is a major challenge and opportunity to translate these findings into new targeted systemic treatments.[2;3] Tumor growth often depends on a few dysregulated growth signaling routes, known as oncogene addiction, and identifying this 'tumor Achilles heel' might potentially reveal the best drug target in the individual patient. One of the proofs of successful Achilles heel targeting is the current treatment for patients with human epidermal growth factor receptor-2 (HER2) positive breast cancer. HER2 is a potent pro-oncogenic factor which is involved in tumor cell survival, proliferation, maturation, metastasis and angiogenesis, and has anti-apoptotic effects. Overexpression of HER2 as a result of *HER2* gene (*HER2/neu* or *c-erbB-2*) amplification has been shown in 20-30% of breast cancer patients and HER2 overexpression is also seen in other tumors, such as gastric and ovarian cancers.[4-6] HER2 overexpression in breast cancer is associated with a worse prognosis and more aggressive clinical behavior, when not specifically treated.[7] These characteristics make HER2 an attractive target for treatment of HER2 positive cancers and have triggered the discovery of HER2 targeting drugs.[6]

Another Achilles heel of most solid tumors is the formation of new blood vessels: angiogenesis.[8] Tumor cells produce and secrete growth factors, like vascular endothelial growth factor (VEGF) and placental growth factor (PlGF). These factors stimulate endothelial cells from the surrounding vasculature to proliferate into a new vascular network for supply of nutrients and energy to facilitate tumor growth. Blocking this formation of tumor vasculature with antiangiogenic drugs can thereby potentially limit tumor growth. Over the last years, several antiangiogenic drugs have been approved for clinical use.[9]

A third major target for cancer therapy is the process of invasion and metastasis. Cancer induced death is mostly caused by metastases. Blocking metastasis might

therefore have a great impact on survival of cancer patients. New insights in the molecular pathways that drive invasion and metastasis of tumor cells have identified several targets for antimetastatic therapy.[10] Among these, transforming growth factor β (TGF-β) has the potential to serve as target for antimetastatic therapy. Inhibition of TGF-β is however explored with caution because of its varying roles in tumor development.[11-14]

In addition to these examples of individual targets for cancer therapy, there is an interest for targeting multiple oncogenic proteins with a single agent. This has become reality by the identification of heat shock protein-90 (HSP90) as a molecular chaperone protein. HSP90 is involved in the conformation, activation, functionality and stability of over hundred (oncogenic) client proteins, making it an attractive candidate for multi-targeted cancer therapy.[15-17]

In parallel with the identification of new drug targets for cancer therapy, advances have been made in biotechnology and high-throughput screening programs that have accelerated drug development enormously. As a result, oncology is a major focus area of pharmaceutical companies.[18] There is a tsunami of new targeted anticancer drug candidates, with currently >800 anticancer drugs in clinical development.[2;19;20] The major challenges now are to identify the best drug candidate(s) in early stages of drug development and to identify the patient (sub)populations most likely to benefit from such an agent. In addition, there is a need for techniques that can rapidly and precisely elucidate the pharmacokinetic and pharmacodynamic profile of new drugs. Molecular imaging, defined as "the visualization, characterization, and measurement of biological processes at the molecular and cellular levels in humans and other living systems",[21] can potentially fulfill, or at least assist in, all these tasks. In oncology, molecular imaging can be performed with several modalities, including radionuclide imaging with positron emission tomography (PET) or single photon emission computed tomography (SPECT), magnetic resonance imaging (MRI) and optical imaging. Molecular imaging can potentially be used for cancer staging and screening[22], translating cancer science[23], and in the discovery, development and evaluation of targeted anticancer drugs.[24-27] Furthermore, molecular imaging can be performed of the whole body at once and repetitively, providing information about (changes in) all organs and tumor lesions over time.

This thesis aims at evaluating the role of molecular imaging with zirconium-89 (^{89}Zr) labeled antibodies in the guidance of targeted anticancer drugs. This

technique, known as immunoPET, has recently become available for clinical use and its applications are progressing rapidly.[28-30]

Outline of the thesis

In chapter 2, the current roles and future potentials of molecular imaging in the treatment of breast cancer patients are described. Data on molecular imaging of breast cancer patients for breast cancer screening, staging, restaging, response evaluation and guiding therapies are reviewed. Most clinical molecular imaging data available cover the visualization of general processes such as glucose metabolism and DNA synthesis. Increasingly more breast cancer specific targets such as the hormone receptors, growth factors and growth factor receptors are being used for molecular imaging, as shown by the results obtained with hormone receptor, VEGF and HER2 imaging.

The molecular imaging data presented in this thesis are all obtained by PET imaging with ^{89}Zr labeled antibodies or antibody fragments. In chapters 3, 4 and 5, this technique is used for monitoring the molecular effects of targeted anticancer drugs *in vivo*, aiming at a better understanding of, and therewith guiding of, these agents. In chapters 6 and 7, PET imaging with ^{89}Zr labeled antibodies is used for monitoring the pharmacokinetics, organ distribution and tumor uptake of the labeled antibodies and to determine the feasibility of molecular imaging with these antibodies.

One of the therapies that may be guided by molecular imaging is HSP90 inhibition. The HSP90 inhibitor NVP-AUY922 downregulates the expression of many oncogenic HSP90 client proteins (including HER2), and inhibits angiogenesis by downregulating hypoxia inducible factor 1α (HIF-1α) resulting in decreased VEGF excretion.[31;32] Therefore HER2 and VEGF downregulation are potential early predictive biomarkers for the response to HSP90 inhibitors. Firstly, the effects of NVP-AUY922 on HER2 and VEGF expression are described in a series of *in vitro* experiments in chapters 3 and 4. Thereafter, the alterations in HER2 and VEGF expression after NVP-AUY922 treatment are evaluated non-invasively *in vivo* with ^{89}Zr-trastuzumab and ^{89}Zr-bevacizumab PET imaging. ^{89}Zr-trastuzumab imaging is used in a human HER2 positive xenograft model and ^{89}Zr-bevacizumab imaging is used in two human HER2 negative xenograft models. PET data are compared with *ex vivo* biodistribution data and immunohistochemistry.

In chapter 5, the development and preclinical use of the ^{89}Zr-labeled F(ab')$_2$ fragment of trastuzumab is studied. ^{89}Zr-trastuzumab-F(ab')$_2$ can visualize rapid treatment effects on the dynamics of HER2 expression. A better understanding of the molecular responses to HER2 targeting drugs like trastuzumab, lapatinib and HSP90 inhibition might contribute to composing the best multi-agent HER2 blockade. HSP90 inhibition, and to a lesser extent, also trastuzumab result in HER2 degradation,[33-35] while lapatinib stabilizes HER2 at the cell membrane.[36] In this chapter, the combined effect of lapatinib and the HSP90 inhibitor 17AAG on HER2 expression, HER2 signaling and cell survival is first evaluated *in vitro* in HER2 positive SKBR3 human breast cancer cells. To allow measurement of rapid changes in HER2 expression by lapatinib or 17AAG, not the antibody but the F(ab')$_2$ fragment of trastuzumab was used for HER2-PET imaging. Suitability of HER2 imaging with ^{89}Zr-trastuzumab-F(ab')$_2$ for HER2 monitoring is first validated in repetitive imaging of untreated mice, followed by imaging experiments with treated mice.

In chapter 6A, the clinical feasibility of HER2 imaging with ^{89}Zr-trastuzumab is presented. Previously, we had performed HER2 imaging with indium-111 (^{111}In) labeled trastuzumab using SPECT. In patients with HER2-positive metastatic breast cancer, this had revealed HER2 specific uptake and newly discovered lesions in 13 of 15 patients.[37] Preclinical evaluation of ^{89}Zr-trastuzumab for HER2-PET, displayed superior image quality and better quantification compared to ^{111}In-trastuzumab, while tumor uptake of ^{89}Zr-trastuzumab and ^{111}In-trastuzumab was comparable.[38] In view of this, we performed a clinical study with ^{89}Zr-trastuzumab PET imaging to determine the required conditions of ^{89}Zr-trastuzumab antibody dose and timing. HER2 positive metastatic breast cancer patients receive 37 MBq ^{89}Zr-trastuzumab at 3 trastuzumab protein doses (10 or 50 mg when trastuzumab naive and 10 mg while on trastuzumab treatment) and undergo ≥ 2 PET-scans around two and five days postinjection. ^{89}Zr-trastuzumab distribution and tumor uptake is visually analyzed. Quantification of ^{89}Zr-trastuzumab levels in liver, bone and brain lesions as well as physiological uptake in liver, spleen, kidneys and brain is performed. Chapter 6B describes the biodistribution findings with ^{89}Zr-trastuzumab HER2-PET in a patient with a high tumor load.

Chapter 7 describes the development and preclinical validation of PET imaging with the ^{89}Zr-labeled TGF-β antibody fresolimumab. TGF-β is a potential drug target for the treatment of cancer,[12] especially in case of highly invasive and

metastatic tumors such as glioblastomas and metastatic breast cancer.[39;40] TGF-β has dual roles in cancer and imaging TGF-β could therefore be of value for patient selection. Development, quality control and preclinical validation of ^{89}Zr-fresolimumab for non-invasive PET imaging of tumor and organ distribution of fresolimumab is performed in several preclinical models, including xenograft models transfected to produce different amounts of human TGF-β and a model of human triple negative metastatic breast cancer.

In chapter 8 the findings of this thesis are summarized, followed by a general discussion with future perspectives of molecular antibody imaging.

References

1. Croce CM. Oncogenes and cancer. N Engl J Med 2008;358:502-11.
2. Schilsky RL. Personalized medicine in oncology: the future is now. Nat Rev Drug Discov 2010;9:363-6.
3. de Bono JS, Ashworth A. Translating cancer research into targeted therapeutics. Nature 2010;467:543-9
4. Moasser MM. The oncogene HER2: its signaling and transforming functions and its role in human cancer pathogenesis. Oncogene 2007;26:6469-87.
5. Hayes DF, Thor AD, Dressler LG, et al. HER2 and response to paclitaxel in node-positive breast cancer. N Engl J Med 2007;357:1496-506.
6. Baselga J, Swain SM. Novel anticancer targets: revisiting ERBB2 and discovering ERBB3. Nat Rev Cancer 2009;9:463-75.
7. Slamon DJ, Clark GM, Wong SG, Levin WJ, Ullrich A, McGuire WL. Human breast cancer: correlation of relapse and survival with amplification of the HER-2/neu oncogene. Science 1987;235:177-82.
8. Kerbel RS. Tumor angiogenesis. N Engl J Med 2008;358:2039-49.
9. Ferrara N, Kerbel RS. Angiogenesis as a therapeutic target. Nature 2005;438:967-74.
10. Chiang AC, Massague J. Molecular basis of metastasis. N Engl J Med 2008;359:2814-23.
11. Massague J. TGFbeta in cancer. Cell 2008;134:215-30.
12. Ikushima H, Miyazono K. TGFbeta signalling: a complex web in cancer progression. Nat Rev Cancer 2010;10:415-24.
13. Padua D, Massague J. Roles of TGFbeta in metastasis. Cell Res 2009;19:89-102.
14. Kelly RJ, Morris JC. Transforming growth factor-beta: a target for cancer therapy. J Immunotoxicol 2010;7:15-26.
15. Taipale M, Jarosz DF, Lindquist S. HSP90 at the hub of protein homeostasis: emerging mechanistic insights. Nat Rev Mol Cell Biol 2010;11:515-28.
16. Workman P, Burrows F, Neckers L, Rosen N. Drugging the cancer chaperone HSP90: combinatorial therapeutic exploitation of oncogene addiction and tumor stress. Ann N Y Acad Sci 2007;1113:202-16.
17. Banerji U. Heat shock protein 90 as a drug target: some like it hot. Clin Cancer Res 2009;15:9-14.
18. Oldham RK, Dillman RO. Monoclonal antibodies in cancer therapy: 25 years of progress. J Clin Oncol 2008;26:1774-7.
19. Alvarez RH, Valero V, Hortobagyi GN. Emerging targeted therapies for breast cancer. J Clin Oncol 2010;28:3366-79

20. Bergh J. Quo vadis with targeted drugs in the 21st century? J Clin Oncol 2009;27:2-5.
21. Mankoff DA. A definition of molecular imaging. J Nucl Med 2007;48:18N, 21N.
22. Frangioni JV. New technologies for human cancer imaging. J Clin Oncol 2008;26:4012-21.
23. Mankoff DA. Molecular imaging as a tool for translating breast cancer science. Breast Cancer Res 2008;10 Suppl 1:S3.
24. McLarty K, Reilly RM. Molecular imaging as a tool for personalized and targeted anticancer therapy. Clin Pharmacol Ther 2007;81:420-4.
25. Eckelman WC, Reba RC, Kelloff GJ. Targeted imaging: an important biomarker for understanding disease progression in the era of personalized medicine. Drug Discov Today 2008;13:748-59.
26. Hargreaves RJ. The role of molecular imaging in drug discovery and development. Clin Pharmacol Ther 2008;83:349-53.
27. de Vries EGE, Oude Munnink TH, van Vugt MATM, Nagengast WB. Toward molecular imaging-driven drug development in oncology. Cancer Discovery 2011;1:25-28.
28. van Dongen GA, Visser GW, Lub-De Hooge MN, de Vries EG, Perk LR. Immuno-PET: a navigator in monoclonal antibody development and applications. Oncologist 2007;12:1379-89.
29. McCabe KE, Wu AM. Positive progress in immunoPET-not just a coincidence. Cancer Biother Radiopharm 2010;25:253-61.
30. van Dongen GAMS, Vosjan MJWD. Immuno-positron emission tomography: shedding light on clinical antibody therapy. Cancer Biother Radiopharm 2010;25:375-85.
31. Eccles SA, Massey A, Raynaud FI, et al. NVP-AUY922: a novel heat shock protein 90 inhibitor active against xenograft tumor growth, angiogenesis, and metastasis. Cancer Res 2008;68:2850-60.
32. Jensen MR, Schoepfer J, Radimerski T, et al. NVP-AUY922: a small molecule HSP90 inhibitor with potent antitumor activity in preclinical breast cancer models. Breast Cancer Res 2008;10:R33.
33. Solit DB, Zheng FF, Drobnjak M, et al. 17-Allylamino-17-demethoxy-geldanamycin induces the degradation of androgen receptor and HER-2/neu and inhibits the growth of prostate cancer xenografts. Clin Cancer Res 2002;8:986-93.
34. Zsebik B, Citri A, Isola J, Yarden Y, Szollosi J, Vereb G. Hsp90 inhibitor 17-AAG reduces ErbB2 levels and inhibits proliferation of the trastuzumab resistant breast tumor cell line JIMT-1. Immunol Lett 2006;104:146-55.

35. Raja SM, Clubb RJ, Bhattacharyya M, et al. A combination of trastuzumab and 17-AAG induces enhanced ubiquitinylation and lysosomal pathway-dependent ErbB2 degradation and cytotoxicity in ErbB2-overexpressing breast cancer cells. Cancer Biol Ther 2008;7:1630-40.
36. Scaltriti M, Verma C, Guzman M, et al. Lapatinib, a HER2 tyrosine kinase inhibitor, induces stabilization and accumulation of HER2 and potentiates trastuzumab-dependent cell cytotoxicity. Oncogene 2009;28:803-14.
37. Perik PJ, Lub-De Hooge MN, Gietema JA, et al. Indium-111-labeled trastuzumab scintigraphy in patients with human epidermal growth factor receptor 2-positive metastatic breast cancer. J Clin Oncol 2006;24:2276-82.
38. Dijkers ECF, Kosterink JG, Rademaker AP, et al. Development and characterization of clinical-grade ^{89}Zr-trastuzumab for HER2/*neu* immunoPET imaging. J Nucl Med 2009;50:962-9.
39. Wick W, Naumann U, Weller M. Transforming growth factor-beta: a molecular target for the future therapy of glioblastoma. Curr Pharm Des 2006;12:341-9.
40. Korpal M, Kang Y. Targeting the transforming growth factor-beta signalling pathway in metastatic cancer. Eur J Cancer 2010; 46:1232-40.

Chapter 2:

Molecular imaging of breast cancer

Thijs Oude Munnink[1]
Wouter Nagengast[1]
Adrienne Brouwers[2]
Carolina Schröder[1]
Geke Hospers[1]
Marjolijn Lub-de Hooge[2,3]
Elsken van der Wall[4]
Paul van Diest[5]
Elisabeth de Vries[1]

Departments of Medical Oncology[1], Nuclear Medicine and Molecular Imaging[2], Hospital and Clinical Pharmacy[3], University Medical Center Groningen, Groningen, The Netherlands; Departments of Medical Oncology[4], Pathology[5], University Medical Center, Utrecht, The Netherlands

Breast 2009;18(S3):S66-S73

ABSTRACT

Molecular imaging of breast cancer can potentially be used for breast cancer screening, staging, restaging, response evaluation and guiding therapies.

Techniques for molecular breast cancer imaging include magnetic resonance imaging (MRI), optical imaging, and radionuclide imaging with positron emission tomography (PET) or single photon emission computed tomography (SPECT). This review focuses on PET and SPECT imaging which can provide sensitive serial non invasive information of tumor characteristics.

Most clinical data are gathered on the visualization of general processes such as glucose metabolism with the PET-tracer [^{18}F]fluorodeoxyglucose (FDG) and DNA synthesis with [18F]fluoro-L-thymidine (FLT).

Increasingly more breast cancer specific targets are imaged such as the estrogen receptor (ER), growth factors and growth factor receptors. Imaging of the ER with the PET tracer 16-α-[^{18}F]fluoro-17-β-estradiol (FES) has shown a good correlation between FES tumor uptake and ER density. ^{111}In-trastuzumab SPECT to image the human epidermal growth factor receptor 2 (HER2) showed that in most patients with metastatic HER2 overexpressing disease more lesions were detected than with conventional staging procedures. The PET tracer ^{89}Zr-trastuzumab showed excellent, quantifiable, and specific tumor uptake. ^{111}In-bevacizumab for SPECT and ^{89}Zr-bevacizumab for PET-imaging have been developed for vascular endothelial growth factor (VEGF) imaging as an angiogenic marker. Lastly, tracers for the receptors EGFR, IGF-1R, PDGF-βR and the ligand TGFβ are under development.

Although molecular imaging of breast cancer is still not commonly used in daily clinical practice, its application portfolio is expanding rapidly.

INTRODUCTION

Current screening and staging techniques for breast cancer give a non-perfect diagnostic yield.[1] In addition, optimal treatment with targeted therapies often requires knowledge about the expression of their targets within the tumor lesions. Molecular imaging of tumor metabolism, proliferation and other more tumor specific targets may therefore be of additional value in breast cancer management. It can potentially be used for breast cancer screening, staging, restaging, response evaluation and guiding surgery, radiotherapy and systemic treatment. Additionally, molecular imaging can be a useful tool in targeted drug development and for translating breast cancer science.[2;3]

Molecular imaging has been defined by the Society of Nuclear Medicine as "the visualization, characterization and measurement of biological processes at the molecular and cellular levels in humans and other living systems".[4] Molecular imaging of breast cancer is an emerging field. It can be performed with various imaging modalities. Ligands used for this purpose can be labeled with either a contrast agent for magnetic resonance imaging (MRI), a fluorescent dye for optical imaging, a positron emitting radionuclide for positron emission tomography (PET) or a gamma emitting radionuclide for single photon emission computed tomography (SPECT) imaging. This review will focus on PET and SPECT molecular breast cancer imaging given the high sensitivity of nuclear imaging, with up to 1 million times more sensitive in detecting molecular probes than other imaging modalities, and available results.

Both PET and SPECT molecular imaging are based on the detection of radiolabeled (tumor specific) ligands. Radioisotopes are chosen based on the proposed imaging modality, PET or SPECT, and the physical half-life of the radioisotope ideally should match the biological half-life of the ligand. Radioisotopes used for PET imaging (e.g. ^{18}F, ^{11}C, ^{15}O, ^{13}N, ^{64}Cu, ^{124}I, ^{89}Zr) emit positrons during radioactive decay. After combining with an electron, the positron and electron are annihilated and their combined masses are converted into two gamma photons of 511 keV each, emitted in 180^0 opposite directions. The photons thus produced, are available for detection by a PET camera, in which two paired detectors both register a photon simultaneously (coincidence detection). Radioisotopes used in SPECT imaging (^{111}In, ^{99m}Tc, $^{123/131}I$) emit single gamma photons which can be detected with a gamma camera. As single photons offer no information about the direction of travel, the direction of detected photons is fixed by using a collimating lead filter (collimator). This collimator has small

parallel holes which reject the photons not traveling perpendicular to the detector surface. SPECT imaging uses rotating gamma camera heads for acquiring multiple 2D projections, and a computer algorithm for reconstruction to 3D images. The relatively limited sensitivity of SPECT reduces its statistical strength for quantitative interpretation. However in general, SPECT is a less expensive technique than PET and in addition, SPECT isotopes are more widely available than PET isotopes.

For breast cancer molecular imaging, several tumor characteristics are candidates for development of tumor specific tracers (Fig 1). To target general phenomena one can visualize the tumor cell glucose metabolism or DNA synthesis, which are both increased in tumor cells compared to normal cells. Most breast cancers express hormone receptors in the tumor cell, making these receptors interesting targets for imaging in these subsets of patients. Also receptors present at the tumor cell membrane, such as human epidermal growth factor receptor 2 (HER2), epidermal growth factor receptor (EGFR), insulin-like growth factor-1 receptor (IGF-1R) and platelet derived growth factor-β receptor (PDGF-βR), may be of interest for imaging. In addition, tumor cells excrete growth factors, like vascular endothelial growth factor (VEGF) and transforming growth factor-β (TGF-β), in the tumor microenvironment and therefore are tracer target

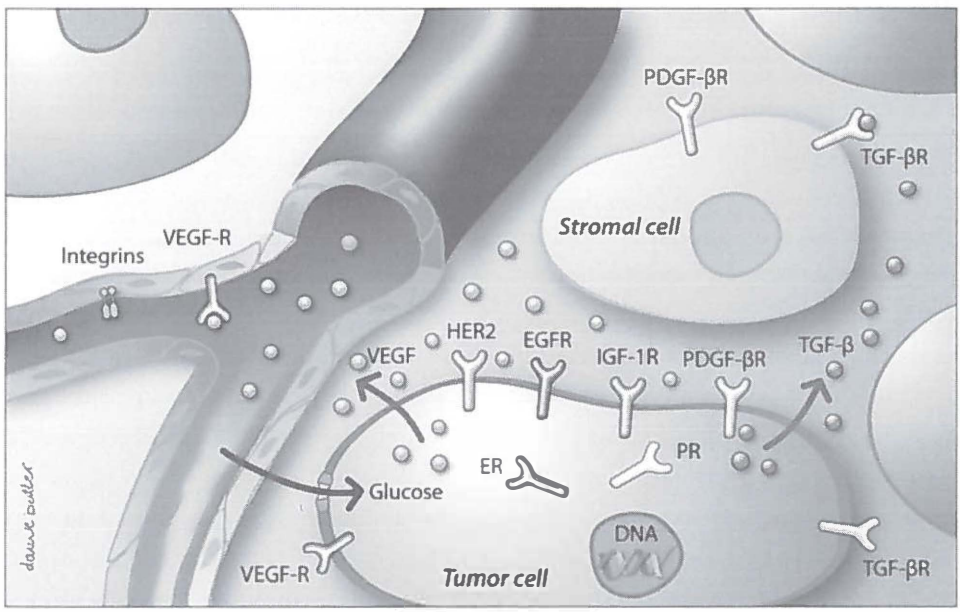

Figure 1. Schematic presentation of the (potential) targets for breast cancer molecular imaging. See page 166 for full color image.

candidates. Finally, all targets involved in angiogenesis (VEGF-receptors, $\alpha v\beta_3$ integrin, fibronectin, endostatin) and hypoxia can be used, since both processes are key players in tumor growth generally not occurring in normal breast tissue.

FDG-PET breast cancer imaging

The best studied and clinically most used PET-tracer is [^{18}F]fluorodeoxyglucose (FDG).[5] FDG-PET visualizes glucose metabolism, which is often increased in tumor cells compared to normal cells. FDG is transported across the cell membrane by glucose transporter proteins and is phosphorylated by hexokinases to FDG-6-phosphatase. Because FDG-6-phosphate lacks a hydroxyl group in the 2-position, unlike glucose-6-phosphate, it is not further metabolized and thus 'trapped' in the cell. This results in a tumor accumulation of FDG, which is regulated by the activity of the glucose transporters and hexokinase. During the process of tumor accumulation, FDG is cleared from the blood by the kidneys resulting in low blood levels.[6] Usually 45-90 minutes after FDG injection, the tumor uptake can be detected with a PET camera (Fig. 2A). Under physiological conditions, FDG predominantly accumulates in tissues with high glucose metabolism, such as the brain. Less uptake is seen in muscle, myocardium, liver, intestine and kidneys. Limited anatomical information by FDG-PET alone is increasingly improved by fusing the separately recorded PET images with computed tomography (CT) or magnetic resonance imaging (MRI), and by fusing the images recorded by integrated PET-CT cameras.[7;8]

FDG-PET has been evaluated for primary tumor detection and diagnosis, (re)staging of locoregional and distant metastases and monitoring therapy response. In a pre-operative setting, high FDG tumor uptake was observed particularly in ductal carcinomas.[9] The degree of FDG tumor uptake was positively correlated with grade, Ki-67 proliferation index,[9;10] mitotic index, Glut-1 expression, amount of necrosis, number of tumor cells/volume, hexokinase I expression and microvessel density.[11] However, FDG uptake itself is not tumor-specific, and the distinction between malignant and benign breast cells can be difficult, particularly in situations of breast hypermetabolism (breast feeding, mastitis).[12;13] Also, false positive results can be due to the accumulation of FDG in activated inflammatory cells such as granulocytes and macrophages.[14]

For early breast cancer detection and diagnosis, the ability to detect non-palpable, small (<1.0 cm) malignancies is desirable. The spatial resolution of previous

generation clinical PET camera is >7 mm, depending on positron range, and therefore whole body FDG-PET has not extensively been used for this purpose.[5;15] In the latest generation PET/CT cameras, spatial resolution has improved to ≤ 4 mm for [^{18}F].

High resolution, high sensitive positron emission mammography (PEM) has been developed for early stage breast cancer detection and diagnosis. This technique consists of two planar detectors placed opposite a gently compressed breast and is capable of detecting primary breast cancers lesions as small as 3 mm.[16] PEM results were correlated with histopathology for 92 lesions in 77 patients, and a sensitivity of 90% and a specificity of 86% for detecting primary breast cancers was found. In the same study, PEM detected 5 of 8 lesions smaller than 1 cm in patients with biopsy proven breast cancer or suspicious breast lesions.[17] Its clinical utility for screening or as adjunct to mammography has to be proven in larger series.[18;19]

The role of FDG-PET for staging, including detection of tumor involvement in regional lymph nodes and distant metastases, has recently been reviewed.[20] It cannot replace histological staging for axillary staging, since its sensitivity varied from 20-94% in 20 studies with a specificity of 85-100%.[21;22]

A number of studies addressed the role of FDG-PET for detecting distant metastases and disease recurrence. Specificity varied from 100% to as low as 20%, while sensitivity was consistently high, ranging from 78-100%.[20] The sensitivity may vary with tumor biological characteristics. Overall acceptable and generally superior sensitivity is reported for FDG-PET compared to conventional imaging (mammography, ultrasonography, CT, MRI, radiography and bone scintigraphy) in the detection of local recurrence or distant metastatic disease.[19;23-26] For the detection of bone metastases, particularly osteolytic or mixed type, FDG-PET can perform better than conventional bone scintigraphy.[27] FDG-PET detects osteolytic metastases often missed by bone scintigraphy, while FDG-PET often misses osteoblastic metastases, for which bone scintigraphy has higher sensitivity.[28;29] It appears that FDG-PET is complementary to bone scintigraphy, which remains the standard for detecting bone metastases in breast cancer.[30] For patients with inflammatory breast cancer, it was suggested that FDG-PET/CT should be considered for initial staging because it provides additional information on distant metastases.[31]

Guidelines in general advice a relatively modest use of FDG-PET. The National Comprehensive Cancer Network (NCCN) Practice Guidelines in Oncology (v.1.2009) advice not to use FDG-PET for breast cancer staging in general, but apply it in case of those clinical situations with locally advanced or metastatic disease where other staging studies are equivocal or suspicious.[32] Others also do not recommended FDG-PET for routine breast cancer staging.[20] The "Recommendations on the use of FDG-PET in oncology" panel chaired by the American Society of Clinical Oncology (ASCO) concluded that it should be routinely added to the conventional work-up in detecting metastatic or recurrent breast cancer in those patients clinically suspected of metastases or recurrence.[5]

Assessment of the change in tumor burden, either by tumor size or by tumor functionality, is important for the clinical evaluation of cancer therapeutics. In 2000, the Response Evaluation Criteria in Solid Tumors (RECIST) guideline for the assessment of tumor size changes included imaging with X-ray, CT or MRI for response monitoring.[33] In the recently updated RECIST guideline (version 1.1), FDG-PET is included and mentioned to be able to complement CT to assess progression. In addition, it is now suggested to use FDG-PET in circumstances where it is difficult to distinguish residual disease from normal (scar) tissue.[34]

Thresholds ranging from 20-70% decrease of the standardized uptake value (SUV) are used for FDG tumor uptake as response evaluation.[35;36] The appropriate percentage SUV decrease threshold depends among others on technical and clinical factors differing between studies and institutions.[37] For early effect assessment on chemotherapy after one cycle for example, smaller SUV threshold values are used then for late assessment. There is no standardized protocol with a SUV cut-off value that is generally accepted to implicate a response. In the neo-adjuvant setting (n=64), changes in FDG tumor uptake between baseline and after 1, 2, 3 and 6 cycles of chemotherapy was compared with pathologic response at surgery after the sixth cycle. In patients with a histological total or near-total therapeutic effect, decrease in FDG uptake increased after each cycle of chemotherapy. The average decrease in FDG uptake after 1, 2, 3 and 6 cycles was 59.6, 78.7, 86.3 and 90.2% in this group, respectively. In patients with histological no and less than 50% therapeutic effect, FDG uptake was only decreased to an average of 53.2% after six cycles of chemotherapy.[38] In another neo-adjuvant study, FDG-PET was performed at baseline and after the first and second chemotherapy cycle. Twenty-four of 104 patients had a low baseline SUV (< 3.0), and none of them experienced a histopathological response to chemotherapy,

defined as minimal residual disease. In patients with a baseline FDG SUV >3.0, histopathological responders showed an average decrease of 51% in FDG uptake, while non-responders showed an average decrease of 37% (P=0.01).[39] In addition, the FDG SUV decrease after the first cycle was a predictive factor for a pathologically proven complete response (pCR) as a SUV decrease >60% predicted the pCR with an accuracy of 87%.[40] Others showed similar results in 30 primary and metastatic breast cancer patients.[41] In a neo-adjuvant setting (n=96), decrease in FDG uptake after chemotherapy in the subset of patients with low baseline FDG uptake (n=57), could not predict histopathological tumor response. In the subset of patients with high baseline FDG uptake (n=39), there was a clear and significant difference between the FDG decrease for the high and low histopathological tumor response categories.[42] Increased metabolic activity, or 'metabolic flare', detected by FDG-PET in response to hormonal treatment was predictive for tumor response and overall survival.[43-45]

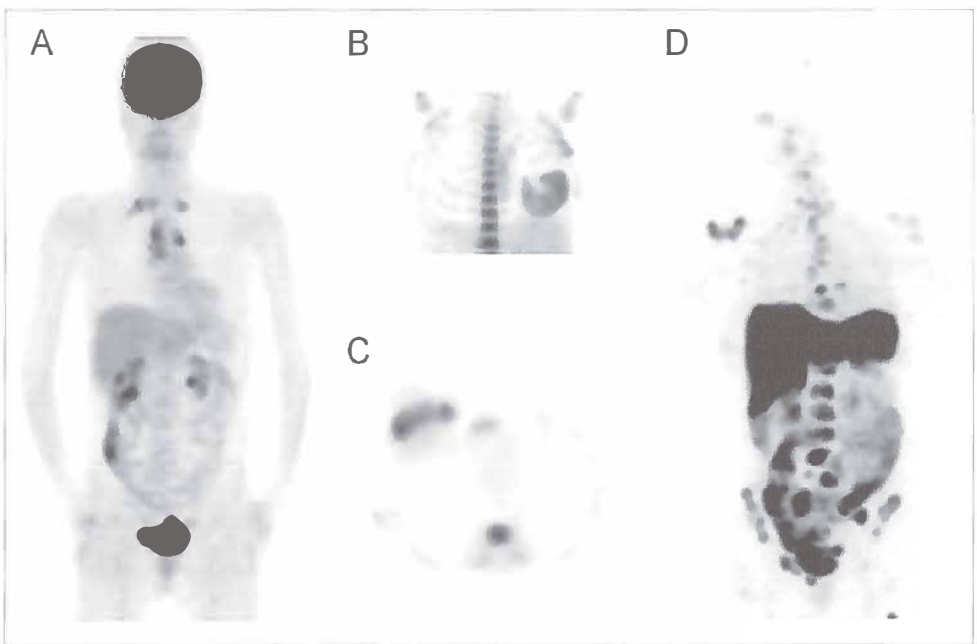

Figure 2. Examples of three breast cancer patients imaged with various PET tracers. FDG-PET shows physiological FDG uptake in brain, bladder, kidneys, liver, intestine and muscles, and pathological FDG uptake supraclavicular and mediastinal metastatic lesions (A). FLT-PET shows physiological FLT uptake in liver and bone marrow, and pathological FLT uptake in primary tumor (B, C). FES-PET shows physiological FES uptake in liver and intestine, and pathological FES uptake in numerous bone metastases (D).

Few small studies addressed the prognostic role of FDG-PET for chemotherapy outcome. A superior predictive value of complete metabolic response measured with FDG-PET before- and one month after completion of chemotherapy, as compared with conventional imaging techniques, has been reported. Mean survival was 10 months in patients without metabolic response (n=13), versus 24 months with metabolic response (n=34). In patients with response measured by conventional imaging (n=31), median survival was 21 months, versus 10 months in non-responders.[46] Preoperative FDG tumor uptake after neo-adjuvant chemotherapy (n=40) was inversely associated with disease free but not with overall survival.[47] FDG tumor uptake before primary breast surgery correlated with prognostic parameters such as tumor size, axillary lymph node status, histological type, histological grade, ER status, p53 and Ki-67 expression.[48;49]

In conclusion: in clinical practice FDG-PET is not recommended as a standard procedure for breast cancer diagnosis and staging. The use of FDG-PET in detection of breast cancer recurrence and metastasis can be of value, especially in patients at high risk. Information on its role in evaluation and prediction of treatment response is increasing, but FDG-PET is not recommended as a routine assessment yet.

FLT-PET breast cancer imaging

The pyrimidine analogue PET-tracer [^{18}F]fluoro-L-thymidine (FLT) has been developed to image increased DNA synthesis, as FLT tumor uptake reflects the proliferation rate of tumor cells (Fig. 2B,C). Normal physiological uptake of FLT is seen in liver, bone marrow and the urine tract. In breast cancer patients, small studies have been performed for staging and as early predictive marker of response to chemotherapy. FLT uptake was seen in 8 out of 10 primary breast tumors and some large axillary lymph node metastases, but small axillary lymph node metastases were not detected.[50] Slightly better results were seen in another report in 12 patients, where 13 out of 14 primary breast tumors and 7 out of 8 axillary lymph node metastases could be detected.[51] Experience with FLT-PET for early response prediction is limited. FDG and FLT were compared for monitoring and predicting tumor response to chemotherapy in 14 patients with primary or metastatic breast cancer. A strong correlation was found between the percentage decrease in FLT tumor uptake 2 weeks after initiation of chemotherapy and late CT (average interval 3.3 months) size changes. No correlation was found between

FDG uptake changes over the first 2 weeks and these response measurements.[52] Similar results were obtained when FLT-PET was performed already one week after initiation of chemotherapy.[53]

Overall, FLT-PET is not regarded as an routine staging tool for breast cancer but may play a role in prediction of response to therapy.[54]

Hormone receptor imaging

At diagnosis, 70% of the breast cancer patients have tumors positive for hormone receptors of which the majority are positive for estrogen receptor (ER). Furthermore, >95% of progesterone receptor (PR) positive tumors are also ER positive. Immunohistochemical determination of ER and PR expression at the time of primary diagnosis is part of standard care. Treatment strategies are based on hormone receptor expression, which is predictive of response to anti-hormonal treatment in up to 70% of patients with a new diagnosis of breast cancer. The guidelines of the PDQ, the National Comprehensive Cancer Network (NCCN) and the European Society for Medical Oncology (ESMO) indicate that new histology has to be considered at relapse,[32;55;56] as hormone receptor expression can vary between primary tumor and recurrence in ~30% of cases.[57;58] In one study, the discordance between the ER-status of the primary tumor and the distant metastases was 41% for bone marrow metastases, and 44% for liver metastases.[59] Obtaining tumor tissue at relapse may be cumbersome. Also, sampling error may be a potential problem, as ER expression can differ between primary tumor and synchronous metastases. In addition, anti-hormonal treatment induces ER loss in a number of patients with acquired hormonal resistance.[60]

The PET tracer 16-a-[^{18}F] fluoro-17-β-estradiol (FES) was developed as a receptor ligand for ER (Fig. 2D) and binds to both subtypes ERα and ERβ, with a preference for ERα.[61] Several studies with FES-PET have been performed in breast cancer patients. FES tumor uptake was shown to correlate with immunohistochemical ER tumor density.[62-65] These studies pointed to the potential role of FES-PET in the assessment of ER status, especially in patients with multiple tumors or tumors that are difficult to biopsy, and in the guidance of anti-hormonal therapies. Comparison of FES and FDG tumor uptake with ER status in 43 patients, showed an 88% overall agreement between FES uptake and

ER status. However, no correlation was found between FDG uptake and ER status or between FES and FDG uptake.[62]

With regard to predicting and monitoring of response to anti-hormonal therapy, few data are available.[43-45;66;67] FES-PET was evaluated in 47 patients with immunohistochemically ER positive recurrent or metastatic tumors. FES-PET was performed at baseline prior to, or shortly after the initiation of anti-hormonal therapy, consisting of tamoxifen, aromatase inhibitor or aromatase inhibitor with fulvestrant. FES tumor uptake at baseline was compared with the response after 6 months therapy, determined by a combination of clinical assessment and modified RECIST criteria. In patients with low FES tumor uptake at baseline (n=15), no response was shown. In the group with a high uptake at baseline, 11 of 32 patients responded to anti-hormonal therapy. Particularly patients with HER2 co-expression (n=10) did not show an objective treatment response, in spite of high FES uptake at baseline.[67]

With regard to the prognostic value of FES-PET, no data are available yet. So far, no validated tracer is available for imaging PR.[68]

In conclusion, thus far FES-PET cannot be regarded as a routine imaging technique for the workup of a breast cancer patient. However, it is certainly a technique that deserves to be explored more extensively, particularly with regard to predicting treatment response.

HER2 imaging

HER2 is encoded for by the *HER2* proto-oncogene (HER2/*neu* or c-erbB-2) and is involved in tumor cell survival, proliferation, maturation, metastasis and angiogenesis, and has anti-apoptotic effects. Overexpression of HER2, the result of *HER2* gene amplification, is present in 25-30% of breast cancer patients.[69;70] Trastuzumab is a recombinant IgG1 monoclonal antibody targeting the extracellular domain of HER2 and is widely used clinically in patients with HER2 overexpressing breast cancer.

HER2 tumor expression can vary during treatment and can differ across metastatic lesions within a patient.[71-75] Therefore, there is a need for methods that are able to assess the HER2 status repeatedly, preferable in all lesions and non-invasively. HER2 imaging could potentially serve this aim.

HER2 imaging starts with selecting a suitable HER2 targeting ligand. Currently available HER2 targeted ligands includes full length monoclonal antibodies, Fab-fragments, F(ab')$_2$-fragments, diabodies, minibodies, affibodies, scFv-Fc and peptides. When radiolabeling these HER2 targeted molecules, the physical half-life of the radio isotope ideally should suit the biological half-life of the HER2 targeting molecule to allow imaging at the optimal time-point. This implicates that full-length monoclonal antibodies are mostly radiolabeled with long-lived isotopes while the smaller HER2 targeting molecules, which have a more rapid clearance, are radiolabeled with shorter-lived isotopes. Full-length HER2 monoclonal antibodies have been labeled with ^{131}I, ^{111}In and ^{99m}Tc for HER2-SPECT/gamma camera imaging and with ^{124}I, ^{86}Y, ^{76}Br and ^{89}Zr for HER2-PET. The smaller HER2 targeting antibody fragments, proteins and peptides have been labeled with ^{111}In, ^{131}I and ^{99m}Tc for HER2-SPECT/gamma camera imaging and with ^{18}F, ^{68}Ga, ^{64}Cu, ^{124}I and ^{76}Br for HER2-PET.[76]

We have performed ^{111}In-trastuzumab planar gamma camera and SPECT imaging in HER2 positive metastatic breast cancer patients. With this technique, 45% of single tumor lesions, detected with conventional imaging, could be shown. In addition, new tumor lesions were discovered in 13 of 15 patients.[77] Since PET imaging provides a higher spatial resolution, a better signal-to-noise ratio and is potentially more quantitative than SPECT, we have developed ^{89}Zr-trastuzumab for HER2-PET.[78] Preliminary data of the clinical evaluation of this tracer in metastatic breast cancer patients shows excellent tracer uptake in the tumors and the successful detection and quantification of HER2 positive breast cancer metastases.

HER2-PET may also be useful for pharmacodynamic evaluation of HER2 down-regulating therapies. Heat shock protein-90 (HSP90) is a molecular chaperone protein which is involved in the conformation, activation, functionality, and stability of over hundred client proteins. Client proteins of HSP90 include the key regulator of VEGF expression HIF-1α, HER2, hormone receptors and others.[79] Treatment with HSP90 inhibitors results in HER2 downregulation. This rapid but transient HER2 downregulation has been shown in several preclinical reports, both in vitro and in vivo.[80-83] The pharmacodynamics of HER2 downregulation induced by HSP90 inhibition with 17AAG were visually and quantitatively evaluated by PET in an HER2 overexpressing xenograft model with a ^{68}Ga labeled F(ab')$_2$ fragment of trastuzumab. HER2-PET imaging with this fragment was able to quantify the HER2 response as a 50% lower tracer tumor uptake after 17AAG

treatment,[84] while FDG tumor uptake was unaffected during the 21 days follow-up period.[85] We showed a 41% decrease of ^{89}Zr-trastuzumab uptake by the new HSP90 inhibitor NVP-AUY922 in a tumor xenograft.[86]

In summary, preclinical results with HER2 imaging are abundant and promising but clinical experience is limited. Our findings with clinical HER2-SPECT and -PET imaging with ^{111}In-trastuzumab and ^{89}Zr-trastuzumab in metastatic breast cancer advocate the further development and exploration of the possibilities of this technique.

VEGF imaging

The development of vascular supply, usually called angiogenesis, is important for the growth of tumors. One of the most important factors involved in angiogenesis is vascular endothelial growth factor (VEGF). In tumor cells there is an unproportional upregulation of VEGF production which leads to locally high VEGF levels, mainly located in the extracellular matrix.

In metastatic breast cancer the addition of bevacizumab, a humanized monoclonal antibody which neutralizes all isoforms of VEGF-A, to paclitaxel leads to an increased response rate and increased progression free survival.[87]

To select patients who could benefit from VEGF targeted therapies, and to follow up new treatment regimes, imaging of VEGF using specific tracers, is of great interest. It is an important downstream protein produced as a result of multiple processes (hypoxia), activation of growth factor receptors (EGFR, HER2) and intracellular proteins (HIF-1α, mTOR etcetera).

To date, several radiolabeled anti-VEGF antibodies and Fab-fragments have been used for the development of VEGF imaging namely VG76e, HumMV833, bevacizumab and ranibizumab.[88-90] ^{125}I- and ^{124}I-labeled VG76e, an IgG1 mouse monoclonal anti-VEGF antibody, showed specific tumor targeting in a human fibrosarcoma xenograft mouse model.[90] ^{124}I-HuMV833 PET scans in 20 patients with progressive solid tumors, showed highly variable uptake between and within patients. For example, there was high ^{124}I-HuMV833 uptake in an ovarian tumor and low uptake in a poorly vascularized colon cancer metastasis.[89]

We developed several tracers for VEGF-PET and -SPECT imaging. MicroPET imaging in a human ovarian xenograft model using ^{89}Zr labeled bevacizumab showed clear and specific tumor localization 72 h postinjection with maximal

uptake after 168 h.[88] ^{89}Zr-bevacizumab tumor uptake could be quantified non-invasively, allowing follow-up of VEGF secretion during therapy. Comparable results were seen using ^{89}Zr- and ^{18}F labeled ranibizumab, a Fab-fragment binding to VEGF. Fast distribution and clearance of the Fab-fragment allowed to acquire images earlier, namely already 3 h after tracer injection, although absolute tumor uptake of the Fab-fragment is lower compared to bevacizumab. This makes the Fab-fragment tracer attractive to follow up rapid changes of VEGF secretion following therapy.[91] SPECT imaging using ^{111}In labeled bevacizumab revealed tumor lesions in both melanoma and metastatic colon cancer patients.[92] Future studies, should further elucidate the role of VEGF-imaging in the assessment of response evaluation of new molecular targeted therapies.

Screening mammography is the single most effective breast cancer screening method. Magnetic resonance imaging (MRI) has additionally a role in high risk individuals. However, the sensitivity and specificity of these techniques is not optimal. Therefore, in addition to not detecting all breast tumors, also a significant proportion of false positive tests occur. In the United States, 11% of mammograms require additional evaluation while the lesion turns out to be benign in more than 90% of cases.[93] False positive readings are more common in younger women, both because the tests are less specific and because breast cancer is less common.[94;95] More tumor specific ways of detecting breast lesions, are clearly desired in the setting of early diagnosis. Increased vascularization is present in all pre-invasive lesions, ductal as well lobular, and increases with lesion severity. Also, immunohistochemically determined VEGF expression in normal glandular structures is lower than in lesions, with the highest levels found in ductal lesions.[96] Non-invasive assessment of VEGF-levels in the micro-environment of pre-malignant or malignant breast tumor by VEGF imaging could potentially be used as screening tool. The presence of high VEGF levels in the extra cellular matrix can magnify the tumor tracer uptake and might well make detection of small lesions possible.

Another way of imaging angiogenesis is to visualize the $\alpha v\beta_3$ integrin receptor. Recently, two studies reported about PET tracers based on the $\alpha v\beta_3$ targeting Arg-Gly-Asp (RGD) tripeptide. In 7 metastatic breast cancer patients, RGD-PET with ^{18}F-AH111585 visualized all 18 lesions shown on CT. Uptake of ^{18}F-AH111585 in tumor was either homogeneous or appeared within the tumor rim.[97] In 16 patients with primary or metastatic breast cancer, RGD-PET with ^{18}F-Galacto-

RGD identified all invasive carcinomas but lymph-node metastases were only seen in 3 of 8 patients.[98]

Other targets for molecular breast cancer imaging

Breast cancers that are negative for ER, PR and HER2 immunohistochemically, known as triple-negative breast cancer, have a poor prognosis.[99-101] Much research is ongoing to identify the biological processes and targets that drive triple-negative breast cancer. Molecular imaging of these targets could have a role in target identification, drug development and response prediction and evaluation.

Overexpression of EGFR is seen in 57% of triple negative breast cancers. The EGFR directed monoclonal antibody cetuximab is currently in clinical investigation for the treatment of triple-negative breast cancer.[102] Several tracers have been developed for EGFR imaging, such as radiolabeled EGFR tyrosine kinase inhibitors and the EGFR ligand epidermal growth factor or EGFR antibodies.[103] Recently, also the IGF-1R has been identified as a possible target for treatment of triple-negative breast cancer[104] because many of these tumors express IGF-1R and tracers for imaging IGF-1R are underway.[105] In breast cancer, the crucial orchestrating role of TGF-β in the metastasising processes becomes more and more evident[106] and TGF-β and TGF-βRs targeting therapies are currently in clinical trials. Imaging TGF-β could help to select patients most likely to benefit from TGF-β targeting therapies and to monitor TGF-β targeting therapies.

PDGF-βR is commonly expressed in malignant breast tissue and surrounding peri-epithelial stromal cells.[107] PDGF-βRs are pivotal in peritumoral vasculature, stroma and bone. The receptor and its downstream effectors trigger a cascade that regulates cell proliferation, differentiation, and survival.[108] Increased PDGF-βR signaling is required for formation of breast cancer metastases.[109] Therefore, the visualization of this receptor can possibly contribute to improved breast cancer staging. A possible strategy to perform this, is by radiolabeling a construct with the PDGF-βR homing peptide pPB.[110]

Discussion and future direction

Although molecular imaging of breast cancer is still not commonly used in daily clinical practice, its application portfolio is expanding rapidly and it thereby holds promise for improving breast cancer management. We addressed results

with the sensitive PET and SPECT techniques, but these techniques do have limitations, especially for screening purposes, caused by the exposure to ionizing radiation, limited capacity and the limited spatial resolution of currently used systems which hinders early tumor detection. Resolution of the latest generation PET and SPECT cameras has improved and the introduction of combined systems with an integrated CT (and soon also MRI) system has led to a much better (anatomic) interpretation of the data. In addition to this integration of imaging modalities, also the indirect combination of nuclear imaging and optical imaging could serve shared purposes. Optical contrast agents (tracers) that target specific molecular changes associated with breast cancer formation as well as clinical optical breast imaging equipment are under development, primarily for breast cancer screening.[111] In case of optical imaging, no ionizing radiation is needed and the technique is relatively inexpensive, which are significant advantages for breast cancer screening purposes. For clinical use, the optical tracer and its target have to be validated. In a combined setting, more sensitive PET and SPECT imaging can be used for target and tracer validation and if successful, the nuclear tracer can be converted to an optical tracer by replacing the radioisotope by a fluorescent label. Also an intermediate stage tracer validation can be performed with dual labeled tracers, for combined nuclear and optical imaging. This makes the integration of nuclear and optical imaging an attractive approach for developing an optical imaging breast cancer screening system capable of early tumor detection.

Supported by grants from Dutch Cancer Society, Pink Ribbon and Pink Ribbon Gala.

References

1. Carney PA, Miglioretti DL, Yankaskas BC, et al. Individual and combined effects of age, breast density, and hormone replacement therapy use on the accuracy of screening mammography. Ann Intern Med 2003;138:168-75.
2. Eckelman WC, Reba RC, Kelloff GJ. Targeted imaging: an important biomarker for understanding disease progression in the era of personalized medicine. Drug Discov Today 2008;13:748-59.
3. Mankoff DA. Molecular imaging as a tool for translating breast cancer science. Breast Cancer Res 2008;10 Suppl 1:S3.
4. Mankoff DA. A definition of molecular imaging. J Nucl Med 2007;48:18N, 21N.
5. Fletcher JW, Djulbegovic B, Soares HP, et al. Recommendations on the use of 18F-FDG PET in oncology. J Nucl Med 2008;49:480-508.
6. Gambhir SS. Molecular imaging of cancer with positron emission tomography. Nat Rev Cancer 2002;2:683-93.
7. Endo K, Oriuchi N, Higuchi T, et al. PET and PET/CT using 18F-FDG in the diagnosis and management of cancer patients. Int J Clin Oncol 2006;11:286-96.
8. Hayashi M, Murakami K, Oyama T, et al. PET/CT supports breast cancer diagnosis and treatment. Breast Cancer 2008;15:224-30.
9. Buck A, Schirrmeister H, Kuhn T, et al. FDG uptake in breast cancer: correlation with biological and clinical prognostic parameters. Eur J Nucl Med Mol Imaging 2002;29:1317-23.
10. Crippa F, Seregni E, Agresti R, et al. Association between [18F]fluorodeoxyglucose uptake and postoperative histopathology, hormone receptor status, thymidine labelling index and p53 in primary breast cancer: a preliminary observation. Eur J Nucl Med 1998;25:1429-34.
11. Bos R, Der Hoeven JJ, van der Wall E, et al. Biologic correlates of (18)fluorodeoxyglucose uptake in human breast cancer measured by positron emission tomography. J Clin Oncol 2002;20:379-87.
12. Hicks RJ, Binns D, Stabin MG. Pattern of uptake and excretion of (18)F-FDG in the lactating breast. J Nucl Med 2001;42:1238-42.
13. Bakheet SM, Powe J, Kandil A, Ezzat A, Rostom A, Amartey J. F-18 FDG uptake in breast infection and inflammation. Clin Nucl Med 2000;25:100-3.
14. Barentsz J, Takahashi S, Oyen W, et al. Commonly used imaging techniques for diagnosis and staging. J Clin Oncol 2006;24:3234-44.
15. Samson DJ, Flamm CR, Pisano ED, Aronson N. Should FDG PET be used to decide whether a patient with an abnormal mammogram or breast

finding at physical examination should undergo biopsy? Acad Radiol 2002;9:773-83.
16. Tafra L, Cheng Z, Uddo J, et al. Pilot clinical trial of 18F-fluorodeoxyglucose positron-emission mammography in the surgical management of breast cancer. Am J Surg 2005;190:628-32.
17. Berg WA, Weinberg IN, Narayanan D, et al. High-resolution fluorodeoxyglucose positron emission tomography with compression ("positron emission mammography") is highly accurate in depicting primary breast cancer. Breast J 2006;12:309-23.
18. Frangioni JV. New technologies for human cancer imaging. J Clin Oncol 2008;26:4012-21.
19. Rosen EL, Eubank WB, Mankoff DA. FDG PET, PET/CT, and breast cancer imaging. Radiographics 2007;27 Suppl 1:S215-S229.
20. Hodgson NC, Gulenchyn KY. Is there a role for positron emission tomography in breast cancer staging? J Clin Oncol 2008;26:712-20.
21. Groheux D, Moretti JL, Baillet G, et al. Effect of (18)F-FDG PET/CT imaging in patients with clinical Stage II and III breast cancer. Int J Radiat Oncol Biol Phys 2008;71:695-704.
22. Fuster D, Duch J, Paredes P, et al. Preoperative staging of large primary breast cancer with [18F]Fluorodeoxyglucose Positron Emission Tomography/Computed Tomography compared with conventional imaging procedures. J Clin Oncol 2008;26:4746-51.
23. Eubank WB, Mankoff DA. Evolving role of positron emission tomography in breast cancer imaging. Semin Nucl Med 2005;35:84-99.
24. Mankoff DA, Eubank WB. Current and future use of positron emission tomography (PET) in breast cancer. J Mammary Gland Biol Neoplasia 2006;11:125-36.
25. Franc BL, Hawkins RA. Positron emission tomography, positron emission tomography-computed tomography, and molecular imaging of the breast cancer patient. Semin Roentgenol 2007;42:265-79.
26. Mahner S, Schirrmacher S, Brenner W, et al. Comparison between positron emission tomography using 2-[fluorine-18]fluoro-2-deoxy-D-glucose, conventional imaging and computed tomography for staging of breast cancer. Ann Oncol 2008;19:1249-54.
27. Minn H, Soini I. [18F]fluorodeoxyglucose scintigraphy in diagnosis and follow up of treatment in advanced breast cancer. Eur J Nucl Med 1989;15:61-6.
28. Cook GJ, Houston S, Rubens R, Maisey MN, Fogelman I. Detection of bone metastases in breast cancer by 18FDG PET: differing metabolic activity in osteoblastic and osteolytic lesions. J Clin Oncol 1998;16:3375-9.

29. Nakai T, Okuyama C, Kubota T, et al. Pitfalls of FDG-PET for the diagnosis of osteoblastic bone metastases in patients with breast cancer. Eur J Nucl Med Mol Imaging 2005;32:1253-8.
30. Shie P, Cardarelli R, Brandon D, Erdman W, Abdulrahim N. Meta-analysis: comparison of F-18 Fluorodeoxyglucose-positron emission tomography and bone scintigraphy in the detection of bone metastases in patients with breast cancer. Clin Nucl Med 2008;33:97-101.
31. Yang WT, Le-Petross HT, Macapinlac H, et al. Inflammatory breast cancer: PET/CT, MRI, mammography, and sonography findings. Breast Cancer Res Treat 2008;109:417-26.
32. National Comprehensive Cancer Network (NCCN) Practice Guidelines in Oncology - v.1.2009; http://www.nccn.org/
33. Therasse P, Arbuck SG, Eisenhauer EA, et al. New guidelines to evaluate the response to treatment in solid tumors. European Organization for Research and Treatment of Cancer, National Cancer Institute of the United States, National Cancer Institute of Canada. J Natl Cancer Inst 2000;92:205-16.
34. Eisenhauer EA, Therasse P, Bogaerts J, et al. New response evaluation criteria in solid tumours: revised RECIST guideline (version 1.1). Eur J Cancer 2009;45:228-47.
35. Weber WA. Positron emission tomography as an imaging biomarker. J Clin Oncol 2006;24:3282-92.
36. Kim SJ, Kim SK, Lee ES, Ro J, Kang S. Predictive value of [18F]FDG PET for pathological response of breast cancer to neo-adjuvant chemotherapy. Ann Oncol 2004;15:1352-7.
37. Boellaard R, Oyen WJ, Hoekstra CJ, et al. The Netherlands protocol for standardisation and quantification of FDG whole body PET studies in multi-centre trials. Eur J Nucl Med Mol Imaging 2008;35:2320-33.
38. Rousseau C, Devillers A, Sagan C, et al. Monitoring of early response to neoadjuvant chemotherapy in stage II and III breast cancer by [18F]fluorodeoxyglucose positron emission tomography. J Clin Oncol 2006;24:5366-72.
39. Schwarz-Dose J, Untch M, Tiling R, et al. Monitoring primary systemic therapy of large and locally advanced breast cancer by using sequential Positron Emission Tomography imaging with [18F]Fluorodeoxyglucose. J Clin Oncol 2009;27:535-41.
40. Berriolo-Riedinger A, Touzery C, Riedinger JM, et al. [18F]FDG-PET predicts complete pathological response of breast cancer to neoadjuvant chemotherapy. Eur J Nucl Med Mol Imaging 2007;34:1915-24.

41. Smith IC, Welch AE, Hutcheon AW, et al. Positron emission tomography using [(18)F]-fluorodeoxy-D-glucose to predict the pathologic response of breast cancer to primary chemotherapy. J Clin Oncol 2000;18:1676-88.
42. McDermott GM, Welch A, Staff RT, et al. Monitoring primary breast cancer throughout chemotherapy using FDG-PET. Breast Cancer Res Treat 2007;102:75-84.
43. Dehdashti F, Flanagan FL, Mortimer JE, Katzenellenbogen JA, Welch MJ, Siegel BA. Positron emission tomographic assessment of "metabolic flare" to predict response of metastatic breast cancer to antiestrogen therapy. Eur J Nucl Med 1999;26:51-6.
44. Mortimer JE, Dehdashti F, Siegel BA, Trinkaus K, Katzenellenbogen JA, Welch MJ. Metabolic flare: indicator of hormone responsiveness in advanced breast cancer. J Clin Oncol 2001;19:2797-803.
45. Dehdashti F, Mortimer JE, Trinkaus K, et al. PET-based estradiol challenge as a predictive biomarker of response to endocrine therapy in women with estrogen-receptor-positive breast cancer. Breast Cancer Res Treat 2009;113:509-17.
46. Cachin F, Prince HM, Hogg A, Ware RE, Hicks RJ. Powerful prognostic stratification by [18F]fluorodeoxyglucose positron emission tomography in patients with metastatic breast cancer treated with high-dose chemotherapy. J Clin Oncol 2006;24:3026-31.
47. Emmering J, Krak NC, van der Hoeven JJ, et al. Preoperative [18F] FDG-PET after chemotherapy in locally advanced breast cancer: prognostic value as compared with histopathology. Ann Oncol 2008;19:1573-7.
48. Gil-Rendo A, Martinez-Regueira F, Zornoza G, Garcia-Velloso MJ, Beorlegui C, Rodriguez-Spiteri N. Association between [(18)F]fluorodeoxyglucose uptake and prognostic parameters in breast cancer. Br J Surg 2009;96:166-70.
49. Ueda S, Tsuda H, Asakawa H, et al. Clinicopathological and prognostic relevance of uptake level using 18F-fluorodeoxyglucose positron emission tomography/computed tomography fusion imaging (18F-FDG PET/CT) in primary breast cancer. Jpn J Clin Oncol 2008;38:250-8.
50. Been LB, Elsinga PH, de Vries J, et al. Positron emission tomography in patients with breast cancer using (18)F-3'-deoxy-3'-fluoro-l-thymidine ((18)F-FLT)-a pilot study. Eur J Surg Oncol 2006;32:39-43.
51. Smyczek-Gargya B, Fersis N, Dittmann H, et al. PET with [18F]fluorothymidine for imaging of primary breast cancer: a pilot study. Eur J Nucl Med Mol Imaging 2004;31:720-4.
52. Pio BS, Park CK, Pietras R, et al. Usefulness of 3'-[F-18]fluoro-3'-deoxythymidine with positron emission tomography in predicting breast cancer response to therapy. Mol Imaging Biol 2006;8:36-42.

53. Kenny L, Coombes RC, Vigushin DM, Al Nahhas A, Shousha S, Aboagye EO. Imaging early changes in proliferation at 1 week post chemotherapy: a pilot study in breast cancer patients with 3'-deoxy-3'-[18F]fluorothymidine positron emission tomography. Eur J Nucl Med Mol Imaging 2007;34:1339-47.
54. Salskov A, Tammisetti VS, Grierson J, Vesselle H. FLT: measuring tumor cell proliferation in vivo with positron emission tomography and 3'-deoxy-3'-[18F]fluorothymidine. Semin Nucl Med 2007;37:429-39.
55. Breast Cancer Treatment (PDQ®). 2009; http://www.cancer.gov/
56. Kataja V, Castiglione M. Locally recurrent or metastatic breast cancer: ESMO clinical recommendations for diagnosis, treatment and follow-up. Ann Oncol 2008;19 Suppl 2:ii11-ii13.
57. Spataro V, Price K, Goldhirsch A, et al. Sequential estrogen receptor determinations from primary breast cancer and at relapse: prognostic and therapeutic relevance. The International Breast Cancer Study Group (formerly Ludwig Group). Ann Oncol 1992;3:733-40.
58. Kuukasjarvi T, Kononen J, Helin H, Holli K, Isola J. Loss of estrogen receptor in recurrent breast cancer is associated with poor response to endocrine therapy. J Clin Oncol 1996;14:2584-9.
59. Brunn RB, Kamby C. Immunohistochemical detection of estrogen receptors in paraffin sections from primary and metastatic breast cancer. Pathol Res Pract 1989;185:856-9.
60. Normanno N, Di Maio M, De Maio E, et al. Mechanisms of endocrine resistance and novel therapeutic strategies in breast cancer. Endocr Relat Cancer 2005;12:721-47.
61. Yoo J, Dence CS, Sharp TL, Katzenellenbogen JA, Welch MJ. Synthesis of an estrogen receptor beta-selective radioligand: 5-[18F]fluoro-(2R,3S)-2,3-bis(4-hydroxyphenyl) pentanenitrile and comparison of in vivo distribution with 16alpha-[18F]fluoro-17beta-estradiol. J Med Chem 2005;48:6366-78.
62. Dehdashti F, Mortimer JE, Siegel BA, et al. Positron tomographic assessment of estrogen receptors in breast cancer: comparison with FDG-PET and in vitro receptor assays. J Nucl Med 1995;36:1766-74.
63. Mintun MA, Welch MJ, Siegel BA, et al. Breast cancer: PET imaging of estrogen receptors. Radiology 1988;169:45-8.
64. Peterson LM, Mankoff DA, Lawton T, et al. Quantitative imaging of estrogen receptor expression in breast cancer with PET and 18F-fluoroestradiol. J Nucl Med 2008;49:367-74.
65. Mortimer JE, Dehdashti F, Siegel BA, Katzenellenbogen JA, Fracasso P, Welch MJ. Positron emission tomography with 2-[18F]Fluoro-2-deoxy-D-glucose and 16alpha-[18F]fluoro-17beta-estradiol in breast cancer:

correlation with estrogen receptor status and response to systemic therapy. Clin Cancer Res 1996;2:933-9.
66. McGuire AH, Dehdashti F, Siegel BA, et al. Positron tomographic assessment of 16 alpha-[18F] fluoro-17 beta-estradiol uptake in metastatic breast carcinoma. J Nucl Med 1991;32:1526-31.
67. Linden HM, Stekhova SA, Link JM, et al. Quantitative fluoroestradiol positron emission tomography imaging predicts response to endocrine treatment in breast cancer. J Clin Oncol 2006;24:2793-9.
68. Hospers GA, Helmond FA, de Vries EG, Dierckx RA, de Vries EF. PET imaging of steroid receptor expression in breast and prostate cancer. Curr Pharm Des 2008;14:3020-32.
69. Moasser MM. The oncogene HER2: its signaling and transforming functions and its role in human cancer pathogenesis. Oncogene 2007;26:6469-87.
70. Hayes DF, Thor AD, Dressler LG, et al. HER2 and response to paclitaxel in node-positive breast cancer. N Engl J Med 2007;357:1496-506.
71. Zidan J, Dashkovsky I, Stayerman C, Basher W, Cozacov C, Hadary A. Comparison of HER-2 overexpression in primary breast cancer and metastatic sites and its effect on biological targeting therapy of metastatic disease. Br J Cancer 2005;93:552-6.
72. Rasbridge SA, Gillett CE, Seymour AM, et al. The effects of chemotherapy on morphology, cellular proliferation, apoptosis and oncoprotein expression in primary breast carcinoma. Br J Cancer 1994;70:335-41.
73. Solomayer EF, Becker S, Pergola-Becker G, et al. Comparison of HER2 status between primary tumor and disseminated tumor cells in primary breast cancer patients. Breast Cancer Res Treat 2006;98:179-84.
74. Meng S, Tripathy D, Shete S, et al. HER-2 gene amplification can be acquired as breast cancer progresses. Proc Natl Acad Sci U S A 2004;101:9393-8.
75. Sekido Y, Umemura S, Takekoshi S, et al. Heterogeneous gene alterations in primary breast cancer contribute to discordance between primary and asynchronous metastatic/recurrent sites: HER2 gene amplification and p53 mutation. Int J Oncol 2003;22:1225-32.
76. Dijkers EC, de Vries EG, Kosterink JG, Brouwers AH, Lub-De Hooge MN. Immunoscintigraphy as potential tool in the clinical evaluation of HER2/neu targeted therapy. Curr Pharm Des 2008;14:3348-62.
77. Perik PJ, Lub-De Hooge MN, Gietema JA, et al. Indium-111-labeled trastuzumab scintigraphy in patients with human epidermal growth factor receptor 2-positive metastatic breast cancer. J Clin Oncol 2006;24:2276-82.

78. Dijkers ECF, Kosterink JG, Rademaker AP, et al. Development and characterization of clinical-grade ^{89}Zr-trastuzumab for HER2/*neu* immunoPET imaging. J Nucl Med 2009;50(6):962-9.
79. Neckers L. Heat shock protein 90: the cancer chaperone. J Biosci 2007;32:517-30.
80. Solit DB, Zheng FF, Drobnjak M, et al. 17-Allylamino-17-demethoxygeldanamycin induces the degradation of androgen receptor and HER-2/neu and inhibits the growth of prostate cancer xenografts. Clin Cancer Res 2002;8:986-93.
81. Zsebik B, Citri A, Isola J, Yarden Y, Szollosi J, Vereb G. Hsp90 inhibitor 17-AAG reduces ErbB2 levels and inhibits proliferation of the trastuzumab resistant breast tumor cell line JIMT-1. Immunol Lett 2006;104:146-55.
82. Jensen MR, Schoepfer J, Radimerski T, et al. NVP-AUY922: a small molecule HSP90 inhibitor with potent antitumor activity in preclinical breast cancer models. Breast Cancer Res 2008;10:R33.
83. Eccles SA, Massey A, Raynaud FI, et al. NVP-AUY922: a novel heat shock protein 90 inhibitor active against xenograft tumor growth, angiogenesis, and metastasis. Cancer Res 2008;68:2850-60.
84. Smith-Jones PM, Solit DB, Akhurst T, Afroze F, Rosen N, Larson SM. Imaging the pharmacodynamics of HER2 degradation in response to Hsp90 inhibitors. Nat Biotechnol 2004;22:701-6.
85. Smith-Jones PM, Solit D, Afroze F, Rosen N, Larson SM. Early tumor response to Hsp90 therapy using HER2 PET: comparison with 18F-FDG PET. J Nucl Med 2006;47:793-6.
86. Oude Munnink TH, de Korte MA, Nagengast WB, et al. ^{89}Zr-trastuzumab PET visualizes HER2 downregulation induced by the HSP90 inhibitor NVP-AUY922 in human tumor xenograft. Eur J Cancer 2010;46:678-84
87. Miller K, Wang M, Gralow J, et al. Paclitaxel plus bevacizumab versus paclitaxel alone for metastatic breast cancer. N Engl J Med 2007;357:2666-76.
88. Nagengast WB, de Vries EG, Hospers GA, et al. In vivo VEGF imaging with radiolabeled bevacizumab in a human ovarian tumor xenograft. J Nucl Med 2007;48:1313-9.
89. Jayson GC, Zweit J, Jackson A, et al. Molecular imaging and biological evaluation of HuMV833 anti-VEGF antibody: implications for trial design of antiangiogenic antibodies. J Natl Cancer Inst 2002;94:1484-93.
90. Collingridge DR, Carroll VA, Glaser M, et al. The development of [(124)I]iodinated-VG76e: a novel tracer for imaging vascular endothelial growth factor in vivo using positron emission tomography. Cancer Res 2002;62:5912-9.

91. Nagengast W, De Vries E, Warnders F, et al. In vivo VEGF imaging with an anti-VEGF Fab-fragment in a human ovarian tumor xenograft model using MicroPET and MicroCT. AACR Meeting Abstracts 2008; abstract #3161.
92. Nagengast WB, Lub-De Hooge MN, Hospers GA, et al. Towards clinical VEGF imaging using the anti-VEGF antibody bevacizumab and Fab-fragment ranibizumab. J Clin Oncol 2008; 26: abstract #3547
93. Brown ML, Houn F, Sickles EA, Kessler LG. Screening mammography in community practice: positive predictive value of abnormal findings and yield of follow-up diagnostic procedures. AJR Am J Roentgenol 1995;165:1373-7.
94. Kerlikowske K, Grady D, Barclay J, Sickles EA, Eaton A, Ernster V. Positive predictive value of screening mammography by age and family history of breast cancer. JAMA 1993;270:2444-50.
95. Lidbrink E, Elfving J, Frisell J, Jonsson E. Neglected aspects of false positive findings of mammography in breast cancer screening: analysis of false positive cases from the Stockholm trial. BMJ 1996;312:273-6.
96. Viacava P, Naccarato AG, Bocci G, et al. Angiogenesis and VEGF expression in pre-invasive lesions of the human breast. J Pathol 2004;204:140-6.
97. Kenny LM, Coombes RC, Oulie I, et al. Phase I trial of the positron-emitting Arg-Gly-Asp (RGD) peptide radioligand 18F-AH111585 in breast cancer patients. J Nucl Med 2008;49:879-86.
98. Beer AJ, Niemeyer M, Carlsen J, et al. Patterns of alphavbeta3 expression in primary and metastatic human breast cancer as shown by 18F-Galacto-RGD PET. J Nucl Med 2008;49:255-9.
99. Schneider BP, Winer EP, Foulkes WD, et al. Triple-negative breast cancer: risk factors to potential targets. Clin Cancer Res 2008;14:8010-8.
100. Bauer KR, Brown M, Cress RD, Parise CA, Caggiano V. Descriptive analysis of estrogen receptor (ER)-negative, progesterone receptor (PR)-negative, and HER2-negative invasive breast cancer, the so-called triple-negative phenotype: a population-based study from the California cancer Registry. Cancer 2007;109:1721-8.
101. Mersin H, Yildirim E, Berberoglu U, Gulben K. The prognostic importance of triple negative breast carcinoma. Breast 2008;17:341-6.
102. Cleator S, Heller W, Coombes RC. Triple-negative breast cancer: therapeutic options. Lancet Oncol 2007;8:235-44.
103. Cai W, Niu G, Chen X. Multimodality imaging of the HER-kinase axis in cancer. Eur J Nucl Med Mol Imaging 2008;35:186-208.

104. Law JH, Habibi G, Hu K, et al. Phosphorylated insulin-like growth factor-i/insulin receptor is present in all breast cancer subtypes and is related to poor survival. Cancer Res 2008;68:10238-46.
105. Cornelissen B, McLarty K, Kersemans V, Reilly RM. The level of insulin growth factor-1 receptor expression is directly correlated with the tumor uptake of (111)In-IGF-1(E3R) in vivo and the clonogenic survival of breast cancer cells exposed in vitro to trastuzumab (Herceptin). Nucl Med Biol 2008;35:645-53.
106. Massague J. TGFbeta in cancer. Cell 2008;134:215-30.
107. Bhardwaj B, Klassen J, Cossette N, et al. Localization of platelet-derived growth factor beta receptor expression in the periepithelial stroma of human breast carcinoma. Clin Cancer Res 1996;2:773-82.
108. Cristofanilli M, Morandi P, Krishnamurthy S, et al. Imatinib mesylate (Gleevec) in advanced breast cancer-expressing C-Kit or PDGFR-beta: clinical activity and biological correlations. Ann Oncol 2008;19:1713-9.
109. Jechlinger M, Sommer A, Moriggl R, et al. Autocrine PDGFR signaling promotes mammary cancer metastasis. J Clin Invest 2006;116:1561-70.
110. Beljaars L, Weert B, Geerts A, Meijer DK, Poelstra K. The preferential homing of a platelet derived growth factor receptor-recognizing macromolecule to fibroblast-like cells in fibrotic tissue. Biochem Pharmacol 2003;66:1307-17.
111. van de Ven SM, Elias SG, van den Bosch MA, Luijten P, Mali WP. Optical imaging of the breast. Cancer Imaging 2008;8:206-15.

Chapter 3:

^{89}Zr-trastuzumab PET visualizes HER2 downregulation by the HSP90 inhibitor NVP-AUY922 in a human tumor xenograft

Thijs Oude Munnink[1#]
Maarten de Korte[1#]
Wouter Nagengast[1]
Hetty Timmer-Bosscha[1]
Carolina Schröder[1]
Johan de Jong[2]
Guus van Dongen[3]
Michael Rugaard Jensen[4]
Cornelia Quadt[5]
Marjolijn Lub-de Hooge[2,6]
Elisabeth de Vries[1]

Contributed equally[#]

Departments of Medical Oncology[1] and Nuclear Medicine and Molecular Imaging[2], University Medical Center Groningen, Groningen, The Netherlands; Department of Nuclear Medicine and PET Research[3],VU University Medical Center, Amsterdam, The Netherlands; Novartis Institute for Biomedical Research[4], Basel, Switzerland; Novartis Pharma[5], Basel, Switzerland; Department of Hospital and Clinical Pharmacy[6], University Medical Center Groningen, Groningen, The Netherlands

European Journal of Cancer 2010;46:678-84

ABSTRACT

NVP-AUY922, a potent heat shock protein-90 (HSP90) inhibitor, downregulates the expression of many oncogenic proteins, including the human epidermal growth factor receptor-2 (HER2). Because HER2 downregulation is a potential biomarker for early response to HSP90 targeted therapies, we used the ^{89}Zr labeled HER2 antibody trastuzumab to quantify the alterations in HER2 expression after NVP-AUY922 treatment with HER2 positron emission tomography (PET) imaging.

The HER2 overexpressing human SKOV-3 ovarian tumor cell line was used for in vitro experiments and as xenograft model in nude athymic mice. *In vitro* HER2 membrane expression was assessed by flow cytometry and a radio-immuno assay with ^{89}Zr-trastuzumab. For *in vivo* evaluation, mice received 50 mg/kg NVP-AUY922 intraperitoneally every other day. ^{89}Zr-trastuzumab was injected intravenously 6 days before NVP-AUY922 treatment and after 3 NVP-AUY922 doses. MicroPET imaging was performed at 24, 72 and 144 h post tracer injection followed by ex-vivo biodistribution and immunohistochemical staining.

After 24 h NVP-AUY922 treatment HER2 membrane expression showed profound reduction with flow cytometry (80%) and radio immuno assay (75%). PET tumor quantification, showed a mean reduction of 41% (P = 0.0001) in ^{89}Zr-trastuzumab uptake at 144 h post tracer injection after NVP-AUY922 treatment. PET results were confirmed by *ex vivo* ^{89}Zr-trastuzumab biodistribution and HER2 immunohistochemical staining.

NVP-AUY922 effectively downregulates HER2, which can be monitored and quantified *in vivo* non-invasively with ^{89}Zr-trastuzumab PET. This technique is currently under clinical evaluation and might serve as an early biomarker for HSP90 inhibition in HER2 positive metastatic breast cancer patients.

INTRODUCTION

Heat shock protein-90 (HSP90) is a 90 kDa molecular chaperone protein which is involved in the conformation, activation, functionality and stability of over hundred client proteins. Client proteins of HSP90 are involved in all hallmarks of oncogenesis: tumor cell growth, invasion, metastasis, angiogenesis, evading apoptosis and insensitivity to anti-growth signals.[1] Tumor cells overexpress HSP90 2- to 10- fold compared to normal cells of the related tissue and are more dependent on HSP90 than normal counterparts.[2] In tumor cells HSP90 is predominantly present in an active complexed state with a higher ATPase activity and ATP affinity.[3] These characteristics make HSP90 a target with high potential for cancer therapy, as inhibition of HSP90 results in targeting multiple signaling pathways crucial for tumor maintenance.

Several HSP90 inhibitors are currently in clinical development. Most preclinical and clinical experience has been obtained with the geldanamycin class of HSP90 inhibitors of which 17-(allylamino)-17-demethoxygeldanamycin (17AAG; tanespimycin) is the best studied family member. Therapeutic effects (disease stabilization, tumor responses) of 17AAG were seen in several phase I and II trials, including a phase II trial in patients refractory to trastuzumab therapy.[4;5] However, clinical application of 17AAG is hampered due to hepatotoxicity and formulation difficulties.

A new interesting class of HSP90 inhibitors consists of the pyrazole resorcinols, of which NVP-AUY922 is *in vitro* the most potent family member.[6] Preclinical activity of NVP-AUY922 has been reported recently[7;8] and NVP-AUY922 is currently being investigated in two phase I-II clinical trials.

Monitoring the pharmacodynamic effects of HSP90 inhibitors would facilitate the clinical development of these drugs. Currently, there is no proven early biomarker for evaluating HSP90 inhibition. In a clinical phase I study with 17AAG, tumor biopsies were taken in which Western blot analysis revealed c-RAF1 inhibition, CDK4 depletion and HSP70 induction.[4] The limited feasibility of repeated tumor biopsies, however, has driven the search for non-invasive pharmacodynamic monitoring of HSP90 inhibitors.[9]

One of the most potent oncogenic client proteins of HSP90 is the human epidermal growth factor receptor-2 (HER2). HER2 is a key player in oncogenic transformation in a variety of cancer types and is overexpressed in 20-25% of

breast cancers.[10] The rapid but transient HER2 degradation induced by HSP90 inhibition has been shown *in vitro* and *in vivo* in several preclinical reports.[7;8;11;12]

Molecular imaging techniques are well suited for non-invasive monitoring of the rapid molecular changes induced by tumor targeting therapies. Serial HER2 positron emission tomography (PET) imaging is potentially attractive as biomarker as it allows the visualization and quantification of the molecular tumor response to the drug early during treatment.

HER2-PET imaging with a ^{68}Ga labeled trastuzumab F(ab')$_2$ fragment (^{68}Ga-DCHF) has preclinically shown to be able to monitor the HER2 downregulation after 17AAG treatment.[13] In the search for a clinical usable PET tracer, we labeled the full length HER2 antibody trastuzumab with the long-lived PET isotope zirconium-89 (^{89}Zr) for HER2-PET imaging. The pre-clinical kinetics and biodistribution of ^{89}Zr-trastuzumab have recently been described.[14] Our clinical experience with this tracer for HER2 imaging in metastatic breast cancer patients showed excellent feasibility.[15] In the present study, we aim to use ^{89}Zr-trastuzumab PET imaging for non-invasive quantification of the HER2 downregulation by the HSP90 inhibitor NVP-AUY922 in a HER2 positive xenograft model.

MATERIALS AND METHODS

Cell line and reagents

The HER2 overexpressing human ovarian cancer cell-line SKOV-3 was obtained from the American Type Culture Collection. Cells were cultured in a humidified incubator at 5% CO_2 and 37 °C in D-MEM high glucose, supplemented with 10% FCS. NVP-AUY922 was provided by Novartis. 17AAG was purchased from LC Laboratories and was used as a reference for the in vitro effects of NVP-AUY922. For the *in vitro* experiments NVP-AUY922 and 17AAG were dissolved in DMSO and stored at -80 or -20 °C, respectively. For intraperitoneal (i.p.) administration, NVP-AUY922 was dissolved in 5% glucose and was delivered in a volume of 200 µL. *In vivo* experiments were performed with NVP-AUY922 only.

Flow cytometry

Attached cells were incubated with 30 or 100 nM NVP-AUY922 for 24 h. In these concentrations, NVP-AUY922 was shown to downregulate HER2 expression in vitro.[7;8] For reference, cells were also incubated with 30, 100 or 500 nM 17AAG. Cells were harvested with trypsin, washed and diluted in cold phosphate buffered saline (PBS). Subsequently, cells were incubated on ice for 45 min with 20 μg/mL trastuzumab followed by 45 min with 20 μg/mL monoclonal anti-human IgG, FITC conjugated (Clone HP 6017, Sigma). Membrane receptor expression was analyzed using flow cytometry (FACSCalibur, BD Biosciences) with Winlist software (Verity Software House). For every treatment condition, 3 independent experiments were performed.

Conjugation and ^{89}Zr-labeling of trastuzumab

Trastuzumab (Herceptin, Roche) conjugation and labeling was performed as described previously.[14] Briefly, trastuzumab was first conjugated with the chelater N-succinyldesferrioxamine B-tetrafluorphenol (N-sucDf-TFP; VUMC). After conjugation, the product was purified by ultracentrifugation and stored at -20 °C. In the second step, N-sucDf-trastuzumab was radiolabeled with clinical-grade ^{89}Zr oxalate (IBA Molecular).

Conjugation and ^{111}In-labeling of control human IgG

Human IgG (Sanquin) conjugation and labeling was performed according to Ruegg.[14;16] Briefly, IgG was first conjugated to the bifunctional conjugating agent 2-(4-Isothiocyanatobenzyl)-diethylenetriaminepentaacetic acid (*p*-SCN-Bn-DTPA, Macrocyclics). After conjugation, the product was used for radiolabeling immediately or stored at -20°C. Conjugated human IgG was radiolabeled with $^{111}InCl_3$ (Covidien). Glassware, materials and solutions used for the conjugation and labeling procedures were sterilized, pyrogen-free and metal-free.

Radio immuno assay

Attached cells were incubated with 30 or 100 nM NVP-AUY922 or 500 nM 17AAG for 24 h. Cells were harvested following trypsinization and were washed and diluted in cold PBS. To correct for aspecific binding, a sample of the

untreated cells was blocked with a 500-fold excess of unlabeled trastuzumab. For each condition, $5x10^5$ cells were incubated in triplicate for 60 min with 1 μg ^{89}Zr-trastuzumab at 4 °C. Binding of ^{89}Zr-trastuzumab was measured in a calibrated well-type LKB-1282-Compu-gamma system (LKB Wallac). For every treatment condition, 3 independent experiments were performed.

Animal studies

In vivo imaging and biodistribution experiments were conducted using male athymic mice (Hsd:Athymic Nude/nu) obtained from Harlan. Mice were injected subcutaneously with 10^6 SKOV-3 cells mixed equally with Matrigel™ (BD Bioscience). When tumors measured between 5-8 mm in diameter (~ 0.2 cm^3), approximately 2-3 weeks after inoculation, mice were injected with a ^{89}Zr-trastuzumab (100 μg, ± 5 MBq) and IgG (100 μg) co-injection via the penile vein. Animals were imaged using a MicroPET Focus 220 rodent scanner (CTI Siemens). Static images of 15-45 min acquisition time were obtained at 24, 72 and 144 h postinjection. NVP-AUY922 was administered i.p. every other day in a dose of 50 mg/kg starting directly after the 144 h scan of the baseline ^{89}Zr-trastuzumab injection. With this treatment regimen, NVP-AUY922 has shown to decrease HER2 tumor expression and to effectively inhibit tumor growth *in vivo*, with acceptable tolerability.[8] After 3 doses of NVP-AUY922, mice were again injected with ^{89}Zr-trastuzumab (100 μg, ± 5 MBq) and ^{111}In-IgG (100 μg, ± 5 MBq) co-injection. Post treatment microPET scans were acquired according to the same schedule as described for the baseline scans. NVP-AUY922 treatment was continued till the last scan. After image reconstruction, *in vivo* quantification was performed with AMIDE Medical Image Data Examiner software (version 0.9.1, Stanford University)[17] and tumor accumulation was calculated as Standardized Uptake Value (SUV). Animals were sacrificed after the last scan and organs were excised, rinsed for residual blood, weighed and counted for radioactivity in a calibrated well-type LKB-1282-Compu-gamma system. Tissue activity is expressed as percentage of the injected dose per gram tissue (%ID/g). A separate group of mice receiving only the vehicle was used as control for ^{89}Zr-trastuzumab and ^{111}In-IgG biodistribution. Experiments were performed with isofluran inhalation anaesthesia (induction 3%, maintenance 1.5%) and were approved by the animal experiments committee of the University of Groningen.

Immunohistochemistry

Tumors were kept on ice during biodistribution analysis and subsequently processed for immunohistochemical analysis. Formalin-fixed, paraffin-embedded tumors were stained with antibodies against HER2 (HercepTest™, DAKO). Immunohistochemistry results were scored semi quantitatively according to the system used in clinical testing (0, 1, 2 and 3+, which corresponds with no, weak, moderate or strong circumferential, membranous staining).

Statistical analysis

Data are presented as mean ± standard deviation. Statistical analysis was performed using the Mann-Whitney test for non-parametric data, an unpaired T-test for parametric data and a paired sampled T-test for paired data (SPSS, version 16). A P value ≤ 0.05 was considered significant.

RESULTS

NVP-AUY922 downregulates HER2 expression in SKOV-3 cells *in vitro*

NVP-AUY922 induced HER2 downregulation is shown in Fig.1A. Treatment with 30 and 100 nM NVP-AUY922 for 24 h resulted in HER2 downregulation of 72.5 ± 2.4% and 80.1 ± 1.4%, respectively, compared with untreated control cells. Treatment with 30, 100 and 500 nM 17AAG resulted in HER2 downregulation of 11.4 ± 3.6%, 41.6 ± 3.7% and 82.0 ± 1.2%, respectively, compared with untreated control cells. NVP-AUY922 and 17AAG isomolar concentrations of 30 and 100 nM resulted in a more pronounced HER2 downregulation after NVP-AUY922 treatment than after 17AAG treatment with P values < 0.0001. Treatment with 500 nM 17AAG resulted in similar HER2 downregulation as 100 nM NVP-AUY922 (P = 0.15).

NVP-AUY922 reduces ^{89}Zr-trastuzumab binding to SKOV-3 cells *in vitro*

^{89}Zr-trastuzumab binding to SKOV-3 cells after 24 h treatment with NVP-AUY922, 17AAG and control is shown in Fig 1B. Binding of ^{89}Zr-trastuzumab to untreated SKOV-3 cells was 21.7 ± 8.4% of the total ^{89}Zr-trastuzumab applied. Blocking the cells with an excess of unlabelled trastuzumab reduced ^{89}Zr-trastuzumab binding to 0.31 ± 0.03%, being the non-specific binding of ^{89}Zr-

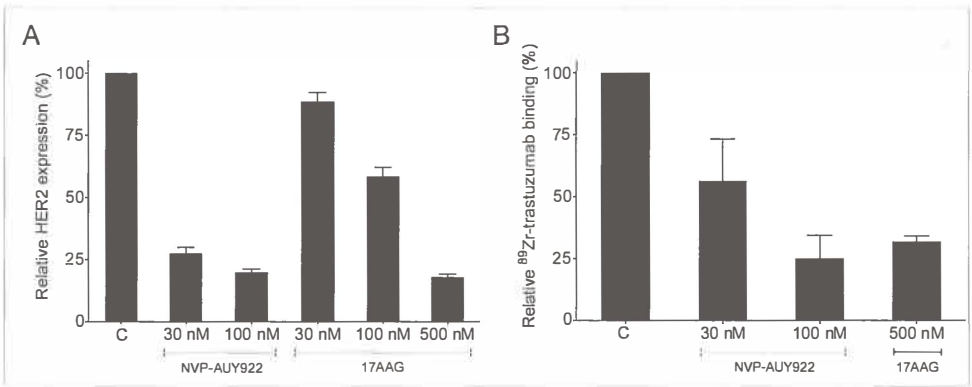

Figure 1. HER2 downregulation, as determined by flow cytometry (A) and ^{89}Zr-trastuzumab binding, as determined by radio-immuno assay (B), after 24 h treatment with NVP-AUY922 and 17AAG.

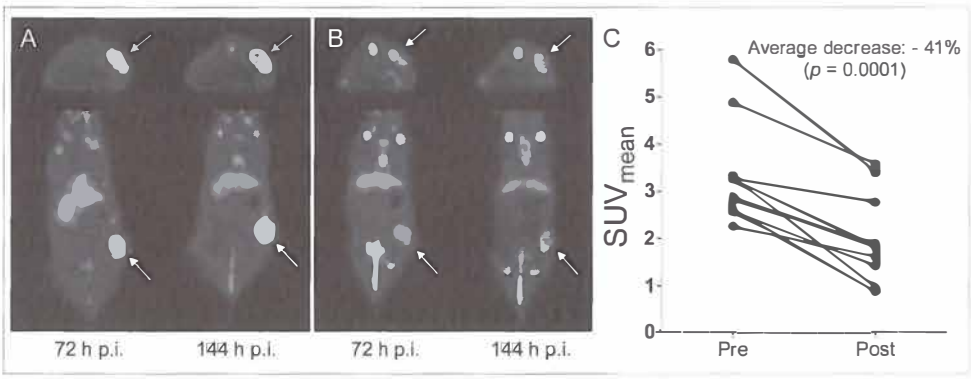

Figure 2. Transversal and coronal PET images of a representative mouse scanned with ^{89}Zr-trastuzumab before (A) and after (B) treatment with NVP-AUY922. Arrows indicate tumor. PET quantification of ^{89}Zr-trastuzumab tumor uptake at 144 h postinjection is shown in C. See page 167 for full color image.

trastuzumab. Treatment of the cells with 30 and 100 nM NVP-AUY922 reduced the specific binding of ^{89}Zr-trastuzumab compared to control by 43.7 ± 16.9% and 74.9 ± 9.3%, respectively. Treatment with 500 nM 17AAG resulted in a reduction of ^{89}Zr-trastuzumab specific binding with 68.2 ± 2.2%, which was similar to 100 nM NVP-AUY922 (P = 0.29).

^{89}Zr-trastuzumab PET imaging shows reduced tumor uptake after NVP-AUY922 treatment

Visual analysis of PET imaging showed a time dependent accumulation of ^{89}Zr-trastuzumab within the tumors. At 144 h postinjection, tumor uptake of ^{89}Zr-

trastuzumab was higher than at 72 h postinjection. Fig. 2A and B show the transversal and coronal images of a representative mouse scanned at 72 and 144 h postinjection of ^{89}Zr-trastuzumab before and after treatment with NVP-AUY922. Treatment with NVP-AUY922 results in a clearly visible decrease in ^{89}Zr-trastuzumab tumor uptake. The mean SUV at baseline was 2.9 ± 0.6 and 3.4 ± 1.1 at 72 and 144 h postinjection, respectively. The decrease in ^{89}Zr-trastuzumab tumor uptake after NVP-AUY922 treatment was 34 ± 23% (P = 0.0009) and 41 ± 17% (P = 0.0001) at 72 and 144 h postinjection, respectively, resulting in a post treatment SUV of 1.9 ± 0.8 and 2.0 ± 0.9 at 72 and 144 h postinjection, respectively. Fig. 2C shows the individual tumor SUVs at 144 h postinjection of ^{89}Zr-trastuzumab pre and post treatment with NVP-AUY922.

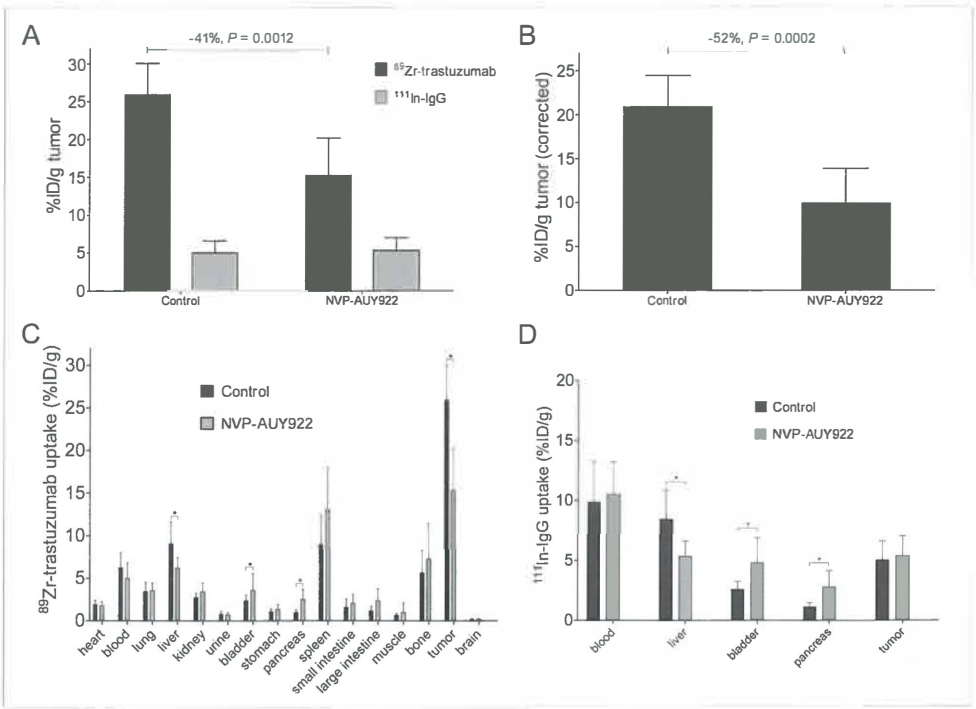

Figure 3. ^{89}Zr-trastuzumab and ^{111}In-IgG tumor uptake (A, B) and biodistribution (C, D). Mice were treated with NVP-AUY922 (50 mg/kg, 3qw) or control for 10 days. Both tracers were co-injected at 4 days after initiation of treatment.

Biodistribution results in the NVP-AUY922 treatment group (n = 10) were compared with the ^{89}Zr-trastuzumab and ^{111}In-IgG biodistribution in a control

group (n = 7), which received only the vehicle. This comparison was made to determine if the reduced ^{89}Zr-trastuzumab tumor uptake after NVP-AUY922 treatment was indeed caused by a downregulation of HER2. This proved to be the case as there was a 41% (P = 0.0012) lower tumor uptake of ^{89}Zr-trastuzumab in the NVP-AUY922 treated mice, compared to the control mice (Fig. 3A) while there was no difference in ^{111}In-IgG tumor uptake between treated and control mice. The ^{89}Zr-trastuzumab tumor uptake was corrected for non specific uptake by subtracting the ^{111}In-IgG tumor uptake for each mouse (Fig. 3B). This correction reveals the HER2 driven ^{89}Zr-trastuzumab tumor uptake which was reduced with 52% (P = 0.0002) after NVP-AUY922 treatment, compared to control.

The ^{89}Zr-trastuzumab biodistribution profile at 6 days postinjection in treated and control mice shows that NVP-AUY922 affected ^{89}Zr-trastuzumab uptake in liver, bladder, pancreas and tumor (Fig. 3C). ^{89}Zr-trastuzumab uptake was higher in bladder and pancreas and lower in liver and tumor in the NVP-AUY922 treated group. These alterations in ^{89}Zr-trastuzumab uptake in liver, bladder and pancreas were also seen with ^{111}In-IgG (Fig. 3D), indicating a non HER2 driven mechanism.

Immunohistochemistry

HER2 immunohistochemistry performed on tumors obtained from the biodistribution experiment confirmed the HER2 downregulation in the NVP-AUY922 treated group. All the tumors from the treated mice were still HER2 positive (1+ or 2+), however the HER2 staining in this group was overall less intense compared to the control group (Fig. 4).

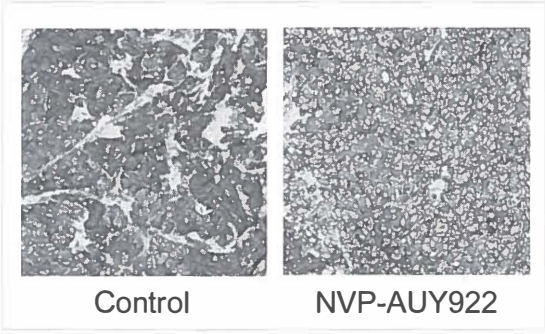

Figure 4. HER2 immunohistochemistry in representative tumors from a control and a NVP-AUY922 treated mouse. Mice were treated with NVP-AUY922 (50 mg/kg, 3qw) or control for 10 days. Tumor samples were collected 2 days after the last dose of NVP-AUY922. See page 167 for full color image.

DISCUSSION

In the present study, we successfully demonstrate the feasibility of ^{89}Zr-trastuzumab HER2-PET as a biomarker for HSP90 inhibition in a HER2 positive xenograft model. Currently, there is no clinically proven early biomarker for evaluating the pharmacodynamic effects of HSP90 inhibition. Serial molecular imaging can provide information about the molecular alterations as an early response to HSP90 inhibition. Because many oncoproteins are clients of HSP90,[18;19] there are several molecular imaging target opportunities for non-invasive monitoring of HSP90 inhibition. EGFR imaging with ^{64}Cu-cetixumab has been used for pharmacodynamic monitoring of 17AAG in PC-3 human prostate cancer xenografts.[20] However, HER2 imaging is probably a better readout than EGFR imaging since HER2 is likely the client protein most sensitive to HSP90 inhibition and in addition, both nascent and mature HER2 are downregulated by HSP90 inhibition, whereas only nascent EGFR is downregulated.[21] Therefore, for HER2 positive cancers, molecular imaging of HER2 expression during HSP90 inhibiting therapies has the best potential for pharmacodynamic monitoring. This approach has also been evaluated previously in other preclinical models. HER2 downregulation induced by 17AAG in a BT-474 human breast cancer xenograft model was monitored by PET imaging with ^{68}Ga-DCHF. ^{68}Ga-DCHF tumor uptake was reduced by 50% after treatment with 17AAG (3 x 50 mg/kg in 24 h), compared to baseline ^{68}Ga-DCHF tumor uptake.[13] In the same xenograft model, the tumor uptake of the metabolic PET tracer [^{18}F]fluorodeoxyglucose (FDG) was unaffected by 17AAG during the follow-up period of 21 days after treatment.[22] This indicates that HER2 imaging is more useful as an early biomarker for HSP90 inhibition than metabolic FDG imaging.

Radiolabeled full length trastuzumab has been used previously by others to assess HER2 downregulation after HSP90 inhibition. PET imaging with ^{64}Cu-trastuzumab showed a 64% reduction in tumor uptake 24 h after treatment of SKOV-3 xenograft bearing mice with 17-(dimethylaminoethylamino)-17-demethoxygeldanamycin (17-DMAG; alvespimycin) (3 x 50 mg/kg in 24 h).[23] Similar results were seen with HER2-PET imaging using the ^{18}F-FBEM-$Z_{HER2:342}$ affibody molecule after treatment of BT474 xenografts with 17-DMAG (40 mg/kg/day, 4 doses).[24]

NVP-AUY922 induced downregulation of HER2 was first shown in HCT116 colon carcinoma cells by Western blot analysis.[6] In a BT-474 human breast cancer xenograft model, a single dose of 50 mg/kg NVP-AUY922 resulted in a HER2

downregulation, as determined with immunohistochemistry and Western blot.[8] Our *in vitro* results confirm the HER2 downregulation by NVP-AUY922, which was more potent than that of 17AAG in isomolar concentrations. It should be noted that NVP-AUY922 is a very promising HSP90 inhibitor, which shows considerably less toxic effects than the geldanamycin derivatives in the current clinical phase I evaluation.

Our *in vivo* results show an average decrease of 41% in ^{89}Zr-trastuzumab tumor uptake, which is comparable with the decrease which was reported with ^{68}Ga-DCHF, ^{18}F-FBEM-$Z_{HER2:342}$ and ^{64}Cu-trastuzumab after HSP90 inhibiting treatment. Main difference between ^{68}Ga-DCHF, ^{18}F-FBEM-$Z_{HER2:342}$, ^{64}Cu-trastuzumab and ^{89}Zr-trastuzumab HER2-PET imaging is the interval between tracer injection and scan acquisition, which is limited by the physical half-life of the radioisotopes. Half-lives of 1.13 and 1.83 h limit imaging with ^{68}Ga-DCHF and ^{18}F-FBEM-$Z_{HER2:342}$ to several hours post tracer injection, were the half-life of ^{64}Cu of 12.7 h allows trastuzumab imaging up to 48 h. We performed HER2-PET imaging in metastatic breast cancer patients up to 7 days postinjection of ^{89}Zr-trastuzumab (with a half-life of 78.4 h) and found that the best images were obtained at days 4 and 5.[15] This is in accordance with the fact that antibodies like trastuzumab accumulate slowly into tumors, which makes trastuzumab imaging days after injection more rational. Our imaging data with ^{89}Zr-trastuzumab in the present study were acquired 72 and 144 h postinjection during treatment with NVP-AUY922 every 48 h. These data showed still an increase over time of ^{89}Zr-trastuzumab tumor uptake from 72 to 144 h. The effect of NVP-AUY922 on ^{89}Zr-trastuzumab tumor uptake was most pronounced at 144 h post tracer injection. The tumor uptake of ^{89}Zr-trastuzumab at 144 h postinjection reflects the level of HER2 membrane expression during that 144 h, which will be the integrated result of NVP-AUY922 induced HER2 downregulation over this interval.

Even though HER2 may serve as an excellent read out for HSP90 inhibition, it is not universally expressed in tumor tissue. Therefore, also other client proteins are of interest in this setting. In our institution, we have also studied the effect of HSP90 inhibition on VEGF expression by means of ^{89}Zr-bevacizumab PET in a preclinical model. An advantage of this marker is that it is universally expressed in tumors, although VEGF may not be as sensitive as readout compared to HER2. HER2 imaging is readily available for use in patients in our institution, and at present we are translating these preclinical results to the clinical setting in collaboration with the Royal Marsden institute in London.

In summary, this paper describes the successful preclinical validation of ^{89}Zr-trastuzumab HER2-PET for non-invasive pharmacodynamic monitoring of the HER2 downregulation by the HSP90 inhibitor NVP-AUY922. This technique might serve as an early biomarker for HSP90 inhibition in HER2 positive metastatic breast cancer patients and could potentially support patient tailored therapy.

Conflict of interest statement

MRJ and CQ are employees and stockholders of Novartis Pharma AG.

Acknowledgements

The authors would like to thank Kirsten van Huisstede and Esther van Straten for their technical assistance. Supported by grant 2007-3739 of the Dutch Cancer Society.

References

1. Workman P, Burrows F, Neckers L, Rosen N. Drugging the cancer chaperone HSP90: combinatorial therapeutic exploitation of oncogene addiction and tumor stress. Ann N Y Acad Sci 2007;1113,202-16.
2. Ferrarini M, Heltai S, Zocchi MR, Rugarli C. Unusual expression and localization of heat-shock proteins in human tumor cells. Int J Cancer 1992;51,613-9.
3. Kamal A, Thao L, Sensintaffar J, et al. A high-affinity conformation of Hsp90 confers tumour selectivity on Hsp90 inhibitors. Nature 2003; 425, 407-10.
4. Banerji U, O'Donnell A, Scurr M, et al. Phase I pharmacokinetic and pharmacodynamic study of 17-allylamino, 17-demethoxygeldanamycin in patients with advanced malignancies. J Clin Oncol 2005;23,4152-61.
5. Modi S, Stopeck AT, Gordon MS, et al. Combination of trastuzumab and tanespimycin (17-AAG, KOS-953) is safe and active in trastuzumab-refractory HER-2 overexpressing breast cancer: a phase I dose-escalation study. J Clin Oncol 2007;25,5410-7.
6. Brough PA, Aherne W, Barril X, et al. 4,5-diarylisoxazole Hsp90 chaperone inhibitors: potential therapeutic agents for the treatment of cancer. J Med Chem 2008;51,196-218.
7. Eccles SA, Massey A, Raynaud FI, et al. NVP-AUY922: a novel heat shock protein 90 inhibitor active against xenograft tumor growth, angiogenesis, and metastasis. Cancer Res 2008;68,2850-60.
8. Jensen MR, Schoepfer J, Radimerski T, et al. NVP-AUY922: a small molecule HSP90 inhibitor with potent antitumor activity in preclinical breast cancer models. Breast Cancer Res 2008;10,R33.
9. Seddon BM, Workman P. The role of functional and molecular imaging in cancer drug discovery and development. Br J Radiol 2003;76 Spec No 2,S128-S38.
10. Moasser MM. The oncogene HER2: its signaling and transforming functions and its role in human cancer pathogenesis. Oncogene 2007;26,6469-87.
11. Solit DB, Zheng FF, Drobnjak M, et al. 17-Allylamino-17-demethoxygeldanamycin induces the degradation of androgen receptor and HER-2/neu and inhibits the growth of prostate cancer xenografts. Clin Cancer Res 2002;8,986-93.
12. Zsebik B, Citri A, Isola J, Yarden Y, Szollosi J, Vereb G. Hsp90 inhibitor 17-AAG reduces ErbB2 levels and inhibits proliferation of the trastuzumab resistant breast tumor cell line JIMT-1. Immunol Lett 2006;104,146-55.

13. Smith-Jones PM, Solit DB, Akhurst T, Afroze F, Rosen N, Larson SM. Imaging the pharmacodynamics of HER2 degradation in response to Hsp90 inhibitors. Nat Biotechnol 2004;22,701-6.
14. Dijkers ECF, Kosterink JG, Rademaker AP, et al. Development and characterization of clinical-grade ^{89}Zr-trastuzumab for HER2/neu immunoPET imaging. J Nucl Med 2009;50,962-9.
15. Dijkers ECF, Oude Munnink TH, Kosterink JG, et al. Biodistribution of ^{89}Zr-trastuzumab and PET imaging of HER2-positive lesions in patients with metastatic breast cancer.. Clin Pharmacol Ther. 2010;87:586-92
16. Ruegg CL, Anderson-Berg WT, Brechbiel MW, Mirzadeh S, Gansow OA, Strand M. Improved in vivo stability and tumor targeting of bismuth-labeled antibody. Cancer Res 1990;50,4221-6.
17. Loening AM, Gambhir SS. AMIDE: a free software tool for multimodality medical image analysis. Mol Imaging 2003;2,131-7.
18. Goetz MP, Toft DO, Ames MM, Erlichman C. The Hsp90 chaperone complex as a novel target for cancer therapy. Ann Oncol 2003;4,1169-76.
19. Calderwood SK, Khaleque MA, Sawyer DB, Ciocca DR. Heat shock proteins in cancer: chaperones of tumorigenesis. Trends Biochem Sci 2006;31,164-72.
20. Niu G, Cai W, Chen K, Chen X. Non-invasive PET imaging of EGFR degradation induced by a heat shock protein 90 inhibitor. Mol Imaging Biol 2008;10,99-106.
21. Xu W, Mimnaugh E, Rosser MF, et al. Sensitivity of mature Erbb2 to geldanamycin is conferred by its kinase domain and is mediated by the chaperone protein Hsp90. J Biol Chem 2001;276,3702-8.
22. Smith-Jones PM, Solit D, Afroze F, Rosen N, Larson SM. Early tumor response to Hsp90 therapy using HER2 PET: comparison with ^{18}F-FDG PET. J Nucl Med 2006;47,793-6.
23. Niu G, Li Z, Cao Q, Chen X. Monitoring therapeutic response of human ovarian cancer to 17-DMAG by noninvasive PET imaging with ^{64}Cu-DOTA-trastuzumab. Eur J Nucl Med Mol Imaging 2009; published online at May 14.
24. Kramer-Marek G, Kiesewetter DO, Capala J. Changes in HER2 expression in breast cancer xenografts after therapy can be quantified using PET and ^{18}F-labeled affibody molecules. J Nucl Med 2009;50,1131-9

Chapter 4:

^{89}Zr-bevacizumab PET of early anti-angiogenic tumor response to treatment with HSP90 inhibitor NVP-AUY922

Wouter Nagengast[1]
Maarten de Korte[1]
Thijs Oude Munnink[1]
Hetty Timmer-Bosscha[1]
Wifred den Dunnen[2]
Harry Hollema[2]
Johan de Jong[3]
Michael Rugaard Jensen[4]
Cornelia Quadt[4]
Carlos Garcia-Echeverria[4]
Guus van Dongen[5]
Marjolijn Lub-de Hooge[2,6]
Carolina Schröder[1]
Elisabeth de Vries[1]

Departments of Medical Oncology[1], Pathology[2], Nuclear Medicine and Molecular Imaging[3], University Medical Center Groningen, Groningen, The Netherlands; Novartis Institutes for Biomedical Research[4], Basel, Switzerland; Department of Nuclear Medicine and PET Research[5], VU University Medical Center, Amsterdam, The Netherlands; Department of Hospital and Clinical Pharmacy[6], University Medical Center Groningen, Groningen, The Netherlands.

Journal of Nuclear Medicine 2010;51:761-7

ABSTRACT

Angiogenesis is a critical step in tumor development, in which vascular endothelial growth factor (VEGF) is a key growth aspect. Heat shock protein-90 (HSP90), a molecular chaperone, is essential for the activity of key proteins involved in VEGF transcription. Currently, no biomarkers to predict the effect of, or monitor, HSP90 inhibition therapy in individual patients exist. ^{89}Zr-bevacizumab PET provides a noninvasive tool to monitor tumor VEGF levels. The aim of this study was to evaluate ^{89}Zr-bevacizumab PET for early antiangiogenic tumor response evaluation of treatment with the new HSP90 inhibitor NVP-AUY922.

In xenografts of A2780 and its cisplatin-resistant CP70 human ovarian cancer subline, ^{89}Zr-bevacizumab microPET was performed before and after NVP-AUY922 treatment and was verified with histologic response and *ex vivo* tumor VEGF levels.

Compared with pretreatment values, two weeks of NVP-AUY922 treatment decreased ^{89}Zr-bevacizumab uptake with 44% (P = 0.0003) in A2780 xenografts, whereas tumor uptake was not affected in CP70 xenografts compared to pre-treatment values. The same pattern was observed in A2780 and CP70 tumor VEGF levels, measured with ELISA, and mean vessel density after NVP-AUY922 treatment. These findings coincided with reduction in the proliferation rate, assessed by Ki67 staining, in A2780 tumor tissue only.

Conclusion: ^{89}Zr-bevacizumab PET was in line with the antiangiogenic response and direct antitumor effects after NVP-AUY922 treatment, supporting the specificity of ^{89}Zr-bevacizumab PET as a sensitive technique to monitor the anti-angiogenic response of HSP90 inhibition *in vivo*.

INTRODUCTION

Angiogenesis, the formation of new blood vessels, is a critical factor involved in the development and growth of tumors.[1] An important aspect involved in angiogenesis is vascular endothelial growth factor (VEGF). VEGF production by tumor cells is thought to be regulated by hypoxemia, growth factor signaling, cytokines and cell differentiation.[1] Overexpression of VEGF occurs in many human tumor types. Therefore, targeting angiogenesis is a rational treatment approach in many cancer types.[2] Currently, this can be done by VEGF neutralizing antibodies, small molecules blocking the VEGF receptor function or by drugs inhibiting cellular tumor signaling pathways affecting angiogenesis. Inhibition of heat shock protein-90 (HSP90) is one way of affecting these pathways. HSP90 is a molecular chaperone, involved in maintaining the conformation, stability, cellular localization and activity of several key oncogenic client proteins.[3,4] HSP90 is constitutively expressed at 2 to 10-fold higher levels in cancer cells and present in active multi-chaperone complexes, conferring relative sensitivity to treatment with HSP90 inhibitors compared to their normal counterparts.[3,5] At this moment, several HSP90 inhibitors are being developed and investigated in preclinical and clinical studies. Of these, the geldanamycin analogue 17-allylamino-17-demethoxygeldanamycin (17AAG; tanespimycin) has been studied most extensively and disease stabilizations and tumor responses have been observed in phase I/II clinical trials.[6] Another class of synthetic HSP90 inhibitors is the resorcinylic pyrazole or isoxazole amide analogues, of which NVP-AUY922, an improved isoxazole resorcinol, is the most potent yet described.[6]

Currently, no biomarkers to predict the effect of, or monitor, HSP90 inhibition therapy in individual patients exist. One potential way to monitor HSP90 therapy is to prove its effect via changes in client proteins of HSP90. Client proteins of HSP90 include receptors and transcription factors like epidermal growth factor receptor-1 and -2 (EGFR and HER2), insulin-like growth factor-1 receptor (IGF1R) and hypoxia inducible factor 1α (HIF1α).[3,7] However, most of these client proteins can be measured only by collecting tumor biopsies. Therefore, molecular imaging is an attractive alternative. It allows repetitive noninvasive follow-up of specific targets. A suitable candidate is VEGF, a downstream product of various HSP90 client proteins.[1,4] Recently, it has been shown that HSP90 directed therapy leads to a reduction of VEGF secretion in tumor cell lines and a decreased mean vessel density (MVD) in tumor bearing animal models.[7-11] Because larger isoforms of

VEGF remain in the extra cellular tumor matrix, these isoforms are attractive as imaging target.[12;13] Noninvasive measurement of VEGF in the tumor might give insight in the effect of HSP90 inhibition and thus assist in tumor response prediction. Previously, we showed in a xenograft mouse model that bevacizumab, a monoclonal antibody against VEGF, radiolabeled with zirconium-89 (^{89}Zr) and indium-111 (^{111}In) can be used for *in vivo* VEGF visualization and quantification, presumably because of binding to cell- and matrix bound VEGF.[12;13] The advantage of ^{89}Zr-bevacizumab is that it allows high resolution and quantitative PET. In addition, radiolabeled bevacizumab is currently used as GMP produced tracer in clinical development.[14]

The aim of this study was to evaluate ^{89}Zr-bevacizumab PET for imaging of the early antiangiogenic tumor response after treatment with the HSP90 inhibitor NVP-AUY922. To this end, an *in vivo* mouse model was used with xenografts from ovarian cancer cell lines A2780 and its cisplatin resistant subline CP70. ^{89}Zr-bevacizumab PET was performed before and after NVP-AUY922 treatment, and the imaging results were related to histologic response and *ex vivo* tumor VEGF levels.

MATERIALS AND METHODS

Cell lines and in vitro experiments

A2780 and its 7-fold cisplatin resistant subline CP70 were kindly provided by Dr. Thomas C. Hamilton (Fox Chase Cancer Center). All cells were cultured in RPMI 1640 (Invitrogen), supplemented with 10% heat inactivated fetal calf serum (Bodinco BV) and 2 mM L-glutamine (Invitrogen) at 37 °C in a fully humidified atmosphere containing 5% CO_2. Cells were subcultured three times per week.

For *in vitro* experiments, NVP-AUY922 was dissolved in DMSO at 10 mM, and stored at -80 °C. A2780 and CP70 cells were plated (3 x 10^5 cells per well in 3 mL) and treated with 50 and 100 nM NVP-AUY922, respectively; relevant plasma levels in mice; or control medium ($n \geq 3$).[6;15] After 24 h of incubation, supernatant was collected and centrifuged at 180 g for 15 min. Supernatant samples were stored at -20 °C until analysis. VEGF levels were determined with the human VEGF ELISA kit (R&D Systems) according to the manufacturer's protocol.

Conjugation and ^{89}Zr-labeling of bevacizumab

Conjugation and labeling of bevacizumab were performed as described previously.[13;16] In short, the chelate desferrioxamine B (desferal, Novartis) was succinylated (*N*-suc-desferrioxamine), temporarily filled with stable iron [Fe(III)], and coupled to the lysine residues of bevacizumab by means of a tetrafluorophenol-*N*-suc-desferrioxamine ester. Conjugation was performed at room temperature for 30 min at pH 9.5-9.7. After conjugation, the mixture was set to pH 4.2-4.4 (0.1 mol/L H_2SO_4) and 50 µL of 25 mg/mL ethylenediaminetetraacetic acid (Calbiochem) were added to remove Fe(III). The solution was incubated 30 min at 35 °C, and purified by ultrafiltration, diluted in water for injection (5 mg/mL) and stored at -20 °C. Labeling was performed with ^{89}Zr (half-life, 78,4 h) produced by Cyclotron BV. In brief, the ^{89}Zr-oxalate solution was set at pH 3.9-4.2 and mixed for 3 min. With 4-(2-hydroxyethyl)-1-piperazineethanesulfonic acid (Sigma-Aldrich) buffer the solution was adjusted to pH 6.7-6.9. N-suc-desferrioxamine-bevacizumab was added and incubated for 45 min at room temperature.

Animals

Tumor cells for xenografting were harvested by trypsinization and resuspended in RPMI 1640 and Matrigel™ (BD Bioscience). *In vivo* imaging and *ex vivo* biodistribution experiments were conducted using male nude BALB/c mice (BALB/cOlaHSD-foxn^{nu}) obtained from Harlan Nederland. At 6-8 wk of age the mice were injected subcutaneously with 5x10^6 A2780 or CP70 cells mixed with 0.1 mL Matrigel™. When the tumor measured between 6 and 8 mm in diameter (± 0.3 cm^3, for A2780 2 weeks after injection, for CP70 3-4 weeks after injection) *in vivo* studies were started.

MicroPET imaging and ex vivo biodistribution

^{89}Zr-bevacizumab (4 ± 0.27 MBq, ± 5 µg) was injected into the penile vein. During a scan sequence, images were made 24 h and 144 h postinjection of the tracer. Two scan sequences were obtaned, before and after NVP-AUY922 treatment. Animals were imaged using a microPET Focus 220 rodent scanner (CTI Siemens). Static images (30 min acquisition time) were obtained. After image reconstruction, *in vivo* quantification was performed with AMIDE Medical Image Data Examiner

software (version 0.9.1; Stanford University).[17] For the quantification of radioactivity within the tumor, 3D volumes of interest were manually drawn using the 3D freehand tool, plane by plane, pixel by pixel, with no change in thresholds. The total injected dose was calculated by decay correction of the total activity present at 24 h after injection in the animal, at which time the clearance of the injected antibodies is considered to be almost negligible, as described earlier.[13] The data are presented as the percentage injected dose per gram tissue (%ID/g), assuming a tissue density of 1 g/cm^3. Animals were sacrificed after the last scan (144 h, second scan sequence) and organs and tissues were excised, rinsed for residual blood and weighed. Samples and primed standards were counted for radioactivity in a calibrated well-type LKB-1282-Compu-gamma system (LKB Wallac) and corrected for physical decay. Tissue activity is expressed as %ID/g. Harvested tumors were divided, immediately frozen at -80 °C, and paraffin embedded for further analysis.

A2780 tumors are growing rapidly, with a doubling time of 3-6 d.[6;18-20] It was considered unachievable to maintain these tumors in the untreated animals for the duration of the drug treatment of the other animals, because the tumors would grow unacceptably large. Therefore, for *ex vivo* comparison non-treated control animals were sacrificed after the first administration of ^{89}Zr-bevacizumab, comparable to the pretreatment scan of the animals treated with NVP-AUY922. Non-treated control animals (A2780 n=6, CP70 n=5) were injected with ^{89}Zr-bevacizumab (4 ± 0.27 MBq, ± 5 μg) and mice were sacrificed 144 h postinjection of tracer. *Ex vivo* biodistribution was performed as described above.

All animal experiments were performed with isofluran inhalation anesthesia (induction 3%; maintenance 1.5%).

NVP-AUY922 treatment

NVP-AUY922 was formulated in water containing 5% glucose and administrated at 50 mg/kg twice weekly intraperitoneally (volume 6.5 ml/kg). Treatment was started immediately after the first (pretreatment) scan sequence (A2780 n=8, CP70 n=6). After 2 weeks of treatment, mice received a second administration of ^{89}Zr-bevacizumab, and a second scan sequence was performed. NVP-AUY922 treatment was continued during this sequence.

All animal experiments were approved by the animal experiments committee of the University of Groningen.

Determination of antiangiogenic response

From frozen tumors, 3 random samples were lysed manually using mammalian protein extraction reagent (Pierce). Thereafter, mixtures were centrifuged at 20,000 g for 15 min and subsequently stored at -20 °C until analysis. The protein concentration of the samples was determined by a Bradford assay.[21] VEGF levels were measured as described above. Data are presented as picogram VEGF per milligram protein.

Paraffin-embedded tumors were stained with antibodies against von Willebrand factor, Ki67 (Dako) and hematoxylin and eosin staining (HE). The mean vessel density (MVD) was scored in 3 areas, defined as hot-spot areas with the maximum number of microvessels, as described earlier.[13] The proliferation index was calculated by percentage of Ki67 positive cells in at least 3 high-power fields (400x) using a calibrated grid. HE staining was performed to assess areas of necrosis. Areas were scored as percentage necrosis and vital tumor tissue per slide.

Statistical analysis

Data are presented as mean ± standard error of the mean (SEM). Statistical analysis was performed using the Mann-Whitney test for nonparametric data and a paired sampled T-test for paired data (SPSS, version 14, Chicago, IL). A P value of 0.05 or less was considered significant.

RESULTS

NVP-AUY922 decreases VEGF secretion in A2780 cells *in vitro*

Following 24 h of incubation, VEGF levels in the culture medium of nontreated A2780 cells were higher (1.8-fold) than those in the culture medium of non-treated CP70 cells (P = 0.042). Treatment of the A2780 cells with 50 nM NVP-AUY922 for 24 h resulted in 43.2% (P = 0.038) reduction of VEGF levels in the culture medium, compared with the culture medium of nontreated cells (Fig. 1). VEGF levels in the culture medium of CP70 cells were not significantly decreased (namely 23.8% lower, P = 0.20). Increased doses of NVP-AUY922 up to 100 nM did not further reduce VEGF secretion by A2780 or CP70 cells.

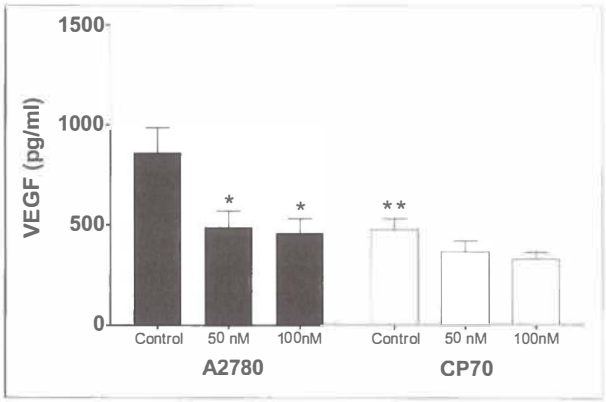

Figure 1. Effect of HSP90 inhibition by NVP-AUY922 on VEGF secretion. A2780 and CP70 tumor cells were incubated for 24 h in 50 and 100 nM NVP-AUY922, or control medium (*$P < 0.05$). Control VEGF levels of A2780 cells were higher compared to control CP70 (**$P < 0.05$). Data is presented as mean ± SEM.

^{89}Zr-bevacizumab uptake decreases in A2780 tumors after NVP-AUY922 treatment

PET 144 h postinjection showed clear tumor localization of ^{89}Zr-bevacizumab in the A2780 and CP70 xenograft model (Fig. 2). ^{89}Zr-bevacizumab uptake was homogeneous within the tumor. Before treatment, ^{89}Zr-bevacizumab tumor uptake in A2780 xenografts (12.9 ± 2.2 %ID/g, 144 h postinjection) was higher ($P < 0.0001$) than that in CP70 xenografts (6.9 ± 1.0 %ID/g). Twice weekly treatment with 50 mg/kg NVP-AUY922 decreased ^{89}Zr-bevacizumab uptake with 44% ($P = 0.0003$), compared with pretreatment, as quantified by microPET at 144 h postinjection of ^{89}Zr-bevacizumab (Fig. 3).

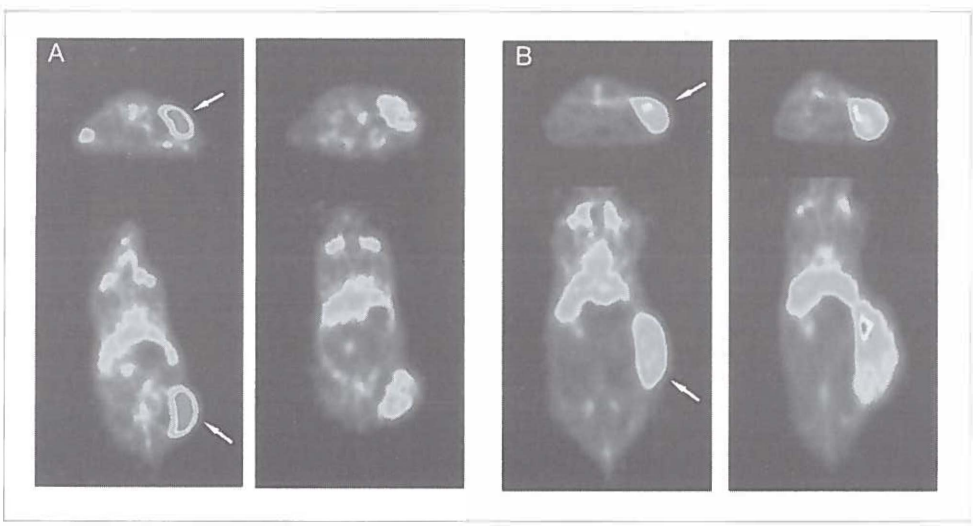

Figure 2. Representative transversal and coronal microPET images of ^{89}Zr-bevacizumab obtained before treatment of A2780 (A) and CP70 (B) xenografts (left panels), and after NVP-AUY922 treatment (right panels). Images were obtained at 144 h after injection of ^{89}Zr-bevacizumab. Tumor is indicated by arrow. See page 168 for full color image.

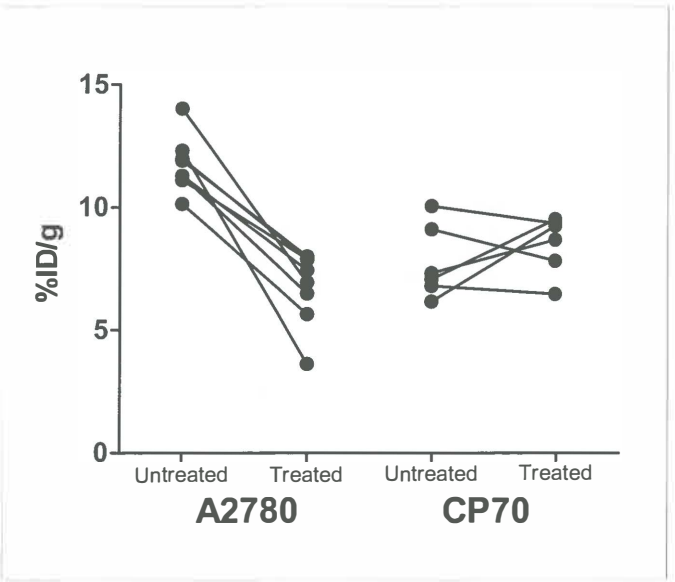

Figure 3. Individual micro-PET quantification of A2780 and CP70 xenografts before and after NVP-AUY922 treatment.

Similar results were seen in *ex vivo* biodistribution experiments, in which ^{89}Zr-bevacizumab uptake was 48% lower (P = 0.029) in NVP-AUY922 treated versus nontreated animals (Fig. 4A). A2780 tumors grew rapidly, with a doubling time of 3-6 d.[6;18-20] In our study, volumes (assessed by microPET, which correlated nicely with *ex vivo* tumor weight (r^2=0.95)) of NVP-AUY922 treated A2780 tumors increased only moderately (2.2 ± 0.2 fold) during the study period (3 wk), indicating an effect of NVP-AUY922 on tumor growth.

In contrast to A2780, treatment with NVP-AUY922 did not change ^{89}Zr-bevacizumab tumor uptake in CP70 xenografts compared to pretreatment tumor uptake (namely an increase of 8%, P = 0.475) as quantified by microPET (Fig. 3). Similar results were seen with *ex vivo* biodistribution studies of nontreated versus treated CP70 tumors (27% increase, P = 0.125). Tumor volumes increased 2.1 ± 0.5 fold during the study period (3 wk), which is comparable to the growth rate before the start of the study in that time. Treatment with NVP-AUY922 did not change normal organ (nontumor) biodistribution of ^{89}Zr-bevacizumab between treated and nontreated tumor bearing mice (all organs $P > 0.05$) (Fig. 4C).

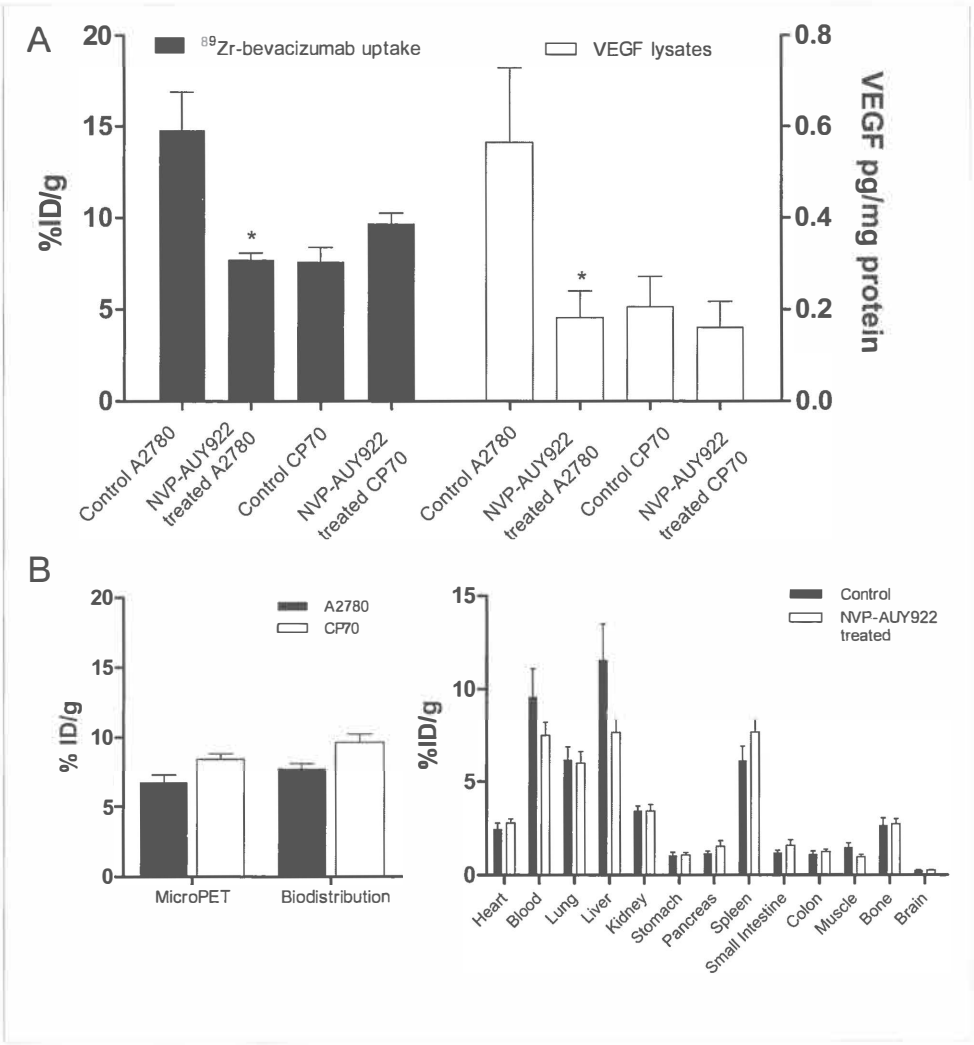

Figure 4. (A) *Ex vivo* tumor biodistribution of ^{89}Zr-bevacizumab and tumor lysate VEGF levels in control and NVP-AUY922 treated A2780 and CP70 xenografts (* $P < 0.05$). (B) MicroPET quantification and *ex vivo* biodistribution of ^{89}Zr-bevacizumab after NVP-AUY922 treatment, and *ex vivo* organ biodistribution (right) of ^{89}Zr-bevacizumab in control (n=11) and NVP-AUY922 treated (n=14) animals. Data are presented as mean ± SEM.

^{89}Zr-bevacizumab imaging corresponds with tumor VEGF levels in A2780 and CP70 xenografts before and after NVP-AUY922 treatment

To verify that changes in ^{89}Zr-bevacizumab tumor uptake were VEGF driven, tumor VEGF levels of nontreated control mice were compared with VEGF levels of NVP-AUY922 treated (50 mg/kg, twice weekly) mice in both A2780 and CP70

xenografts by quantitative ELISA. In A2780 xenografts, tumor VEGF levels were 69% lower (P = 0.041) after NVP-AUY922 treatment, whereas no significant change of VEGF levels was found in CP70 (20% reduction, P = 0.61). These results correspond to ^{89}Zr-bevacizumab tumor uptake as assessed by biodistribution in these animals (Fig. 4A). Both ^{89}Zr-bevacizumab tumor uptake and tumor VEGF levels are lower after NVP-AUY922 treatment in A2780 xenografts, compared with controls. However, this is not the case for CP70 xenografts. Furthermore, higher initial VEGF levels in A2780 versus CP70 are in line with the ^{89}Zr-bevacizumab biodistribution findings in these animals. In the present study, microPET quantification was comparable to *ex vivo* biodistribution (Fig. 4B), as described earlier.[13] Therefore, these results demonstrate that changes in ^{89}Zr-bevacizumab microPET imaging correspond with changes in tumor VEGF levels by NVP-AUY922 mediated HSP90 inhibition.

NVP-AUY922 treatment decreases MVD and Ki67 staining in responding A2780 tumors

The MVD was 60% lower (P = 0.005) in NVP-AUY922 treated A2780 tumors compared to nontreated tumors (Fig. 5). This lower MVD shows that in A2780 tumors a decrease in VEGF secretion is accompanied by an antiangiogenic effect in A2780, as determined histologically, after NVP-AUY922. Additionally, antipro-

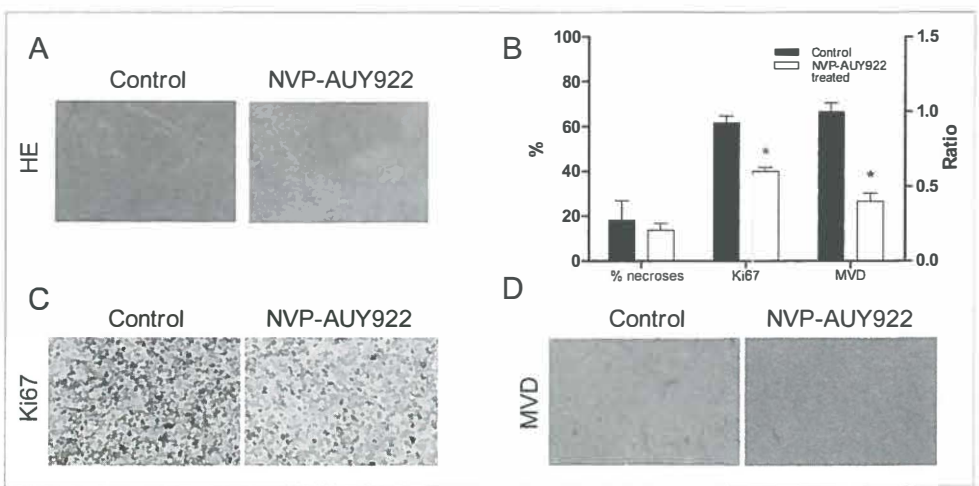

Figure 5. (A) Representative hematoxylin and eosin (HE) staining, (B) percentage necroses, Ki67 staining and MVD (right Y-axis) (* $P < 0.05$), (C) representative Ki67 staining, and (D) representative von Willebrand factor staining for MVD of control and NVP-AUY922 treated A2780 xenograft. Data are presented as mean ± SEM. See page 168 for full color image.

liferative effects were seen in A2780 xenografts (proliferation index reduced by 35%, $P = 0.023$), indicating also that a direct tumor effect occurred parallel to anti-angiogenic effects after NVP-AUY922 treatment (Fig. 5). In CP70 tumors, no differences in MVD ($P = 0.720$) and proliferation rate ($P = 0.688$) were observed, which is compatible with the findings on ^{89}Zr-bevacizumab PET and tumor VEGF levels in this tumor cell line (data not shown).

Furthermore, in neither A2780 nor CP70 xenografts did 2 wk of NVP-AUY922 treatment resulted in increased tumor necrosis as shown by HE staining. In NVP-AUY922 treated as well as nontreated xenografts, at least 80% of the tumor consisted of vital areas (Fig. 5). Therefore, decreased ^{89}Zr-bevacizumab tumor uptake in A2780 was not due to increased tumor necrosis.

DISCUSSION

In the present study, we have demonstrated that the antiangiogenic effect of HSP90 inhibition can be adequately monitored *in vivo* using ^{89}Zr-bevacizumab PET. The specificity of the technique is illustrated by the fact that a decreased ^{89}Zr-bevacizumab uptake is related to the presence of an antiangiogenic response (confirmed by means of decreased VEGF levels and MVD) in the A2780 model, whereas no change in ^{89}Zr-bevacizumab uptake was observed in the nonresponsive CP70 model. Additionally, the extent of antiangiogenic response was related to the antiproliferative effect of the NVP-AUY922 treatment. Thus, ^{89}Zr-bevacizumab PET allows *in vivo* visualization and quantification of early antiangiogenic tumor response to treatment with HSP90 inhibition. As such, it may be used as an early biomarker for the effect of HSP90 inhibition.

It is thought that reduction of VEGF secretion by tumor cells after HSP90 inhibition is mediated via multiple pathways. For example, HSP90 inhibition by 17AAG reduced epidermal growth factor, insulin-like growth factor-1, betacellulin, transforming growth factor-α (TGF-α), and heregulin β1-induced VEGF secretion by tumor cells *in vitro*.[7,9,11] In prostate cancer cells, geldanamycin treatment decreased HIF1α levels, which corresponded with lower VEGF levels *in vitro*.[8]

In addition, HSP90 inhibition has demonstrated antiangiogenic effects *in vivo*. We observed in our A2780 xenograft model a decreased MVD after NVP-AUY922 treatment. Similar effects were observed in a human glioblastoma xenograft model.[6] Furthermore, it was shown that NVP-AUY922 inhibited endothelial cell

function and migration, decreased VEGF-R2 levels on endothelial cells and reduced HIF1α levels in a human glioblastoma xenograft model.[6] These results are comparable to the effects seen with other HSP90 inhibitors. Treatment with 17AAG and 17-(dimethylaminoethyl-amino)-17-demethoxygeldanamycin (17DMAG; alvespimycin), a water soluble geldanamycin analogue, decreased MVD in gastric, colon and hepatocellular carcinoma xenograft models.[7;11;22;23] Additionally, 17DMAG downregulated VEGF-R2 protein expression on endothelial cells, inhibited VEGF-A induced Erk and Akt activation, and down-regulated total-Akt expression.[24] Furthermore, treatment with 17DMAG decreased platelet-derived growth factor R-β expression and function on vascular smooth muscle cells.[24] All these results signify the antiangiogenic effect of HSP90 inhibition in cancer.

In the present study, we investigated whether this antiangiogenic effect by HSP90 inhibition could be monitored by ^{89}Zr-bevavizumab PET. Previously, it was shown that NVP-AUY922 treatment induced HSP70 and decreased c-Raf and cyclin-dependent kinase 4 in A2780 cells, indicating sufficient sensitivity of this cell line to HSP90 inhibition.[6] We treated A2780 and CP70 tumor bearing mice with comparable dosing schemes which showed efficiency in other xenograft models.[6,15] Daily dosing of 50 mg/kg NVP-AUY922 during 7 d reduced tumor growth by 90% in A2780 xenografts, compared to non-treated animals.[6] We showed with microPET quantification a vast decrease of ^{89}Zr-bevacizumab tumor uptake in A2780 xenografts, whereas no decrease in ^{89}Zr-bevacizumab uptake was seen in CP70 xenografts. In a HER2 overexpressing xenograft model, in which we evaluated NVP-AUY922 treatment with ^{89}Zr-trastuzumab, we did not observe changes in tumor uptake of radiolabeled control IgG after NVP-AUY922, suggesting that minimal changes in antibody uptake occur due to alterations in perfusion and extravasation.[25] Previously, we showed that ^{89}Zr-bevacizumab accumulates in tumor blood vessels and its extracellular matrix, presumably because of localization of large human VEGF isoforms. No binding takes place to mouse derived VEGF.[12;13] To verify whether changes in ^{89}Zr-bevacizumab uptake also reflect changes in total tumor human VEGF levels, we assessed VEGF levels in tumor lysates. The *ex vivo* VEGF ELISA we used, detects both extra- and intra cellular human VEGF in tumor lysates. Most likely, equilibrium is present between extracellular and intracellular VEGF. VEGF levels in A2780 xenograft were higher than in CP70 xenografts and they decreased after HSP90 inhibition, whereas VEGF levels in CP70 did not change. These results are in line with our

^{89}Zr-bevacizumab imaging results and demonstrate that ^{89}Zr-bevacizumab microPET imaging can quantify noninvasively both absolute differences between VEGF levels in tumors and changes in VEGF levels after therapy.

These *in vivo* results mimic our *in vitro* experiments, in which initial CP70 VEGF secretion levels were lower than A2780 VEGF secretion levels, and no significant effect of HSP90 therapy was observed. It is not completely clear why CP70 did not respond to HSP90 inhibition, and why initial VEGF levels were lower compared to A2780. Several studies have demonstrated a complex interaction between cisplatin and HSP90. Cisplatin can bind to the C-terminal domain of HSP90, promoting a conformational change in HSP90, whereas HSP90 inhibitors interact with the N-terminal domain of HSP90.[26] Combined treatment of cisplatin and HSP90 inhibition has shown additive and antagonistic effects in colon and ovarian tumor cell lines.[18;27;28] For instance, in A2780 tumor cells concomitant administration of 17AAG and carboplatin was antagonistic *in vitro*, whereas 17AAG followed by carboplatin or vice versa was additive both *in vitro* and *in vivo*.[18] Future studies should elucidate the interaction between cisplatin and HSP90 therapy in both cisplatin sensitive and resistant models. This complexity does, however, point to the relevance of an early predictive factor.[29]

Other client proteins that have been used for noninvasive monitoring of HSP90 therapy are HER2 and EGFR. Smith-Jones et al. demonstrated that the early degradation of HER2 (-50%) during 17AAG therapy could be monitored by microPET imaging in a BT474 breast cancer xenograft model, using ^{68}Ga-DCHF, a F(ab')$_2$ fragment of the HER2 antibody trastuzumab.[30;31] Furthermore, decreased HER2 expression measured by microPET corresponded to reduced tumor growth. In contrast, tumor uptake of ^{18}F-FDG (the most widely used tumor tracer, which visualizes glucose uptake) did not change after HSP90 therapy.[31] Likewise, ^{64}Cu-DOTA-cetuximab was used to monitor EGFR degradation by 17AAG in a PC-3 prostate cancer xenograft model.[32] Uptake of ^{64}Cu-DOTA-cetuximab in 17AAG treated animals was lower (-39%) compared to non-treated animals 48 h after the last administration of 17AAG, which corresponded to a decreased EGFR staining in tumor samples. In contrast to EGFR and HER2, which are abundantly expressed in a selected group of cancer patients, VEGF plays an important, universal role in cancer; therefore ^{89}Zr-bevacizumab imaging is likely to be more widely applicable to the monitoring of HSP90 inhibition.

Conclusion

^{89}Zr-bevacizumab PET was in line with the antiangiogenic response and direct antitumor effects after NVP-AUY922 treatment, supporting the specificity of ^{89}Zr-bevacizumab PET as a sensitive technique to monitor the antiangiogenic response of HSP90 inhibition *in vivo*. Exploration of ^{89}Zr-bevacizumab PET in phase II studies as an early predictive marker during HSP90 inhibition has been started.

Conflict of interest statement

MRJ, CQ, CG are employees and stockholders of Novartis Pharma AG.

Acknowledgments

This study was supported by a personal grant to one of the authors and grants RUG 2007-3739 and RUG 2009-4273 of the Dutch Cancer Society.

References

1. Ferrara N, Davis-Smyth T. The biology of vascular endothelial growth factor. *Endocr Rev*. 1997;18:4-25.
2. Gerber HP, Ferrara N. Pharmacology and pharmacodynamics of bevacizumab as monotherapy or in combination with cytotoxic therapy in preclinical studies. *Cancer Res*. 2005;65:671-680.
3. Xu W, Neckers L. Targeting the molecular chaperone heat shock protein 90 provides a multifaceted effect on diverse cell signaling pathways of cancer cells. *Clin Cancer Res*. 2007;13:1625-1629.
4. Neckers L. Heat shock protein 90: the cancer chaperone. *J Biosci*. 2007;32:517-530.
5. Kamal A, Thao L, Sensintaffar J et al. A high-affinity conformation of Hsp90 confers tumour selectivity on Hsp90 inhibitors. *Nature*. 2003;425:407-410.
6. Eccles SA, Massey A, Raynaud FI et al. NVP-AUY922: a novel heat shock protein 90 inhibitor active against xenograft tumor growth, angiogenesis, and metastasis. *Cancer Res*. 2008;68:2850-2860.
7. Sanderson S, Valenti M, Gowan S et al. Benzoquinone ansamycin heat shock protein 90 inhibitors modulate multiple functions required for tumor angiogenesis. *Mol Cancer Ther*. 2006;5:522-532.
8. Alqawi O, Moghaddas M, Singh G. Effects of geldanamycin on HIF-1alpha mediated angiogenesis and invasion in prostate cancer cells. *Prostate Cancer Prostatic Dis*. 2006;9:126-135.
9. Lang SA, Moser C, Gaumann A et al. Targeting heat shock protein 90 in pancreatic cancer impairs insulin-like growth factor-I receptor signaling, disrupts an interleukin-6/signal-transducer and activator of transcription 3/hypoxia-inducible factor-1alpha autocrine loop, and reduces orthotopic tumor growth. *Clin Cancer Res*. 2007;13:6459-6468.
10. Cao X, Jia G, Zhang T et al. Non-invasive MRI tumor imaging and synergistic anticancer effect of HSP90 inhibitor and glycolysis inhibitor in RIP1-Tag2 transgenic pancreatic tumor model. *Cancer Chemother Pharmacol*. 2008;62:985-994.
11. Lang SA, Klein D, Moser C et al. Inhibition of heat shock protein 90 impairs epidermal growth factor-mediated signaling in gastric cancer cells and reduces tumor growth and vascularization in vivo. *Mol Cancer Ther*. 2007;6:1123-1132.
12. Park JE, Keller GA, Ferrara N. The vascular endothelial growth factor (VEGF) isoforms: differential deposition into the subepithelial extracellular matrix and bioactivity of extracellular matrix-bound VEGF. *Mol Biol Cell*. 1993;4:1317-1326.

13. Nagengast WB, De Vries EG, Hospers GA et al. In vivo VEGF imaging with radiolabeled bevacizumab in a human ovarian tumor xenograft. *J Nucl Med*. 2007;48:1313-1319.
14. Nagengast WB, Lub-De Hooge MN, Hospers GA et al. Towards clinical VEGF imaging using the anti-VEGF antibody bevacizumab and Fab-fragment ranibizumab. *J Clin Oncol*. 2008; May 20 suppl:3547
15. Jensen MR, Schoepfer J, Radimerski T et al. NVP-AUY922: a small molecule HSP90 inhibitor with potent antitumor activity in preclinical breast cancer models. *Breast Cancer Res*. 2008;10:R33.
16. Verel I, Visser GW, Boerman OC et al. Long-lived positron emitters zirconium-89 and iodine-124 for scouting of therapeutic radioimmunoconjugates with PET. *Cancer Biother Radiopharm*. 2003;18:655-661.
17. Loening AM, Gambhir SS. AMIDE: a free software tool for multimodality medical image analysis. *Mol Imaging*. 2003;2:131-137.
18. Banerji U, Sain N, Sharp SY et al. An *in vitro* and in vivo study of the combination of the heat shock protein inhibitor 17-allylamino-17-demethoxygeldanamycin and carboplatin in human ovarian cancer models. *Cancer Chemother Pharmacol*. 2008;62:769-778
19. Arts J, Angibaud P, Marien A et al. R306465 is a novel potent inhibitor of class I histone deacetylases with broad-spectrum antitumoral activity against solid and haematological malignancies. *Br J Cancer*. 2007;97:1344-1353.
20. Taylor SA, Marrinan CH, Liu G et al. Combining the farnesyltransferase inhibitor lonafarnib with paclitaxel results in enhanced growth inhibitory effects on human ovarian cancer models *in vitro* and *in vivo*. *Gynecol Oncol*. 2008;109:97-106.
21. Bradford MM. A rapid and sensitive method for the quantitation of microgram quantities of protein utilizing the principle of protein-dye binding. *Anal Biochem*. 1976;72:248-254.
22. Moser C, Lang SA, Kainz S et al. Blocking heat shock protein-90 inhibits the invasive properties and hepatic growth of human colon cancer cells and improves the efficacy of oxaliplatin in p53-deficient colon cancer tumors in vivo. *Mol Cancer Ther*. 2007;6:2868-2878.
23. Park JH, Kim SH, Choi MC et al. Class II histone deacetylases play pivotal roles in heat shock protein 90-mediated proteasomal degradation of vascular endothelial growth factor receptors. *Biochem Biophys Res Commun*. 2008;368:318-322.
24. Lang SA, Moser C, Fichnter-Feigl S et al. Targeting heat-shock protein 90 improves efficacy of rapamycin in a model of hepatocellular carcinoma in mice. *Hepatology*. 2008;49:523-532.

25. Oude Munnink TH, de Korte MA, Nagengast WB et al. ^{89}Zr-trastuzumab PET visualises HER2 downregulation by the HSP90 inhibitor NVP-AUY922 in a human tumour xenograft. *Eur J Cancer* 2010;46:678-684
26. Marcu MG, Neckers LM. The C-terminal half of heat shock protein 90 represents a second site for pharmacologic intervention in chaperone function. *Curr Cancer Drug Targets*. 2003;3:343-347.
27. Vasilevskaya IA, Rakitina TV, O'Dwyer PJ. Quantitative effects on c-Jun N-terminal protein kinase signaling determine synergistic interaction of cisplatin and 17-allylamino-17-demethoxygeldanamycin in colon cancer cell lines. *Mol Pharmacol*. 2004;65:235-243.
28. Bagatell R, Beliakoff J, David CL, Marron MT, Whitesell L. Hsp90 inhibitors deplete key anti-apoptotic proteins in pediatric solid tumor cells and demonstrate synergistic anticancer activity with cisplatin. *Int J Cancer*. 2005;113:179-188.
29. Oldenhuis CN, Oosting SF, Gietema JA, De Vries EG. Prognostic versus predictive value of biomarkers in oncology. *Eur J Cancer*. 2008;44:946-953.
30. Smith-Jones PM, Solit DB, Akhurst T, Afroze F, Rosen N, Larson SM. Imaging the pharmacodynamics of HER2 degradation in response to Hsp90 inhibitors. *Nat Biotechnol*. 2004;22:701-706.
31. Smith-Jones PM, Solit D, Afroze F, Rosen N, Larson SM. Early tumor response to Hsp90 therapy using HER2 PET: comparison with 18F-FDG PET. *J Nucl Med*. 2006;47:793-796.
32. Niu G, Cai W, Chen K, Chen X. Non-invasive PET imaging of EGFR degradation induced by a heat shock protein 90 inhibitor. *Mol Imaging Biol*. 2008;10:99-106.

Chapter 5:

Lapatinib and 17AAG reduce ^{89}Zr-trastuzumab-F(ab')$_2$ uptake in SKBR3 tumor xenografts

Thijs Oude Munnink[1]
Elisabeth de Vries[1]
Silke Vedelaar[1]
Hetty Timmer-Bosscha[1]
Carolina Schröder[1]
Adrienne Brouwers[2]
Marjolijn Lub-de Hooge[2,3]

Departments of Medical Oncology[1], Nuclear Medicine and Molecular Imaging[2], Hospital and Clinical Pharmacy[3], University Medical Center Groningen, Groningen, The Netherlands

ABSTRACT

Human epidermal growth factor receptor-2 (HER2) directed therapy might be improved by insight in drug effects on HER2 expression. This study evaluates the effects of the EGFR/HER2 tyrosine kinase inhibitor lapatinib, the heat shock protein-90 inhibitor 17AAG, and their combination, on HER2 expression with *in vivo* HER2-PET imaging.

Lapatinib and 17AAG effects on EGFR and HER2 membrane expression were determined *in vitro* using flow cytometry of human SKBR3 tumor cells. Effect of lapatinib on HER2 internalization was studied *in vitro* by ^{89}Zr-trastuzumab-F(ab')$_2$ internalization. For *in vivo* evaluation, ^{89}Zr-trastuzumab-F(ab')$_2$ μPET imaging was performed two times with a 7 day interval. Lapatinib was given for 6 days, starting 1 day after the baseline scan. 17AAG was given 1 day before the second ^{89}Zr-trastuzumab-F(ab')$_2$ injection. Imaging data were compared with *ex vivo* biodistribution analysis and HER2 immunohistochemical staining.

17AAG treatment lowered EGFR expression by 41% (P = 0.016) and HER2 by 76% (P = 0.022). EGFR/HER2 downregulation by 17AAG was inhibited by lapatinib pretreatment. Lapatinib reduced internalization of ^{89}Zr-trastuzumab-F(ab')$_2$ with 25% (P = 0.0022). ^{89}Zr-trastuzumab-F(ab')$_2$ tumor to blood ratio was lowered 32% by lapatinib (P = 0.00004), 34% by 17AAG (P = 0.0022) and even 53% by the combination (P = 0.011).

Lapatinib inhibits HER2 internalization and 17AAG lowers HER2 membrane expression. Both drugs reduce ^{89}Zr-trastuzumab-F(ab')$_2$ tumor uptake. The combination of these drugs therefore deserves further investigation.

INTRODUCTION

Human epidermal growth factor receptor-2 (HER2) is a potent pro-oncogenic factor which is involved in tumor cell survival, proliferation, maturation, metastasis and angiogenesis. HER2 targeted therapy is of clear importance for patients with HER2 overexpressing breast or gastric cancers.[1-4] The monoclonal antibody trastuzumab, which binds to the extracellular domain of HER2, is part of the treatment of HER2 positive breast cancer[5;6] and metastatic gastric cancer.[7] However most of the patients with HER2 positive metastatic breast or gastric cancer will eventually develop progressive disease on a trastuzumab containing regimen. Therefore several new approaches are under investigation. Options in this setting are intensifying HER2 blockade or targeting alternative growth signaling pathways in tumor cells that bypass HER2 blockade.[3;8;9]

New data indicate that intensifying HER2 blockade by combining trastuzumab with the ERFR/HER2 tyrosine kinase inhibitor lapatinib can be more effective than both drugs separately in patients with HER2 positive breast cancer.[10;11] Other novel HER2 targeting strategies include the HER2 dimerization inhibitor pertuzumab, the antibody drug conjugate trastuzumab-DM1, and inhibitors of the multichaperone heat shock protein-90 (HSP90).[3] HER2 is dependent on HSP90 for its conformation, activation, functionality and stability. Inhibition of HSP90 leads to a rapid but transient HER2 degradation.[12-16] In patients with HER2 positive metastatic breast cancer, who progressed on trastuzumab based regimens, antitumor activity of the HSP90 inhibitor 17-(allylamino)-17-demethoxygeldanamycin (17AAG; tanespimycin) in combination with trastuzumab was seen.[17]

A rational designed drug combination for optimal HER2 blockade is of clear interest. A better understanding of the pharmacodynamic effects of HER2 targeting drugs on HER2 expression and dynamics will likely contribute to this. Trastuzumab, pertuzumab and trastuzumab-DM1 bind the extracellular domain of HER2 and therefore require HER2 overexpression at the tumor cell membrane.[3] HSP90 inhibition downregulates HER2,[14-16] while lapatinib stabilizes and upregulates HER2 at the tumor cell membrane.[18] Lapatinib also cleaves the extracellular domain of HER2.[19] These different effects on HER2 make it of interest to study the effect of HSP90 inhibition and lapatinib on HER2 expression.

HER2-positron emission tomography (PET) imaging in preclinical experiments as well as in metastatic breast cancer patients using zirconium-89 (^{89}Zr) labeled

trastuzumab is feasible.[20;21] In addition ^{89}Zr-trastuzumab PET scanning allows monitoring of HER2 degradation after HSP90 inhibition.[16]

The aim of the present study is to analyze the effects of lapatinib, 17AAG and their combination on HER2 expression and dynamics *in vivo* with HER2-PET imaging.

MATERIALS AND METHODS

Cell cultures and chemicals

The HER2 overexpressing human breast cancer cell-line SKBR3 was obtained from American Type Culture Collection. Cells were cultured in a humidified incubator at 5% CO2 and 37 ^{0}C in D-MEM high glucose, supplemented with 10% fetal calf serum (FCS). Lapatinib (di-*p*-toluenesulfonate salt) and 17AAG were purchased from LC Laboratories. For *in vitro* experiments lapatinib and 17AAG were dissolved in dimethyl sulfoxide (DMSO) and stored at -20 ^{0}C. For *in vivo* experiments, lapatinib was freshly suspended in water containing 0.5% hydroxymethylpropyl cellulose and 0.1% Tween 80, and 17AAG was freshly suspended in 10% DMSO and 0.5% Tween 80 in phosphate buffered saline (PBS).

Flow cytometry, Western blot and cytotoxicity assay

For flow cytometry, cells were incubated with 100 or 300 nM lapatinib for 40 h and/or 500 nM 17AAG for 24 h (combination treatment started with 16 h lapatinib alone followed by 24 h of lapatinib and 17AAG combined). Concentrations and incubation time of lapatinib were adapted from Scaltriti et al[18] and 17AAG treatment was based on our previous results.[16] Cells were harvested with trypsin and washed with cold PBS. For flow cytometric analysis (FACSCalibur, BD Biosciences) of receptor expression, cells were incubated with trastuzumab (humanized anti-HER2) and cetuximab (chimeric anti-EGFR) followed by incubation with FITC conjugated monoclonal anti-human IgG2a (Clone HP 6017, Sigma). Membrane expression was calculated as mean fluorescent intensity (MFI) and expressed as percentage of control from at least three independent experiments.

For Western blots, cells were incubated with 100 or 300 nM lapatinib for 40 h and/or 50 or 200 nM 17AAG for 24 h. Combination treatment started with 16 h

lapatinib alone followed by 24 h of lapatinib and 17AAG combined. Cell lysates were prepared using mammalian protein extraction reagent (Pierce). Protein concentrations were estimated with a Bradford assay. Total cell lysates were separated on 10% polyacrylamide gel and transferred onto activated polyvinylidene difluoride membranes (Millipore). After blocking for 1 h in Tris-buffered saline supplemented with 5% skimmed milk (Fluka) and 0.05% Tween-20 (Sigma-Aldrich), immunodetection of the protein of interest was performed according to the manufacturer's protocol. Phosphorylation of extracellular regulated-signal kinase (ERK) was used as readout for HER2/EGFR signaling. Primary antibodies against human ERK and phosphorylated ERK (both from Cell Signaling) and horseradish peroxidase labeled secondary antibody (DAKO) were used. Proteins were visualized using Lumi-Light reagent (Roche Diagnostics). Expression of β-actin served as control.

For cytotoxicity analysis, cells were pre-incubated with lapatinib (0, 100, 300, 500 nM) or 17AAG (0, 5, 50, 200 nM) for 16 h, followed by 96 h incubation with various lapatinib and 17AAG combinations. Also, pre-incubation with 17AAG followed by 17AAG and lapatinib combinations was performed with the same concentrations. Thereafter, 3-[4,5-dimethylthiazol-2-yl]-2,5-diphenyltetrazolium bromide (MTT) in PBS was added and incubated for 3 h 45 min at 37 ^{0}C. Subsequently, plates were centrifuged and supernatant was carefully aspirated. After dissolving formazan crystals in DMSO, extinction was measured at 520 nm using Biorad Microplate Benchmark reader. Cell survival was calculated as extinction ratio of treated to untreated cells, and was expressed as percentage.

Fragmentation, conjugation, ^{89}Zr-labeling and quality control of ^{89}Zr-trastuzumab-F(ab')$_2$

Trastuzumab (Herceptin; Roche) was digested and purified to F(ab')$_2$ fragments using immobilized pepsin (Thermo Scientific). Trastuzumab-F(ab')$_2$ conjugation and ^{89}Zr labeling was performed as described by Verel et al.[22] Briefly, trastuzumab-F(ab')$_2$ was first conjugated with the chelator N-succinyldesferrioxamine-B-tetrafluorphenol (N-sucDf-TFP; kindly provided by GAMS van Dongen at VUMC, Amsterdam) in 5-fold molar excess. After conjugation, the product was purified by ultracentrifugation using a 30 kDa Vivaspin-2 filter (Sartorius) and stored in water for injection at -20 ^{0}C. In the second step, N-sucDf-trastuzumab-F(ab')$_2$ was freshly radiolabeled with ^{89}Zr-

oxalate (IBA Molecular) on the day of use. N-sucDf-trastuzumab-F(ab')$_2$ and ^{89}Zr-trastuzumab-F(ab')$_2$ were analyzed for conjugation ratios, aggregation and (radiochemical) purity by size exclusion high performance liquid chromatography (SE-HPLC). Trastuzumab was fully digested to F(ab')$_2$ fragments, as indicated by a delay in retention time from 19.6 min for full length trastuzumab to 20.7 min for trastuzumab-F(ab')$_2$ (supplementary Fig. 1A, upper panel). A second peak with a retention time of 23.9 min revealed the presence of some IgG remnants with a size of ~20 kD. N-sucDf-trastuzumab-F(ab')$_2$ was labeled with ^{89}Zr in a specific activity of 250 MBq/mg with a radiochemical purity >95%. Stability testing of ^{89}Zr-trastuzumab-F(ab')$_2$ in 0.9% NaCl at 4 ^{0}C and in human serum at 37 ^{0}C revealed a ^{89}Zr release of 0.60 ± 0.35 and 4.4 ± 0.84% per 24 h, respectively (supplementary Fig. 1B). The immunoreactivity of ^{89}Zr-trastuzumab-F(ab')$_2$ was determined using SKBR3 in a Lindmo assay[23] and was calculated at 93 ± 4% (supplementary Fig. 1C and 1D).

^{89}Zr-trastuzumab-F(ab')$_2$ cell binding and internalization assay

Attached SKBR3 cells were incubated with 300 nM lapatinib for 24 h. Cells were harvested with trypsin, counted and resuspended in their culture media in a concentration of $1{\cdot}10^6$ cells per mL. Subsequently, samples of $1.5{\cdot}10^6$ SKBR3 cells were incubated in duplicate at 37 ^{0}C with 0.0667 µg ^{89}Zr-trastuzumab-F(ab')$_2$ for 2 h. After removal of the medium, internalized and membrane bound ^{89}Zr-trastuzumab-F(ab')$_2$ were separated by 10 min incubation with 0.2 M glycine + 4 M urea buffer (pH 2). Unbound, membrane bound and internalized ^{89}Zr-trastuzumab-F(ab')$_2$ was counted in a calibrated well-type gamma-counter.

Animal studies

In vivo imaging and biodistribution experiments were conducted using male athymic mice (BALB/cOlaHsd nude; Harlan), with n = 5-6 per group and isofluran inhalation anesthesia (induction 3%, maintenance 1.5%). All experiments were approved by the animal experiments committee of the University of Groningen.

At 8 weeks of age mice were injected subcutaneously with $5{\cdot}10^6$ SKBR3 cells mixed 1:1 with Matrigel™ (BD Bioscience) to a total volume of 300 µL. Tumor growth was measured two times weekly with caliper measurement. When

tumors measured ~5 mm in diameter (~100 mg), approximately 3-4 weeks after inoculation, mice were injected with ^{89}Zr-trastuzumab-F(ab')$_2$ (~5 MBq, 20 μg) intravenously via the penile vein. Static PET images of 15 min acquisition time were obtained 6 and 24 h postinjection with a microPET Focus 220 rodent scanner (CTI Siemens) followed by a 8 min transmission scan. At 7 days after the first ^{89}Zr-trastuzumab-F(ab')$_2$ injection, mice were re-injected with ^{89}Zr-trastuzumab-F(ab')$_2$ and PET scans were made following the same protocol. Lapatinib was administered orally at a dose of 100 mg/kg/day starting 1 day after the first scan. 17AAG 150 mg/kg divided over 3 gifts of 50 mg/kg in 24 h (adapted from Smith-Jones et al[24]), was administered intraperitoneally (ip) one day before the second ^{89}Zr-trastuzumab-F(ab')$_2$ injection. ^{89}Zr-trastuzumab-F(ab')$_2$ was quantified in tumor, blood pool, kidney and liver using AMIDE Medical Image Data Examiner software (version 0.9.1, Stanford University).[25] Animals were sacrificed after the last scan and organs were excised, rinsed for residual blood, weighed and counted for radioactivity in a calibrated well-type gamma-counter (LKB Wallac). Tissue activity is expressed as percentage of the injected dose per gram tissue (%ID/g) and tumor to blood ratio (TBR).

Histology and immunohistochemistry

Formalin-fixed, paraffin-embedded tumors were stained with hematoxylin-eosin (H&E) for histology, and HER2 expression was immunohistochemically stained with an anti-HER2 antibody (clone CB11, Neomarker). HER2 immunohistochemistry results were scored semi quantitatively according to a 4 level system: 0, 1, 2 and 3+, which corresponds with no, weak, moderate or strong circumferential, membranous staining.

Statistical analysis

Data are presented as mean ± standard deviation (SD) from at least three individual experiments/animals. Statistical analysis was performed using the Mann-Whitney test for non-parametric data, the unpaired T-test for parametric data, the paired T-test for paired data and the Wilcoxon signed-rank test for column comparison. A P value ≤ 0.05 was considered significant.

RESULTS

In vitro effects of lapatinib and 17AAG on EGFR/HER2 expression, EGFR/HER2 signaling and cell survival

EGFR membrane expression was raised to 170 ± 69% (P = 0.034) by lapatinib, but downregulated 41 ± 19% by 17AAG (P = 0.016) (Fig. 1A). The 17AAG effect was prevented by pretreatment with lapatinib, leading to a 71% higher (P = 0.011) EGFR expression than seen with 17AAG alone. Lapatinib did not affect HER2 membrane expression. 17AAG downregulated HER2 by 76 ± 11% (P = 0.022). This downregulation was inhibited by pretreatment with lapatinib, and the resulting HER2 expression was 202% higher than for 17AAG alone (P = 0.0033) and 38% lower compared to lapatinib alone (P = 0.0011).

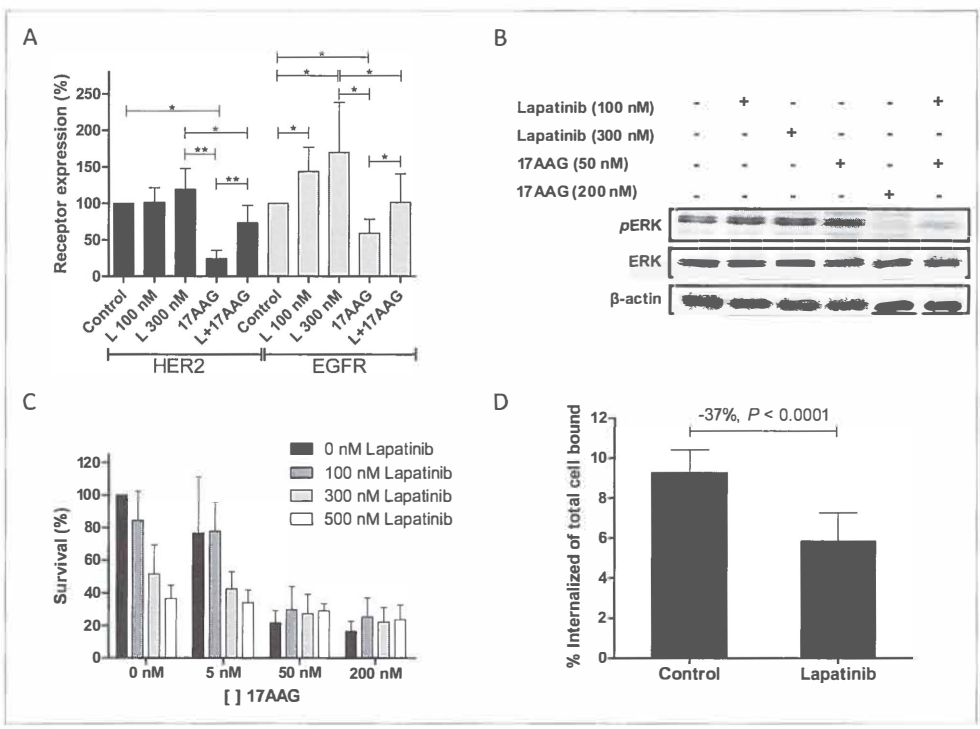

Figure 1. *In vitro* effects of lapatinib and 17AAG on SKBR3 cells. Flow cytometry analysis of HER2 and EGFR membrane expression after treatment with lapatinib (L), 17AAG or the combination. Receptor expression in untreated control cells were set at 100% (A). Representative Western blot for phosphorylated (*p*) and total ERK as readout for HER2/EGFR signaling after lapatinib and/or 17AAG treatment (B). Impact of lapatinib and/or 17AAG on cell survival as assessed by MTT assay is shown for the experiment with lapatinib pre-incubation (C). Effects of lapatinib on ^{89}Zr-trastuzumab-F(ab')$_2$ membrane binding and internalization, expressed as percentage change compared to untreated control cells (D). A P value ≤ 0.05 is indicated as *, and ** indicates a P value ≤ 0.01.

The cellular downstream effects of lapatinib and 17AAG on EGFR/HER2 signaling in SKBR3 as represented by ERK phosphorylation showed that lapatinib and 17AAG alone did not inhibit ERK phosphorylation at the tested concentrations, except for the 200 nM 17AAG dose. The combination of lapatinib and 17AAG however showed already a clear inhibition of ERK phosphorylation at the lowest concentration tested (100 nM lapatinib and 50 nM 17AAG) (Fig.1B).

Lapatinib and 17AAG did not antagonize or synergize their effects on SKBR3 survival for al tested concentrations (Fig. 1C). No difference was observed between cells pretreated with lapatinib or pretreated with 17AAG.

In vitro effects of lapatinib on ^{89}Zr-trastuzumab-F(ab')$_2$ cell binding and internalization

Lapatinib treatment resulted in a 23% (P = 0.023) higher ^{89}Zr-trastuzumab-F(ab')$_2$ binding to SKBR3 cell membranes, while ^{89}Zr-trastuzumab-F(ab')$_2$ internalization by SKBR3 was 25% (P = 0.0022) lower in lapatinib treated cells. The percentage internalized ^{89}Zr-trastuzumab-F(ab')$_2$ of all cell bound (membrane bound + internalized) ^{89}Zr-trastuzumab-F(ab')$_2$ in lapatinib treated cells was 37% (P < 0.0001) lower than control cells (Fig. 1D).

In vivo ^{89}Zr-trastuzumab-F(ab')$_2$ PET imaging and biodistribution

^{89}Zr-trastuzumab-F(ab')$_2$ reproducibility, optimal injection-to-imaging interval and ^{89}Zr-trastuzumab-F(ab')$_2$ biodistribution was evaluated in untreated mice (Fig. 2). Blood pool activity of ^{89}Zr-trastuzumab-F(ab')$_2$ declined between 6 to 24 h postinjection. Kidney uptake of ^{89}Zr-trastuzumab-F(ab')$_2$ reached its plateau at 6 h. ^{89}Zr-trastuzumab-F(ab')$_2$ levels in well perfused organs such as liver and spleen decreased from 6 to 24 h postinjection, corresponding to blood pool activity. ^{89}Zr-trastuzumab-F(ab')$_2$ tumor uptake increased non-significantly from 6 to 24 h postinjection (Fig. 2A and 2B). Therefore a 24 h interval between ^{89}Zr-trastuzumab-F(ab')$_2$ injection and PET scan acquisition was considered most suitable for HER2-imaging during treatment. Comparison of quantification of blood pool, kidney, liver and tumor uptake in the 24 h scans obtained in untreated mice after the first and second ^{89}Zr-trastuzumab-F(ab')$_2$ injection resulted in a high correlation (R^2 = 0.99) between data from both scans (Fig. 2C). *Ex vivo* analysis of ^{89}Zr-trastuzumab-F(ab')$_2$ biodistribution confirmed the PET

quantification data, with highest uptake in kidneys, liver and spleen, and low uptake in other organs (Fig. 2D). Tumor uptake of ^{89}Zr-trastuzumab-F(ab')$_2$ at 24 h postinjection was 7.4 ± 1.4%ID/g.

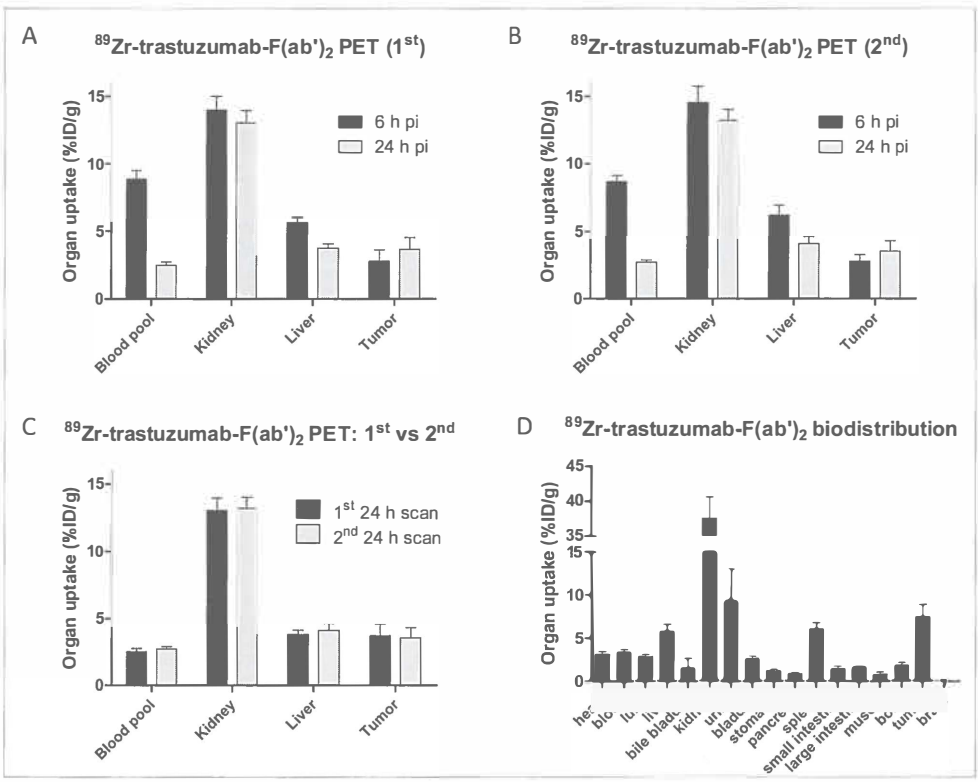

Figure 2. Feasibility and reproducibility of ^{89}Zr-trastuzumab-F(ab')$_2$ PET imaging (A-C) and biodistribution (D) in SKBR3 xenograft bearing mice. Mice were injected with ^{89}Zr-trastuzumab-F(ab')$_2$ two times, with a 7 day interval and scans were obtained 6 and 24 h postinjection (pi).

In vivo effects of lapatinib and 17AAG on ^{89}Zr-trastuzumab-F(ab')$_2$ tumor uptake

^{89}Zr-trastuzumab-F(ab')$_2$ PET images acquired before and after treatment visually showed a lower ^{89}Zr-trastuzumab-F(ab')$_2$ tumor uptake in lapatinib, 17AAG and lapatinib plus 17AAG treated mice (Fig. 3). This reduction was confirmed by PET quantification of ^{89}Zr-trastuzumab-F(ab')$_2$ tumor-to-blood ratios (TBR). Intragroup paired analysis showed a 32% TBR decrease by lapatinib (P = 0.0004), 34% decrease by 17AAG (P = 0.0022) and 53% decrease by the combination (P = 0.011). Intergoup analysis of ^{89}Zr-trastuzumab-F(ab')$_2$ TBR compared to the

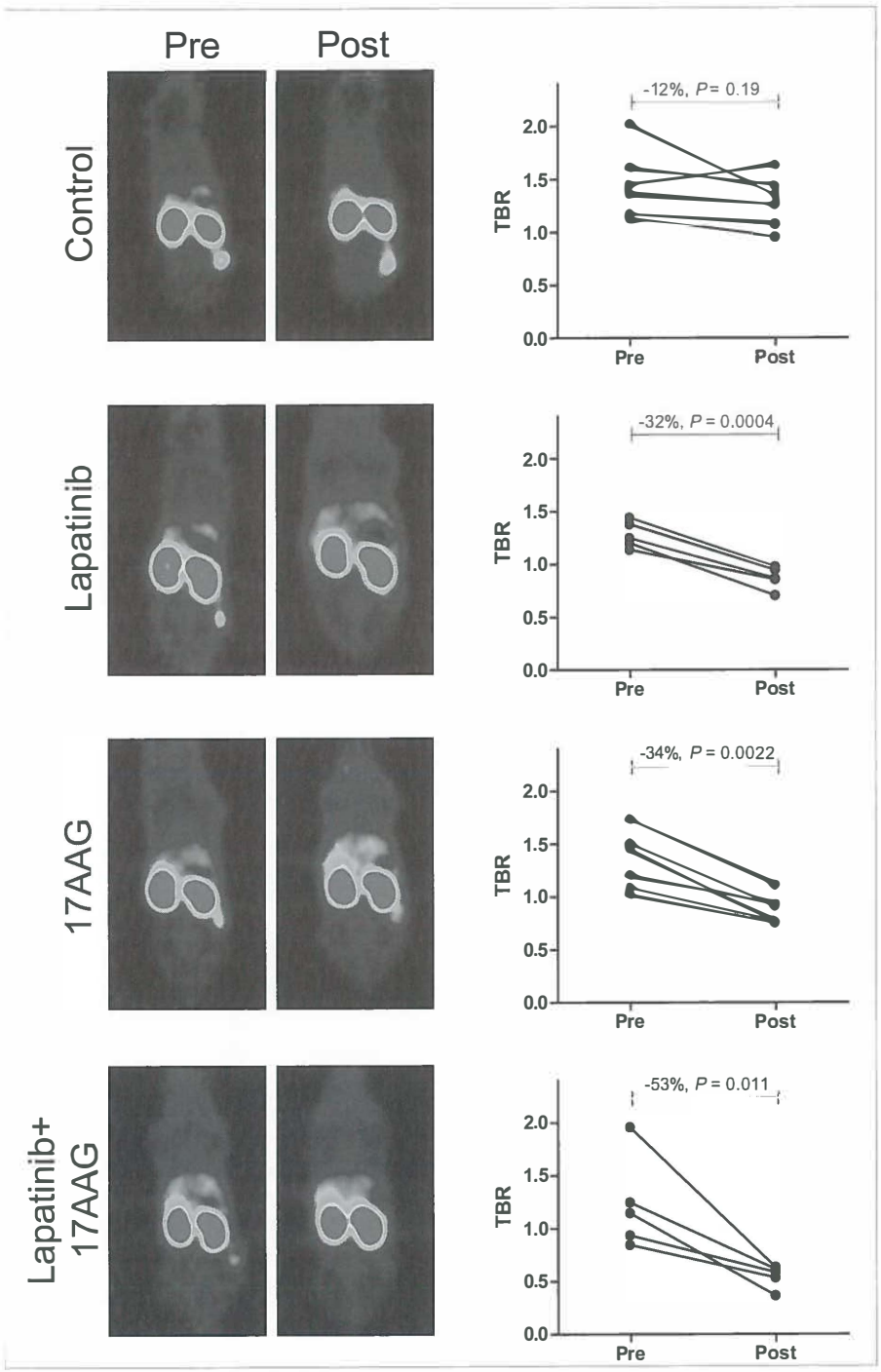

Figure 3. Representative examples of coronal ^{89}Zr-trastuzumab-F(ab')$_2$ PET images acquired pre and post treatment, and PET quantification of ^{89}Zr-trastuzumab-F(ab')$_2$ tumor-to-blood ratios (TBR) in individual mice of the different treatment groups. See page 169 for full color image.

control group showed a 32 ± 8% decline by lapatinib, 33 ± 11% decline by 17AAG and 58 ± 8% decline by the combination (Fig. 4A). *Ex vivo* biodistribution analysis showed that TBR was lower in all treatment groups compared to the control group, and that TBR in mice treated with the combination was 40% lower compared to lapatinib alone (P = 0.0087) or 34% lower compared to 17AAG (P = 0.026) alone (Fig. 4B). ^{89}Zr-trastuzumab-F(ab')$_2$ TBR as quantified from the *ex vivo* biodistribution data and *in vivo* PET data showed a good correlation with R^2 = 0.88 (Fig. 4C).

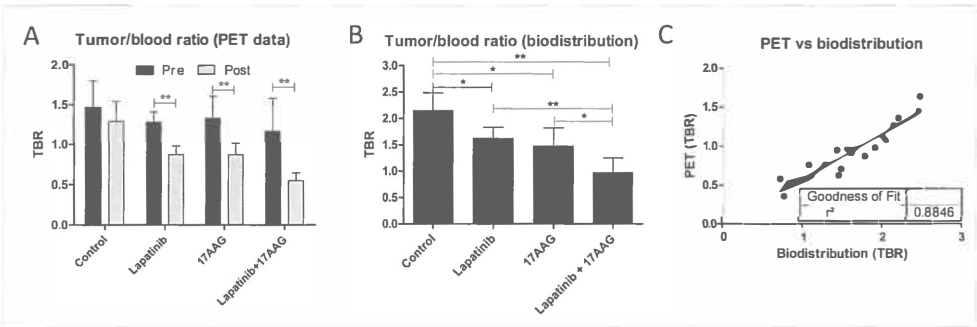

Figure 4: Comparison of TBR as quantified in the PET scans (A) and from the ex vivo biodistribution data (B). Correlation plot of ^{89}Zr-trastuzumab-F(ab')$_2$ TBR as quantified from the ex vivo biodistribution data and in vivo PET data (C). A P value ≤ 0.05 is indicated as *, and ** indicates a P value ≤ 0.01.

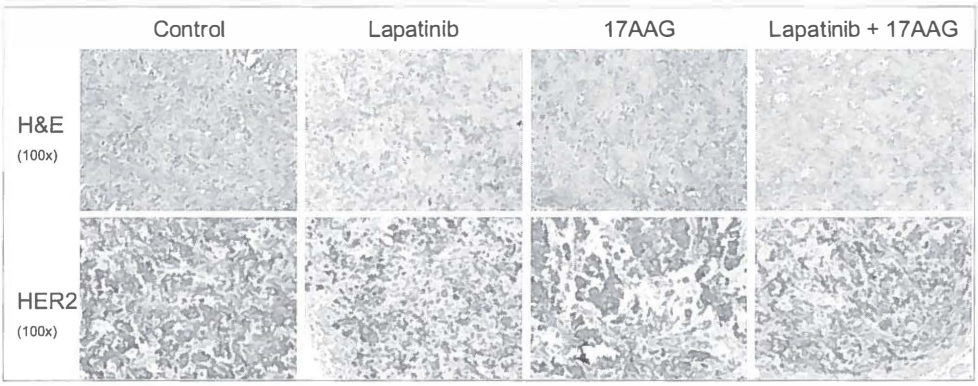

Figure 5. Representative examples of staining for hematoxylin-eosin (H&E) and HER2 in tumors from untreated mice and mice treated with lapatinib, 17AAG or lapatinib + 17AAG. See page 170 for full color image.

Histology and immunohistochemistry

H&E staining showed no difference in morphology between tumors from control and lapatinib, 17AAG or combined treated mice (Fig. 6). All tumors contained viable tumor and stromal cells, and areas of necrosis. Only in tumors from mice treated with lapatinib and 17AAG combination, some apoptotic cells could be identified. HER2 staining indicated no difference in cellular HER2 levels between tumors from control and treated mice.

DISCUSSION

This study shows that ^{89}Zr-trastuzumab-F(ab')$_2$ tumor uptake is reduced by lapatinib and 17AAG. In case of lapatinib this is the consequence of inhibited internalization of ^{89}Zr-trastuzumab-F(ab')$_2$ upon HER2 binding, while for 17AAG this is the result of lower HER2 expression at the cell membrane. The combination of lapatinib and 17AAG resulted in the strongest reduction of ^{89}Zr-trastuzumab-F(ab')$_2$ tumor uptake.

We used the F(ab)$_2$ fragment of trastuzumab instead of the full length antibody. The advantage of this approach is that it allows a shorter interval between tracer injection and imaging. This permits to study the rapid dynamic HER2 responses to lapatinib and 17AAG. The organ distribution with ^{89}Zr-trastuzumab-F(ab')$_2$ shows what was to be expected for a radiolabeled fragment of trastuzumab, namely rapid blood clearance and high kidney uptake.[24;26;27]

Our previous *in vitro* experiments with ^{111}In-trastuzumab showed that 50% of the membrane bound ^{111}In-trastuzumab was internalized within 4 h after binding to HER2 overexpressing SKOV3 cells.[28] Profound internalization of radiolabeled trastuzumab, is likely one of the reasons why optimal tumor-to-background ratios with radiolabeled trastuzumab are found 4-5 days post tracer injection.[21;29] During the interval between tracer injection and image acquisition, radiolabeled trastuzumab will continuously bind to HER2 expressed at the tumor cell membrane, subsequently followed by rapid internalization, resulting in tumor accumulation of the tracer (see also Fig. 6). The final uptake of (fragments of) trastuzumab in tumors as seen on the nuclear scans reflects both the membrane bound and internalized trastuzumab. This emphasizes the value of using a residualizing isotope (like the radiometals ^{111}In and ^{89}Zr) for imaging with ligands that are internalized upon target binding. Antibody based tracers targeted at

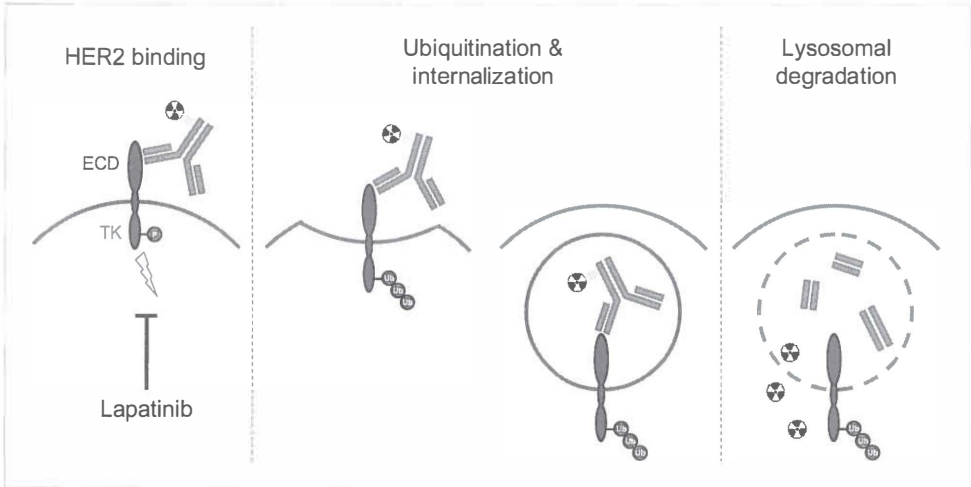

Figure 6. Proposed mechanism of tyrosine kinase triggered HER2 internalization and intracellular uptake of HER2 targeted antibody based imaging tracers and drugs. The HER2 internalization cascade is initiated by phosphorylation of the tyrosine kinase domain. Next step is ubiquitination of the HER2 intracellular domain, followed by internalization of the HER2-antibody complex in a lysosome. Within the lysosome, the HER2 bound antibody based imaging tracer (or drug) is degraded with subsequent intracellular release of the radioisotope (for radioactive tracers), the fluorescent dye (for optical tracers) or the toxin (for antibody-drug conjugates). Most of the internalized HER2 is recycled back to the tumor cell membrane. Lapatinib inhibits HER2 phosphorylation and thereby prevents the first step of the cascade, possibly resulting in hampered intracellular uptake of HER2 targeted antibody based imaging tracers and drugs. See page 170 for full color image.

membrane bound receptors with a high intrinsic turnover likely are the ligands most susceptible for internalization.

HER2 expression, dynamics and internalization are presumably of great clinical relevance for HER2 targeted therapies. The mechanisms responsible for HER2 internalization and subsequent endosomal processing have not yet been exactly uncovered. In contrast to the efficient and well described continuous endocytic degradation of EGFR, the endocytic degradation of HER2 is impaired.[30;31] One of the proposed mechanisms responsible for this is the rapid and efficient recycling of internalized HER2 back to the cell membrane, resulting in a dynamic equilibrium between HER2 endocytosis and recycling.[32] HER2 internalization is triggered by tyrosine kinase activity of the intracellular domain of the receptor[33] which can be blocked by lapatinib. This is the proposed mechanism by which lapatinib upregulates HER2 expression at the cell membrane.[18] Lapatinib induced HER2 membranous upregulation is an attractive strategy for potentiating agents that bind to the extracellular domain of HER2. Although not necessarily the

consequence of only this mechanism, combining lapatinib with trastuzumab has already shown to be more effective than lapatinib or trastuzumab alone in the metastatic and neoadjuvant setting.[10;11] These promising results with the trastuzumab and lapatinib combination, together with the recent successes obtained with single agent trastuzumab-DM1,[34] have raised interest to study the effect of trastuzumab-DM1 combined with a HER2 tyrosine kinase inhibitor.[35] In a preclinical study with MMTV-HER2 Fo5 mammary tumor transplants, combining trastuzumab-DM1 with lapatinib showed an additional effect on tumor growth inhibition.[36] However, since the antitumor effect of trastuzumab-DM1 relies on the internalization and intracellular release of DM1,[37;38] the effect of HER2 tyrosine kinase inhibitors on trastuzumab-DM1 tumor uptake, should also be investigated in preclinical studies.

We found *in vitro* an additive effect of lapatinib and 17AAG on inhibition of HER2 signaling, and *in vivo* lapatinib and 17AAG both reduced ^{89}Zr-trastuzumab-F(ab')$_2$ tumor uptake. This effect was even more pronounced in mice receiving the combination of lapatinib and 17AAG. The combination of lapatinib and HSP90 inhibition using the 17AAG analogue IPI-504 has already shown to be superior to either single agent with complete regressions of some tumors in KPL4 human breast cancer xenografts.[39] Combined inhibition of HSP90 and the tyrosine kinase domain of HER2 therefore warrants further investigation in HER2 positive tumors.

In conclusion, lapatinib inhibits HER2 internalization, and thereby decreases ^{89}Zr-trastuzumab-F(ab')$_2$ tumor uptake. HSP90 inhibition with 17AAG lowers HER2 membrane expression and thereby ^{89}Zr-trastuzumab-F(ab')$_2$ tumor uptake. This study shows that tumor uptake of HER2 imaging tracers depends not only on HER2 expression, but also on HER2 dynamics. HER2-PET imaging could therefore be useful in rationalizing HER2 targeted combinations.

Acknowledgments

The authors would like to thank Matthijs van der Kraats, Mareike Richter, Martin Pool and Frank-Jan Warnders for their technical assistance. The research was supported by grant 2007-3739 of the Dutch Cancer Society.

References

1. Moasser MM. The oncogene HER2: its signaling and transforming functions and its role in human cancer pathogenesis. Oncogene 2007;26:6469-87.
2. Hayes DF, Thor AD, Dressler LG, et al. HER2 and response to paclitaxel in node-positive breast cancer. N Engl J Med 2007;357:1496-506.
3. Baselga J, Swain SM. Novel anticancer targets: revisiting ERBB2 and discovering ERBB3. Nat Rev Cancer 2009;9:463-75.
4. Slamon DJ, Clark GM, Wong SG, Levin WJ, Ullrich A, McGuire WL. Human breast cancer: correlation of relapse and survival with amplification of the HER-2/neu oncogene. Science 1987;235:177-82.
5. Dahabreh IJ, Linardou H, Siannis F, Fountzilas G, Murray S. Trastuzumab in the adjuvant treatment of early-stage breast cancer: a systematic review and meta-analysis of randomized controlled trials. Oncologist 2008;13:620-30.
6. Dawood S, Broglio K, Buzdar AU, Hortobagyi GN, Giordano SH. Prognosis of women with metastatic breast cancer by HER2 status and trastuzumab treatment: an institutional-based review. J Clin Oncol 2010;28:92-8.
7. www.accessdata.fda.gov/drugsatfda_docs/label/2010/103792s5250lbl.pdf; accessed April 2011.
8. Spector NL, Blackwell KL. Understanding the mechanisms behind trastuzumab therapy for human epidermal growth factor receptor 2-positive breast cancer. J Clin Oncol 2009;27:5838-47.
9. Tagliabue E, Balsari A, Campiglio M, Pupa SM. HER2 as a target for breast cancer therapy. Expert Opin Biol Ther 2010;10:711-24.
10. O'Shaughnessy J, Blackwell KL, Burstein H, et al. A randomized study of lapatinib alone or in combination with trastuzumab in heavily pretreated HER2+ metastatic breast cancer progressing on trastuzumab therapy. J Clin Oncol 2010;26:abstr 1015.
11. Baselga J, Bradbury I, Eidtmann H, et al. First results of the NeoALTTO Trial (BIG 01-06 / EGF 106903): A phase III, randomized, open label, neoadjuvant study of lapatinib, trastuzumab, and their combination plus paclitaxel in women with HER2-positive primary breast cancer. 33rd Annual CTRC-AACR San Antonio Breast Cancer Symposium 2010:abstr S3-3.
12. Eccles SA, Massey A, Raynaud FI, et al. NVP-AUY922: a novel heat shock protein 90 inhibitor active against xenograft tumor growth, angiogenesis, and metastasis. Cancer Res 2008;68:2850-60.

13. Jensen MR, Schoepfer J, Radimerski T, et al. NVP-AUY922: a small molecule HSP90 inhibitor with potent antitumor activity in preclinical breast cancer models. Breast Cancer Res 2008;10:R33.
14. Solit DB, Zheng FF, Drobnjak M, et al. 17-Allylamino-17-demethoxygeldanamycin induces the degradation of androgen receptor and HER-2/neu and inhibits the growth of prostate cancer xenografts. Clin Cancer Res 2002;8:986-93.
15. Zsebik B, Citri A, Isola J, Yarden Y, Szollosi J, Vereb G. Hsp90 inhibitor 17-AAG reduces ErbB2 levels and inhibits proliferation of the trastuzumab resistant breast tumor cell line JIMT-1. Immunol Lett 2006;104:146-55.
16. Oude Munnink TH, Korte MA, Nagengast WB, et al. (89)Zr-trastuzumab PET visualises HER2 downregulation by the HSP90 inhibitor NVP-AUY922 in a human tumour xenograft. Eur J Cancer 2010;46:678-84.
17. Modi S, Stopeck AT, Gordon MS, et al. Combination of trastuzumab and tanespimycin (17-AAG, KOS-953) is safe and active in trastuzumab-refractory HER-2 overexpressing breast cancer: a phase I dose-escalation study. J Clin Oncol 2007;25:5410-7.
18. Scaltriti M, Verma C, Guzman M, et al. Lapatinib, a HER2 tyrosine kinase inhibitor, induces stabilization and accumulation of HER2 and potentiates trastuzumab-dependent cell cytotoxicity. Oncogene 2009;28:803-14.
19. Vazquez-Martin A, Oliveras-Ferraros C, Cufí S, Barco SD, Martin-Castillo B, Menendez JA. Lapatinib, a dual HER1/HER2 tyrosine kinase inhibitor, augments basal cleavage of HER2 extracellular domain (ECD) to inhibit HER2-driven cancer cell growth. J Cell Physiol. 2011; 226:52-7.
20. Dijkers ECF, Kosterink JG, Rademaker AP, et al. Development and characterization of clinical-grade ^{89}Zr-trastuzumab for HER2/*neu* immunoPET imaging. J Nucl Med 2009;50:962-9.
21. Dijkers EC, Oude Munnink TH, Kosterink JG, et al. Biodistribution of (89)Zr-trastuzumab and PET imaging of HER2-positive lesions in patients with metastatic breast cancer. Clin Pharmacol Ther 2010;87:586-92.
22. Verel I, Visser GW, Boellaard R, Stigter-van WM, Snow GB, van Dongen GA. 89Zr immuno-PET: comprehensive procedures for the production of 89Zr-labeled monoclonal antibodies. J Nucl Med 2003;44:1271-81.
23. Lindmo T, Boven E, Cuttitta F, Fedorko J, Bunn PA, Jr. Determination of the immunoreactive fraction of radiolabeled monoclonal antibodies by linear extrapolation to binding at infinite antigen excess. J Immunol Methods 1984;72:77-89.

24. Smith-Jones PM, Solit DB, Akhurst T, Afroze F, Rosen N, Larson SM. Imaging the pharmacodynamics of HER2 degradation in response to Hsp90 inhibitors. Nat Biotechnol 2004;22:701-6.
25. Loening AM, Gambhir SS. AMIDE: a free software tool for multimodality medical image analysis. Mol Imaging 2003;2:131-7.
26. Tang Y, Scollard D, Chen P, Wang J, Holloway C, Reilly RM. Imaging of HER2/neu expression in BT-474 human breast cancer xenografts in athymic mice using [(99m)Tc]-HYNIC-trastuzumab (Herceptin) Fab fragments. Nucl Med Commun 2005;26:427-32.
27. Tang Y, Wang J, Scollard DA, et al. Imaging of HER2/neu-positive BT-474 human breast cancer xenografts in athymic mice using (111)In-trastuzumab (Herceptin) Fab fragments. Nucl Med Biol 2005;32:51-8.
28. Lub-de Hooge MN, Kosterink JG, Perik PJ, et al. Preclinical characterisation of 111In-DTPA-trastuzumab. Br J Pharmacol 2004;143:99-106.
29. Perik PJ, Lub-de Hooge MN, Gietema JA, et al. Indium-111-labeled trastuzumab scintigraphy in patients with human epidermal growth factor receptor 2-positive metastatic breast cancer. J Clin Oncol 2006;24:2276-82.
30. Sorkin A, Goh LK. Endocytosis and intracellular trafficking of ErbBs. Exp Cell Res 2008;314:3093-106.
31. Roepstorff K, Grovdal L, Grandal M, Lerdrup M, van Deurs B. Endocytic downregulation of ErbB receptors: mechanisms and relevance in cancer. Histochem Cell Biol 2008;129:563-78.
32. Austin CD, De Mazière AM, Pisacane PI, et al. Endocytosis and sorting of ErbB2 and the site of action of cancer therapeutics trastuzumab and geldanamycin. Mol Biol Cell. 2004;15:5268-82.
33. Gilboa L, Ben Levy R, Yarden Y, Henis YI. Roles for a cytoplasmic tyrosine and tyrosine kinase activity in the interactions of Neu receptors with coated pits. J Biol Chem 1995;270:7061-7.
34. Burris HA 3rd, Rugo HS, Vukelja SJ, et al. Phase II study of the antibody drug conjugate trastuzumab-DM1 for the treatment of human epidermal growth factor receptor 2 (HER2)-positive breast cancer after prior HER2-directed therapy. J Clin Oncol. 2011; 29:398-405.
35. Isakoff SJ, Baselga J. Trastuzumab-DM1: Building a chemotherapy-free road in the treatment of human epidermal growth factor receptor 2-positive breast cancer. J Clin Oncol. 2011; 29:351-4.
36. Lewis Phillips GD, Fields C, Crocker L et al. Potent anti-tumor activity of trastuzumab-DM1 antibody-drug conjugate in combination with cytotoxic chemotherapeutic agents, antibodies or small molecule kinase inhibitors. 99th AACR Annual Meeting: abstract #2133.

37. Krop IE, Beeram M, Modi S, et al. Phase I study of trastuzumab-DM1, an HER2 antibody-drug conjugate, given every 3 weeks to patients with HER2-positive metastatic breast cancer. J Clin Oncol 2010;28:2698-704.
38. Lewis Phillips GD, Li G, Dugger DL, et al. Targeting HER2-positive breast cancer with trastuzumab-DM1, an antibody-cytotoxic drug conjugate. Cancer Res 2008;68:9280-90.
39. Leow CC, Chesebrough J, Coffman KT, et al. Antitumor efficacy of IPI-504, a selective heat shock protein 90 inhibitor against human epidermal growth factor receptor 2-positive human xenograft models as a single agent and in combination with trastuzumab or lapatinib. Mol Cancer Ther 2009;8:2131-41.

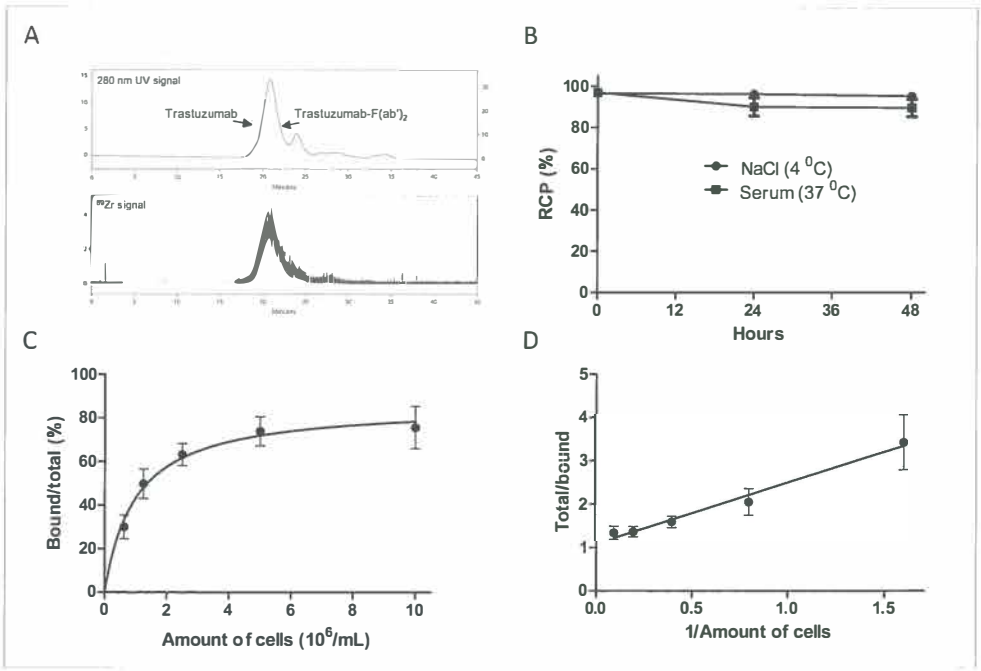

Supplementary figure 1. Quality control of ^{89}Zr-trastuzumab-F(ab')$_2$. Panel A shows a typical SE-HPLC chromatogram of ^{89}Zr-trastuzumab-F(ab')$_2$ with detection at 280 nm for the protein signal (upper panel) and co-registration of radioactive ^{89}Zr signal (lower panel). A SE-HPLC chromatogram of full length trastuzumab is shown for reference. Panel B shows the stability of ^{89}Zr-trastuzumab-F(ab')$_2$ in 0.9% NaCl at 4 ^{0}C and in human serum at 37 ^{0}C expressed as radiochemical purity (RCP) during 48 h. Binding of ^{89}Zr-trastuzumab-F(ab')$_2$ to increasing amounts of SKBR3 cells (C) and the reciprocal plot of ^{89}Zr-trastuzumab-F(ab')$_2$ binding to calculate the binding to infinite antigen excess to determine immunoreactivity (D).

Chapter 6A:

Biodistribution of ^{89}Zr-trastuzumab and PET imaging of HER2-positive lesions in patients with metastatic breast cancer

Eli Dijkers[1,2]
Thijs Oude Munnink[3]
Jos Kosterink[1]
Adrienne Brouwers[2]
Piet Jager[2]
Johan de Jong[2]
Guus van Dongen[4]
Carolina Schröder[3]
Marjolijn Lub-de Hooge[1,2]
Elisabeth de Vries[3]

Departments of Hospital and Clinical Pharmacy[1], Nuclear Medicine and Molecular Imaging[2], and Medical Oncology[3], University Medical Center Groningen, Groningen, The Netherlands; Department of Nuclear Medicine and PET Research[4],VU University Medical Center, Amsterdam, The Netherlands

Clinical Pharmacology and Therapeutics 2010;87:586–92

ABSTRACT

We performed a feasibility study to determine the optimal dosage and time of administration of the monoclonal antibody zirconium-89 (^{89}Zr)-trastuzumab to enable positron emission tomography (PET) imaging of human epidermal growth factor receptor-2 (HER2)-positive lesions. Fourteen patients with HER2-positive metastatic breast cancer received 37 MBq of ^{89}Zr-trastuzumab at one of three doses (10 or 50 mg for those who were trastuzumab-naive and 10 mg for those who were already on trastuzumab treatment). The patients underwent at least two PET scans between days 2 and 5. The results of the study showed that the best time for assessment of ^{89}Zr-trastuzumab uptake by tumors was 4–5 days after the injection. For optimal PET-scan results, trastuzumab-naive patients required a 50 mg dose of ^{89}Zr-trastuzumab, and patients already on trastuzumab treatment required a 10 mg dose. The accumulation of ^{89}Zr-trastuzumab in lesions allowed PET imaging of most of the known lesions and some that had been undetected earlier. The relative uptake values (mean ± SD) were 12.8 ± 5.8, 4.1 ± 1.6, and 3.5 ± 4.2 in liver, bone, and brain lesions, respectively, and 5.9 ± 2.4, 2.8 ± 0.7, 4.0 ± 0.7, and 0.20 ± 0.1 in normal liver, spleen, kidneys, and brain tissue, respectively. PET scanning after administration of ^{89}Zr-trastuzumab at appropriate doses allows visualization and quantification of uptake in HER2-positive lesions in patients with metastatic breast cancer.

INTRODUCTION

Human epidermal growth factor receptor-2 (HER2) is involved in cell survival, cell proliferation, cell maturation, metastasis, and angiogenesis, as well as exerting antiapoptotic effects.[1] Targeting of HER2 with the monoclonal antibody trastuzumab (Herceptin) is a well-established therapeutic strategy in the metastasized and adjuvant setting, and it has positively affected the prognosis of patients with breast cancer characterized by HER2 protein overexpression and/or amplification.[2,3]

HER2 status is routinely determined using immunohistochemistry or fluorescence *in situ* hybridization at the time of diagnosis of the primary tumor. However, there are data indicating that the HER2 status of a tumor can vary during the course of the disease.[4] In addition, there can be a discordance in HER2 expression across tumor lesions in the same patient.[5-7] Therefore, clinical guidelines encourage the use of repeated biopsies during the course of the disease.[8,9] Physicians and patients are nevertheless frequently reluctant to use this invasive technique; in addition, technical problems can arise when lesions are poorly accessible.[10]

Noninvasive HER2 imaging using single-photon emission computed tomography (SPECT) and positron emission tomography (PET) could be a strategy to determine HER2 expression and localization of HER2-overexpressing tumor lesions, including inaccessible distant metastases. This strategy, which could potentially guide HER2-targeted therapies, led to the development of ^{111}In-trastuzumab. Using this SPECT tracer, we have shown HER2-specific uptake in patients with HER2-positive metastatic breast cancer. ^{111}In-trastuzumab imaging discovered new HER2-positive lesions in 13 of 15 patients and was therefore considered to be of potential value as a clinical diagnostic tool in metastatic disease.[11] It was only after our ^{111}In-trastuzumab clinical study was completed that the long-lived PET isotope zirconium-89 (^{89}Zr) became available for clinical immunoPET imaging with ^{89}Zr-labeled antibodies.[12] For immunoPET imaging, positron-emitting radiometals such as ^{89}Zr have an advantage over radiohalogens such as ^{124}I because they are residualizing and are therefore retained within the target cell after internalization and intracellular degradation of the tracer. This results in higher uptake in the tumor when an internalized antibody such as trastuzumab is used.[7] Of the positron-emitting radiometals, ^{89}Zr has the longest and therefore most favorable half-life (78.4 h), allowing antibody imaging up to 7 days after the injection. Preclinical evaluation of ^{89}Zr-trastuzumab showed that it

displays superior image quality as compared to ^{111}In-trastuzumab, given the high spatial resolution and sensitivity of PET, although the uptake levels of ^{89}Zr-trastuzumab and ^{111}In-trastuzumab in the tumors were equivalent.[13] In addition, PET imaging has the advantage of allowing straightforward data quantification and whole-body 3D imaging. In view of these advantages, we performed this clinical study using ^{89}Zr-trastuzumab PET.

In this clinical study, we evaluated the optimal conditions for the administration of ^{89}Zr-trastuzumab to enable PET visualization and quantification of HER2-positive lesions in patients with HER2-positive metastatic breast cancer. We did this by comparing three relevant doses at early and late imaging times.

METHODS

Patients

In this prospective imaging feasibility study in female patients with metastatic breast cancer, the eligibility criteria were (i) proven HER2-positive tumor at diagnosis (as confirmed by immunohistochemistry or fluorescence in situ hybridization), (ii) at least one tumor lesion in situ at the time of inclusion, and (iii) age ≥18 years. Available standard staging procedures with conventional imaging such as radiography, CT, MRI, and bone scans were used for comparison. No standard CT or MRI scans of the brain were performed, except when there were neurological symptoms or suspicion of brain metastases, or where ^{89}Zr-trastuzumab uptake in the brain was seen on the PET scan. Exclusion criteria were (i) pregnancy, (ii) uncontrolled concurrent illness, and (iii) treatment with antibodies other than trastuzumab.

The study was approved by the medical ethical committee of the University Medical Center Groningen, and written informed consent was obtained from all patients.

Tracer and protein dose

Clinical grade ^{89}Zr-trastuzumab was produced as described previously.[13] In short, reconstituted trastuzumab (Roche, Woerden, The Netherlands) was conjugated with tetrafluorophenol-N-succinyldesferal-Fe (VU University Medical Center, Amsterdam, The Netherlands), purified, and stored at −80 °C. Good

manufacturing practice-produced ^{89}Zr-oxalate (IBA Molecular Benelux, Louvain-La-Neuve, Belgium) was used for radiolabeling the conjugate. Quality control was performed to ensure (radio)chemical purity (>95%), antigen-binding capacity (>80%), and stability.

Patients received 37 MBq (1 mCi) ^{89}Zr-trastuzumab intravenously and were monitored for 30 min after the injection to detect any infusion-related anaphylactic reactions or adverse events.

To determine the minimal required trastuzumab dose, three cohorts of ^{89}Zr-trastuzumab protein dose were used: 10 mg (cohort 1) and 50 mg (cohort 2) in those who were trastuzumab-naive and 10 mg (cohort 3) for those already on trastuzumab treatment. Each of these doses consisted of ^{89}Zr-trastuzumab (~1.5 mg), replenished with nonradioactive trastuzumab. Patients on trastuzumab treatment had been receiving up to 6 mg/kg and therefore might already have had a significant amount of trastuzumab in their systems at the time of tracer injection (calculated trastuzumab dose range was 130–675 mg).

We aimed to recruit a maximum of five to seven patients per cohort. Each cohort was evaluated after data from two patients became available. If this evaluation indicated that the trastuzumab dose was insufficient for adequate imaging, the cohort was closed.

PET imaging, biodistribution, and quantification

Each patient underwent at least one PET scan at an early time (1–3 days after injection) and one at a later time (4–7 days after injection). Images were obtained using a Siemens Exact HR+ PET camera (Siemens AG, Munich, Germany). Acquisition was carried out in 3D mode from upper thigh to head, in seven or eight bed positions with 9–12 min of imaging (including 20–22% transmission time) per bed position. PET images were reconstructed using the ordered-subsets expectation maximization algorithm, with two iterations and eight subsets.

The biodistribution of (radiolabeled) antibodies is slow ($T_{½}$ of days). It was therefore expected that the biodistribution during the timeframe of the PET scan would not be a relevant factor. A single frame was acquired to obtain maximal counting statistics and the best image quality.

The PET scans were visually examined, and ^{89}Zr-trastuzumab distribution was assessed in accordance with the protocol for blood pool, liver, spleen, kidneys, bone marrow, and intestines. The number of metastases was determined.

Quantification of ^{89}Zr-trastuzumab distribution was performed using AMIDE software (version 0.9.1; Stanford University, Palo Alto, CA).[14] Instead of the frequently used standardized uptake value, we used a modified parameter, relative uptake value (RUV), to provide a semiquantitative representation of the tissue-to-background ratio. RUV is related to the amount of tracer present in the body at the moment of scan acquisition, whereas standardized uptake value is related to the amount of tracer injected. RUV is independent of the rate of excretion of the ^{89}Zr-trastuzumab tracer and can therefore be used to quantify uptake for a period of days after the injection. For calculating RUV, we used the whole-body mean uptake (WB_{mean}) value based on the radioactivity within the field of view (rather than on the radioactivity within the region of interest, which is used in arriving at standardized uptake value). The RUV_{mean} was calculated as the ratio of mean tissue uptake to mean whole-body uptake for each scan:

$$RUV_{mean} = \frac{Tissue_{mean,\,scanX}}{WB_{mean,\,scanX}} = \frac{Tissue_{mean,\,scanX}}{A_{WB,\,scanX} / V_{WB,\,scanX}}$$

The mean tissue uptake ($Tissue_{mean}$) was determined by manually drawing a volume of interest in metastatic lesions and in normal tissues (heart, liver, spleen, kidneys, bone, and brain) and measuring the mean radioactivity in the volume of interest for all tumor lesions and tissues. The WB_{mean} was calculated by dividing total radioactivity in the field of view (A_{WB}) by the volume represented within the field of view (V_{WB}). The RUV_{max} was calculated by dividing the uptake in tissues in the most intense voxel of the volume of interest by WB_{mean}. The blood pool ^{89}Zr-trastuzumab activity was calculated for the first 5 days after injection by interpolating the volume of interest RUVs of each patient's cardiac blood pool into an exponential fitting model.

Statistics

Data are presented as means ± SD. Statistical analysis was performed using the nonparametric Mann–Whitney U-test (Graphpad Prism 5; Graphpad Software, La Jolla, CA). *P* values <0.05 were considered significant.

RESULTS

Patient characteristics

Between March 2006 and December 2008, 14 patients were enrolled in the study. Patient characteristics are presented in Table 1. The patients received 38.4 ± 1.6 MBq ^{89}Zr-trastuzumab. No infusion-related reactions or adverse events were noticed during the study. Table 2 provides study details for individual patients, including the trastuzumab dose calculated for patients already on trastuzumab, the number of scans carried out and their timing, and the biodistribution of ^{89}Zr-trastuzumab and its uptake in lesions.

Table 1. Patient characteristics

Characteristic	
Number of participants	14
Participants age (years)	
Median	48
Range	32-74
Participants body weight (kg)	
Median	72
Range	47-97
^{89}Zr-trastuzumab dose (n)	
10 mg ^{89}Zr-trastuzumab	2
50 mg ^{89}Zr-trastuzumab	5
10 mg ^{89}Zr-trastuzumab + trastuzumab therapy	7

Trastuzumab dose for ^{89}Zr-trastuzumab PET imaging

The 10 mg trastuzumab dose in cohort 1 (n = 2) resulted in a relatively high uptake in the liver and a pronounced intestinal excretion of ^{89}Zr-trastuzumab. As a result, the amount of ^{89}Zr-trastuzumab in the blood pool was limited in these trastuzumab-naive patients (Fig. 1A). Probably because rapid hepatic clearance prohibited optimal uptake of ^{89}Zr-trastuzumab in the tumors, the lesions could be visualized in only one of these two patients. We concluded that 10 mg trastuzumab was not sufficient for adequate imaging in trastuzumab-naive patients, and this cohort was therefore closed.

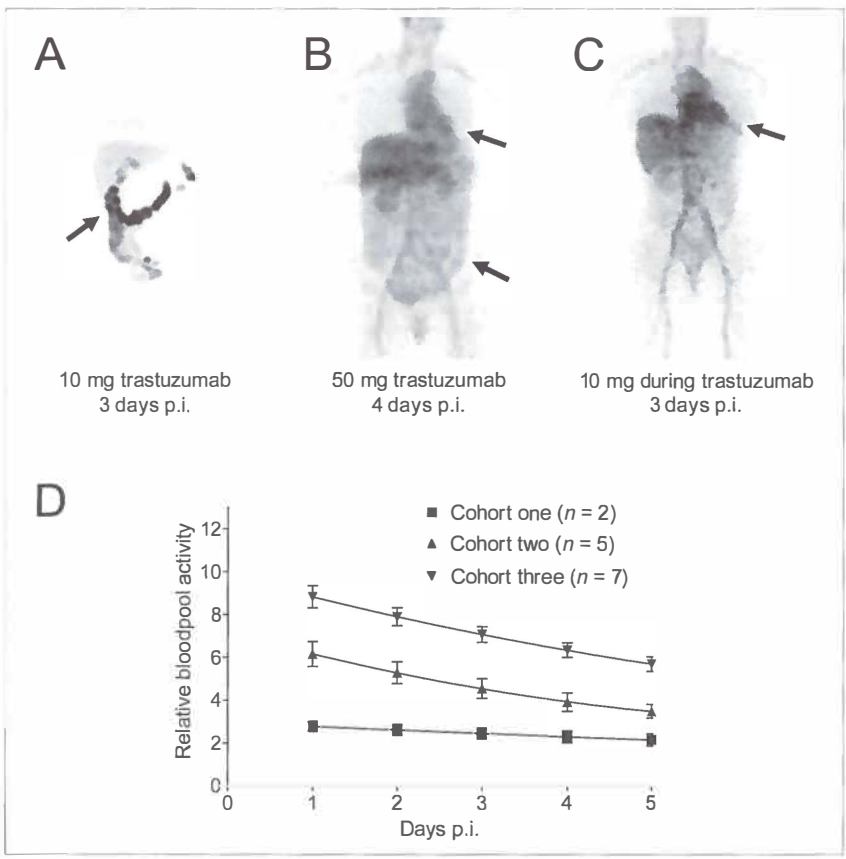

Figure 1. ^{89}Zr-trastuzumab dose dependent biodistribution and blood-clearance. Blood pool activity is indicated and intestinal excretion are indicated by arrows (A-C). The 'Relative blood pool activity' represents the amount of ^{89}Zr-trastuzumab present in the blood pool related to the total amount of ^{89}Zr-trastuzumab present during 5 days postinjection (D).

The 50 mg trastuzumab dose in cohort 2 (n = 5) resulted in less uptake in the liver and lower subsequent intestinal excretion as compared with patients in cohort 1. ^{89}Zr-trastuzumab was present in the blood pool during the scan sequence in all five patients (Fig. 1B), indicating retarded blood pool clearance. Visual analysis revealed good tumor/nontumor ratios in this cohort. Therefore, 50 mg trastuzumab was considered to have a favorable biodistribution and to be adequate for HER2-PET imaging in trastuzumab-naive patients.

In the patients in cohort 3, who were already on trastuzumab (n = 7), a 10 mg dose of trastuzumab resulted in minimal intestinal excretion and slow ^{89}Zr-trastuzumab blood clearance (Fig. 1C); 10 mg was therefore considered an adequate dose for patients already on trastuzumab therapy.

Dose-dependent blood clearance of ^{89}Zr-trastuzumab seen in the visual analysis was confirmed by quantitative analysis of ^{89}Zr-trastuzumab presence in the cardiac blood pool. Fig. 1D shows the quantitative PET analysis of the relative blood pool activity levels of ^{89}Zr-trastuzumab as fitted curves for 5 days after injection in all three cohorts. The curve is lowest for cohort 1 and shows little change during the 5-day period, indicating rapid blood pool clearance within the first 24 h. Patients in cohorts 2 and 3 show a much higher relative blood pool activity, indicating slow clearance of ^{89}Zr-trastuzumab from the blood pool.

Interval between tracer injection and PET scan

Except in the 10-mg dose group (cohort 1), extensive ^{89}Zr-trastuzumab activity was still present in the blood pool 1–2 days after the injection, even while uptake was observed in liver, spleen, and kidneys. At 4–5 days after the injection, ^{89}Zr-trastuzumab activity in the blood pool was lower, and uptake in tumors had increased. This is illustrated by means of the scans obtained from a patient already on trastuzumab treatment (Fig. 2A–C). This representative patient showed a slight decrease in blood pool tracer activity and marked ^{89}Zr-trastuzumab accumulation in the brain metastasis over time.

Scans performed at day 6 or 7 after the injection yielded decreased image quality because of insufficient counting statistics. The optimal time for the scan represents a balance between good tumor/nontumor ratios and sufficient radioactive signal. The best time for assessing uptake of ^{89}Zr-trastuzumab in

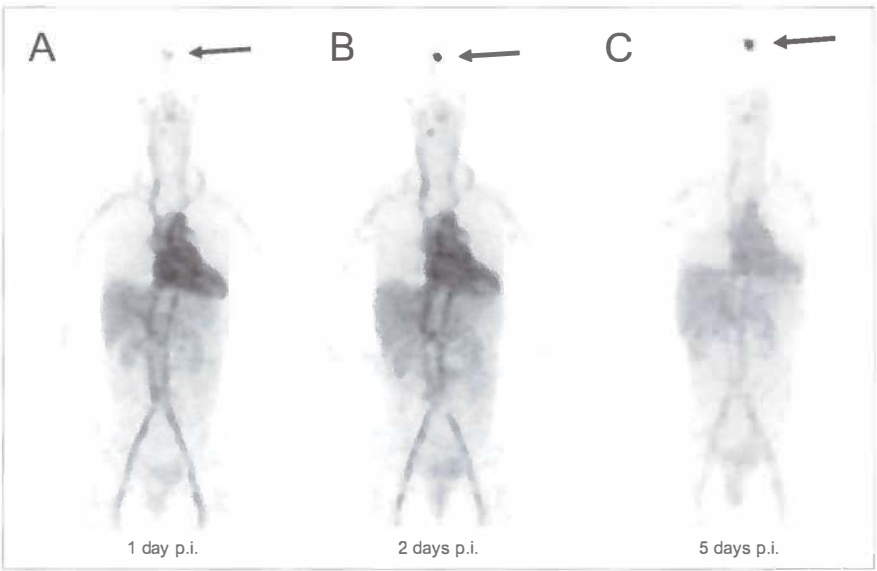

Figure 2. Three ^{89}Zr-trastuzumab scans of a patient on trastuzumab treatment show the increase in time in tumor-to-nontumor ratio (A-C). Arrow indicates ^{89}Zr-trastuzumab uptake in the only lesion.

tumor lesions was found to be 4–5 days after the injection of 37 MBq ^{89}Zr-trastuzumab.

Visual analysis of the PET scans revealed ^{89}Zr-trastuzumab biodistribution to liver, spleen, and kidney. This is in accordance with what was expected for these well-perfused organs. The ^{89}Zr-trastuzumab uptake in other nontumor tissues (e.g., lung, muscle, bone, and brain) was low.

In cohort 1, one of the two trastuzumab-naive patients showed accumulation of ^{89}Zr-trastuzumab in skin and liver metastases.

In both cohort 2 and cohort 3, the majority of the lesions previously identified in the patients by computed tomography (CT), magnetic resonance imaging (MRI), or bone scans could also be seen on the ^{89}Zr-trastuzumab PET scan. Visually, no difference was evident between cohorts 2 and 3 with respect to the uptake of ^{89}Zr-trastuzumab in tumor lesions. We anticipated that, because cohorts 2 and 3 would have sufficient ^{89}Zr-trastuzumab in the circulation (in contrast to cohort 1), there would be sufficient ^{89}Zr-trastuzumab available for accumulation in the tumors in these two cohorts. In addition, because the relative uptake values (RUVs) for these two cohorts were very similar (as shown in Table 2), the cohorts' data

Table 2. Individual ^{89}Zr-trastuzumab HER2 PET results

	^{89}Zr-trastuzumab protein dose													
Parameter	10 mg		50 mg					10 mg during trastuzumab therapy						
Age (years)	62	58	40	44	41	61	32	39	74	41	44	51	53	55
Body weight (kg)	97	71	86	70	66	65	69	77	47	60	75	73	72	78
Calculated trastuzumab dose, mg[1]	-	-	-	-	-	-	-	220	130	675	570	185	504	600
Scan 1 (n days post tracer injection)	1	3	1	1	1	2	1	3	3	3	3	1	1	1
Scan 2 (n days post tracer injection)	4	5	2	2	4	4	2	5	5	5	5	5	2	2
Scan 3 (n days post tracer injection)	-	-	5	6	-	-	5	-	-	-	7	-	5	5
RUV bloodpool	2.6	1.9	3.8	3.2	5.2	3.8	2.1	6.0	5.8	5.8	6.7	3.7	6.0	6.6
RUV liver	10.3	9.4	3.7	3.3	6.0	4.2	10.1	4.0	5.4	6.8	5.8	5.1	4.6	4.0
RUV spleen	3.4	1.9	1.9	2.4	3.2	3.0	1.4	3.0	3.1	4.0	3.5	3.4	3.0	2.6
RUV kidney	5.7	3.9	4.5	4.8	4.4	4.3	3.3	3.0	3.3	3.8	3.3	3.7	4.0	4.1
RUV intestine	6.6	6.3	1.8	2.1	2.7	2.7	1.5	2.1	2.1	2.9	1.8	2.8	1.9	2.3
RUV brain	0.13	0.12	n.a.	n.a.	n.a.	0.19	0.26	0.19	0.46	0.23	0.17	0.13	0.18	0.16
RUV lesion 1		18.6[2]	3.5[4]		3.8[4]	5.0[4]	19.4[2]	4.6[4]	9.2[2]	3.0[4]		4.3[6]	8.4[5]	5.2[2]
RUV lesion 2		20.4[2]	2.8[4]				0.86[5]	3.2[4]	11.6[2]	3.0[4]		2.7[4]		
RUV lesion 3		4.8[3]	5.0[4]					3.6[4]	8.6[2]			9.2[2]		
RUV lesion 4			4.2[4]						8.6[4]					
RUV lesion 5									1.4[5]					

[1] The amount of trastuzumab present at the time of ^{89}Zr-trastuzumab HER2 PET was calculated from the trastuzumab dose and the interval between the last trastuzumab dosing prior to ^{89}Zr-trastuzumab HER2 PET
[2] Liver metastasis
[3] Skin ulceration
[4] Bone metastasis
[5] Brain metastasis
[6] Lung metastasis
[7] Abbreviations: RUV, Relative Uptake Value calculated for the late time point scan (ranging 4-6 days postinjection); n.a., not available.

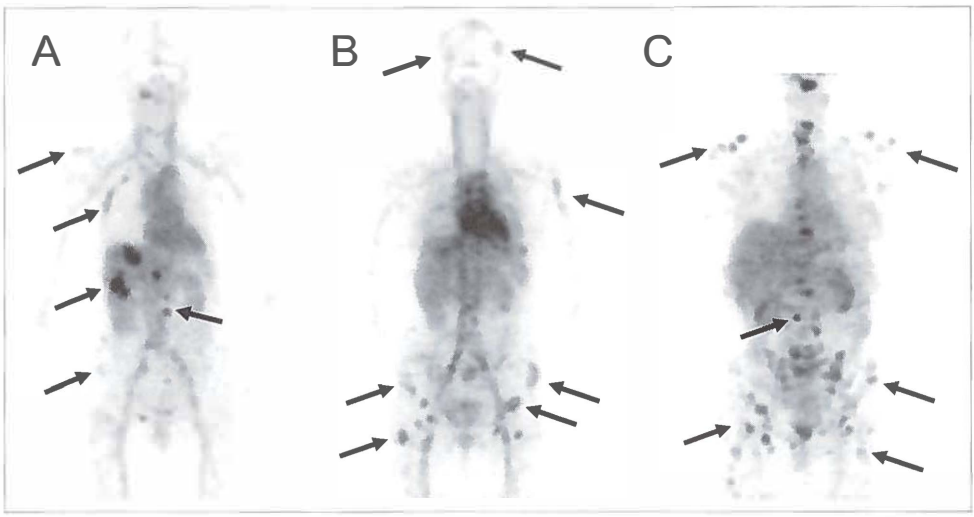

Figure 3. Examples of ^{89}Zr-trastuzumab uptake 5 days p.i. in a patient with liver and bone metastases (A) and two patients with multiple bone metastases (B+C). A number of lesions have been specifically indicated by the arrows.

pertaining to uptake of ^{89}Zr-trastuzumab in tumors were pooled (n = 12). In 6 of these 12 patients, ^{89}Zr-trastuzumab PET did not detect all the known lesions.

Known liver lesions were visualized by ^{89}Zr-trastuzumab in four of seven patients. No uptake of ^{89}Zr-trastuzumab took place in liver lesions in two of the patients in cohort 2 and one patient in cohort 3. Fig. 3A, an image from a representative patient with liver and bone metastases as revealed by CT and bone scan, shows a clear distinction between normal and pathological ^{89}Zr-trastuzumab uptake in the liver on the day-5 scan. ^{89}Zr-trastuzumab PET did not reveal any liver lesions.

At the time of the tracer injection, one of the patients with known liver metastases had been receiving trastuzumab treatment for 2 months. A CT scan performed directly after the PET scan (following ^{89}Zr-trastuzumab administration) showed a partial tumor response. This response, probably associated with tumor cell apoptosis and receptor occupation and/or internalization, might explain the negative results of the ^{89}Zr-trastuzumab PET scan.

Multiple bone lesions, noted on bone scans, CT, or MRI, were visualized by ^{89}Zr-trastuzumab PET in seven of nine patients. The two patients in whom the bone lesions did not show uptake of ^{89}Zr-trastuzumab were in cohort 3. Representative examples of ^{89}Zr-trastuzumab uptake in bone lesions are shown in Fig. 3A–C. The various bone lesions in the two patients are shown in the ^{89}Zr-trastuzumab PET

scans and were in good agreement with ^{99m}Tc-HDP bone scans. Fig. 4A shows the ^{89}Zr-trastuzumab uptake in a vertebral metastasis detected earlier by MRI. Bone lesions that had not been detected by other scans were discovered by PET scan in one patient in cohort 2.

In three patients, brain metastases were visualized by ^{89}Zr-trastuzumab PET. In one patient (from cohort 2) with two brain lesions as seen on MRI, the PET scan showed ^{89}Zr-trastuzumab accumulation in one of the metastases (measuring 2.0 × 1.6 cm on MRI); the other tumor lesion (measuring 0.5 × 0.5 cm on MRI) did not show up in the PET scan. In two other patients (one each in cohorts 2 and 3), ^{89}Zr-trastuzumab PET imaging revealed previously undetected brain metastases, both subsequently confirmed by MRI (Fig. 4B). The smallest brain lesion revealed by ^{89}Zr-trastuzumab PET imaging measured 0.7 × 0.7 cm on MRI.

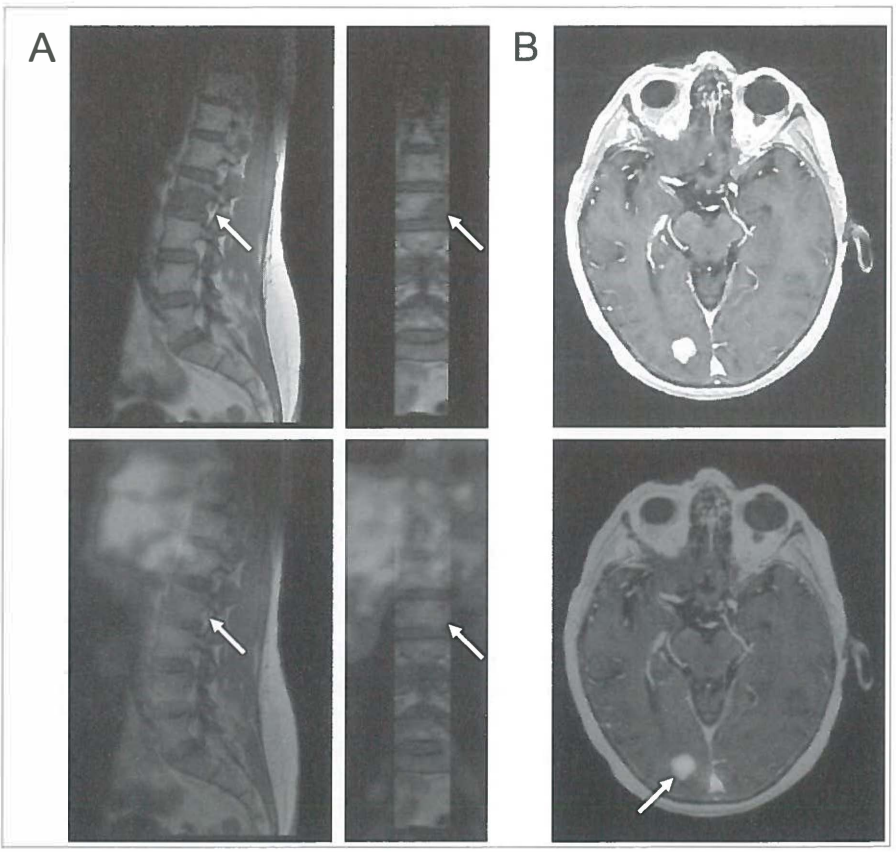

Figure 4. Examples of HER2-PET MRI fusion images. HER2 status of a vertebral metastasis known on MRI unapproachable for biopsy was revealed by ^{89}Zr-trastuzumab uptake on HER2-PET (A). Example of HER2-PET detected unknown brain lesion, which was later confirmed by MRI (B). Arrow indicates lesions. See page 171 for full color image.

The uptake of ^{89}Zr-trastuzumab in metastatic lesions and normal tissue was quantified as RUV_{mean}. The uptake in metastatic lesions was also quantified as RUV_{max}; this showed an excellent correlation (R^2 = 0.974; slope 1.36) between RUV_{mean} and RUV_{max}, indicating a homogeneous uptake within the lesions. Liver lesions displayed the highest level of uptake (12.8 ± 5.8), higher than that of normal liver (5.9 ± 2.4, P = 0.0070) or that of any other normal tissue (Fig. 5). Uptake in brain lesions was higher than in normal brain tissue (3.5 ± 4.2 vs. 0.20 ± 0.1, P = 0.0127), although there was a relatively large variation in uptake values between types of lesions. ^{89}Zr-trastuzumab RUV_{mean} in bone lesions was 4.1 ± 1.6. The uptake for normal bone was too low to be quantified. The RUV_{mean} of the only lung lesion was 4.3.

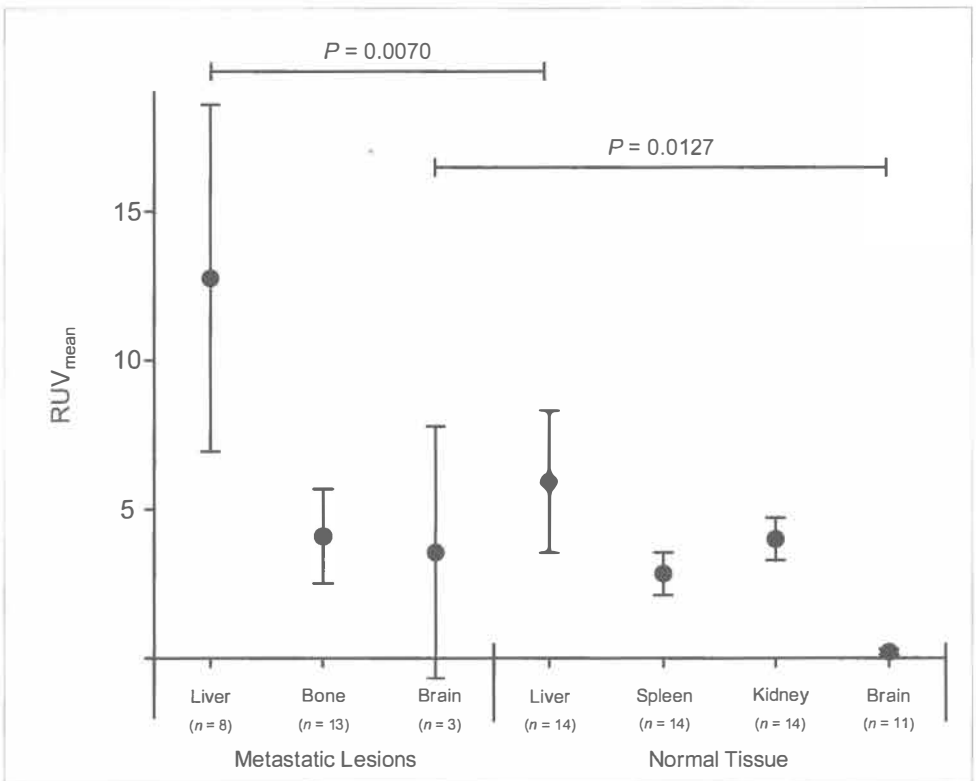

Figure 5. Relative uptake values (RUV) are quantified for metastatic lesions and normal liver, spleen, kidney and brain. RUVs shown here are from the late time point scans.

DISCUSSION

This first-in-human ^{89}Zr-trastuzumab HER2-PET imaging study showed excellent tumor uptake and visualization of HER2-positive metastatic liver, lung, bone, and even brain tumor lesions, when an adequate trastuzumab protein dose was administered. In trastuzumab-naive patients with HER2-positive metastatic breast cancer, 50 mg of trastuzumab was the dose that resulted in optimal biodistribution characteristics under the test conditions and proved adequate for ^{89}Zr-trastuzumab PET imaging. The 50 mg trastuzumab dose in naive patients is a good starting point for further optimization in future studies. In patients undergoing treatment with trastuzumab at the time of tracer injection, 10 mg trastuzumab was adequate for PET imaging. Higher doses of trastuzumab were not expected to improve ^{89}Zr-trastuzumab PET imaging; trastuzumab clearance was already minimal, and therefore a further increase in the dose of trastuzumab could induce target saturation. Quantification of the PET images confirmed the dose-dependency of trastuzumab clearance and revealed a significantly higher uptake in metastatic tumor lesions as compared to corresponding normal tissue. In this study, ^{89}Zr-trastuzumab allowed the researchers to distinguish between lesions with HER2 overexpression and those without. The exact amount of HER2 expression required for adequate imaging will have to be determined in a future biopsy-aligned study.

The rapid ^{89}Zr-trastuzumab clearance, as seen with a 10 mg dose administered to trastuzumab-naive patients in cohort 1, is in accordance with trastuzumab pharmacokinetic data from phase I studies.[15;16] After multiple doses at therapeutic concentrations, trastuzumab clearance has an average terminal half-life of 28.5 days at steady state.[17] However, when given as a single dose of 10 or 50 mg, trastuzumab is known to have an average terminal half-life of 1.5 or 4.3 days, respectively.[15] This short-terminal half-life is probably too brief to allow adequate accumulation of the tracer in the tumors and subsequent imaging when 10 mg of the tracer is used in trastuzumab-naive patients. This analysis is supported by the presence of ^{89}Zr in the intestinal tract in patients in cohort 1.

Dose-dependent pharmacokinetics has also been shown to hold good for the trastuzumab–DM1 antibody–drug conjugate and for the HER2 antibody pertuzumab.[18;19] The exact mechanisms underlying these dose-dependent pharmacokinetics of HER2-targeted antibodies are not known, but they probably involve rapid but saturable elimination of low doses from the first compartment of distribution, i.e., the circulation, during the first elimination phase. Elimination

of trastuzumab is characterized by two phases; a first phase with a half-life of ~4 days, followed by a second phase that starts ~1 week after infusion, with a much longer half-life.[20] Saturable elimination in the first phase is probably caused by antibody catabolism followed by excretion of the catabolites. A second mechanism that can play a role in increasing ^{89}Zr-trastuzumab clearance in trastuzumab-naive patients is the presence of high plasma levels of extracellular domains shed by HER2.[17] After the binding of trastuzumab to these extracellular domains, this complex is cleared by the liver and excreted in the intestines.

The administered ^{89}Zr dose of 37 MBq proved to be sufficient for adequate imaging up to 5 days after the injection. Because of the balance between the relatively slow accumulation of trastuzumab in the tumors and the radioactive decay of ^{89}Zr, a suitable time for assessing ^{89}Zr-trastuzumab tumor uptake was found to be 4–5 days after the injection. The PET images produced with ^{89}Zr-trastuzumab showed high spatial resolution and good signal-to-noise ratio, resulting in an image quality unapproachable by our previous ^{111}In-trastuzumab SPECT scans.[11;21] As compared to the 75 MBq used in the only earlier clinical study with ^{89}Zr, the 37 MBq used in the present study resulted in a lower radiation dose to the patient while preserving image quality.[12] On the basis of the previous ^{111}In-trastuzumab study (after substituting nuclide properties) the ^{89}Zr-trastuzumab radiation dose was estimated at 18 mSv, comparable to two abdominal CT scans.[22]

Although our study was not designed for head-to-head comparison with conventional staging modalities or for assessing sensitivity and specificity, lesions with ^{89}Zr-trastuzumab uptake were generally in agreement with available data from CT, MRI, and bone scans. In approximately half the patients evaluated, PET scans showed no uptake of ^{89}Zr-trastuzumab in certain tumor lesions, although these lesions had previously been identified with conventional imaging. This may be attributable to variable HER2 expression in different lesions in the same patient,[4-7] although this cannot be stated with absolute certainty because no biopsies of those specific lesions were carried out. It is unlikely that in cohort 3 (patients on trastuzumab treatment) some of the tumor lesions had no uptake of ^{89}Zr-trastuzumab due to saturation, because lesions overall showed up very well in this cohort. Therefore, future studies to assess the sensitivity and specificity of HER2-PET imaging should compare the uptake of ^{89}Zr-trastuzumab in tumor lesions with the pathological HER2 status of these lesions, as seen from biopsies. The process of obtaining biopsy specimens will need to be carefully performed

because tumor lesions may be difficult to access; an additional consideration is that undergoing more than one biopsy may be too burdensome to the patient.

Until additional information from these future studies becomes available, it will remain unclear whether nondetection of known lesions by ^{89}Zr-trastuzumab PET imaging occurs because of suboptimal imaging conditions (e.g., dosing and timing, lesion size, spatial resolution) or because the level of HER2 overexpression in these lesions has fallen below the limit detectable by PET.

The fact that we were able to visualize brain lesions was interesting, given that it is generally believed that trastuzumab has poor penetration of the brain.[23] This study shows that ^{89}Zr-trastuzumab can target brain lesions, with an 18-fold higher uptake in tumors than in normal brain tissue. This is probably because of a disruption of the blood–brain barrier at the site of the brain metastasis, and it supports the use of trastuzumab therapy in patients with HER2-positive breast cancer and brain metastases.

In addition to ^{89}Zr-trastuzumab and ^{111}In-trastuzumab, a few other tracers have been used for clinical HER2 imaging. The ^{99m}Tc-labeled anti-HER2 rat antibody ICR12 was administered to eight breast cancer patients in the early 1990s. This SPECT study suggested that ^{99m}Tc-ICR12 could be used for the imaging of HER2-positive disease, although no further clinical results involving this antibody have been made available.[24] Currently, clinical studies with ^{111}In- and ^{64}Cu-trastuzumab and with ^{68}Ga-trastuzumab F(ab')$_2$ fragments are at the stage of patient recruitment.[25] These studies will give insight into the possibility of using shorter-lived isotopes (such as ^{64}Cu) for imaging with intact antibodies and will provide the first clinical results with the smaller HER2-directed F(ab')$_2$ fragments. Generally, large intact monoclonal antibodies penetrate slowly but constantly into solid tumor tissue, ultimately resulting in higher accumulation in the tumor than is the case with small proteins; antibody fragments penetrate more swiftly into tumor tissue but show less uptake in the tumor because of more rapid clearance from the blood.[7]

If, in the future, other tracers prove to be more useful than ^{89}Zr-trastuzumab for HER2-PET imaging in patients, the choice of tracer might well depend on the purpose for which HER2-PET imaging is to be used. One can envision a role for HER2-PET imaging in improving diagnosis, staging (especially in clinical dilemmas such as when lesions are inaccessible for biopsy), guiding individual trastuzumab therapy, and early drug development of HER2-targeting agents.[7;26]

This feasibility evaluation of biodistribution and imaging points to the need for further exploration of ^{89}Zr-trastuzumab HER2-PET imaging.

Acknowledgments

This study was supported by grant 2007-3739 from the Dutch Cancer Society.

References

1. Gross ME, Shazer RL, Agus DB. Targeting the HER-kinase axis in cancer. Semin Oncol 2004;31:9-20
2. Slamon DJ, Leyland-Jones B, Shak S, et al. Use of chemotherapy plus a monoclonal antibody against HER2 for metastatic breast cancer that overexpresses HER2. N Engl J Med 2001;344:783-92
3. Piccart-Gebhart MJ, Procter M, Leyland-Jones B, et al. Trastuzumab after adjuvant chemotherapy in HER2-positive breast cancer. N Engl J Med 2005;353:1659-72
4. Rasbridge SA, Gillett CE, Seymour AM, et al. The effects of chemotherapy on morphology, cellular proliferation, apoptosis and oncoprotein expression in primary breast carcinoma. Br J Cancer 1994;70:335-41
5. Solomayer EF, Becker S, Pergola-Becker G, et al. Comparison of HER2 status between primary tumor and disseminated tumor cells in primary breast cancer patients. Breast Cancer Res Treat 2006;98:179-84
6. Wulfing P, Borchard J, Buerger H, et al. HER2-positive circulating tumor cells indicate poor clinical outcome in stage I to III breast cancer patients. Clin Cancer Res 2006;12:1715-20
7. Dijkers EC, de Vries EG, Kosterink JG, et al. Immunoscintigraphy as potential tool in the clinical evaluation of HER2/neu targeted therapy. Curr Pharm Des 2008;14:3348-62
8. National Comprehensive Cancer Network (NCCN) Practice Guidelines in Oncology - v.1.2009, www.nccn.org, accessed November 2009
9. Breast Cancer Treatment (PDQ®), www.cancer.gov, accessed November 2009
10. Lear-Kaul KC, Yoon HR, Kleinschmidt-DeMasters BK, et al. Her-2/neu status in breast cancer metastases to the central nervous system. Arch Pathol Lab Med 2003;127:1451-57
11. Perik PJ, Lub-De Hooge MN, Gietema JA, et al. Indium-111-labeled trastuzumab scintigraphy in patients with human epidermal growth factor receptor 2-positive metastatic breast cancer. J Clin Oncol 2006;24:2276-82
12. Borjesson PK, Jauw YW, Boellaard R, et al. Performance of immuno-positron emission tomography with zirconium-89-labeled chimeric monoclonal antibody U36 in the detection of lymph node metastases in head and neck cancer patients. Clin Cancer Res 2006;12:2133-40
13. Dijkers ECF, Kosterink JG, Rademaker AP, et al. Development and characterization of clinical grade ^{89}Zr-trastuzumab for HER2/neu immunoPET imaging. J Nucl Med 2009;50:974-81
14. Loening AM, Gambhir SS. AMIDE: a free software tool for multimodality medical image analysis. Mol Imaging 2003;2:131-37

15. FDA Clinical Review of BLA 98-0369: Herceptin Trastuzumab (rhuMAb HER2), in, www.fda.gov, accessed November 2009
16. Tokuda Y, Watanabe T, Omuro Y, et al. Dose escalation and pharmacokinetic study of a humanized anti-HER2 monoclonal antibody in patients with HER2/neu-overexpressing metastatic breast cancer. Br J Cancer 1999;81:1419-25
17. Bruno R, Washington CB, Lu JF, et al. Population pharmacokinetics of trastuzumab in patients with HER2+ metastatic breast cancer. Cancer Chemother Pharmacol 2005;56:361-69
18. Beeram M, Burris HA, Modi S, et al. A phase I study of trastuzumab-DM1 (T-DM1), a first-in-class HER2 antibody-drug conjugate (ADC), in patients (pts) with advance HER2+ breast cancer (BC). J Clin Oncol 2008;26 suppl:abstr 1028
19. Agus DB, Gordon MS, Taylor C, et al. Phase I clinical study of pertuzumab, a novel HER dimerization inhibitor, in patients with advance cancer. J Clin Oncol 2005:23:2534-43
20. Baselga J, Carbonell X, Castaneda-Soto NJ, et al. Phase II study of efficacy, safety and pharmacokinetics of trastuzumab monotherapy administered on a 3-weekly schedule. J Clin Oncol 2005;23:2162-71
21. de Korte MA, de Vries EG, Lub-de Hooge MN, et al. ^{111}Indium-trastuzumab visualises myocardial human epidermal growth factor receptor 2 expression shortly after anthracycline treatment but not during heart failure: a clue to uncover the mechanisms of trastuzumab-related cardiotoxicity. Eur J Cancer 2007;43:2046-51
22. Brenner DJ, Hall EJ. Computed tomography--an increasing source of radiation exposure. N Engl J Med 2007;357:2277-84
23. Lin NU, Winer EP. Brain metastases: the HER2 paradigm. Clin Cancer Res 2007;13:1648-55
24. Allan SM, Dean C, Fernando I, et al. Radioimmunolocalisation in breast cancer using the gene product of c-erbB2 as the target antigen. Br J Cancer 1993;67:706-12
25. United States National Institutes of Health, www.clinicaltrials.gov, accessed November 2009
26. van Dongen GA, Visser GW, Lub-De Hooge MN, et al. Immuno-PET: a navigator in monoclonal antibody development and applications. Oncologist 2007;12:1379-89

Chapter 6B:

Trastuzumab pharmacokinetics influenced by extent HER2-positive tumor load

Thijs Oude Munnink[1]
Eli Dijkers[2]
Sabine Netters[1]
Marjolijn Lub-de Hooge[2,3]
Adrienne Brouwers[3]
Janny Haasjes[4]
Carolina Schröder[1]
Elisabeth de Vries[1]

Departments of Medical Oncology[1], Hospital and Clinical Pharmacy[2], and Nuclear Medicine and Molecular Imaging[3], University Medical Center Groningen, Groningen, The Netherlands; Department of Internal Medicine[4], Bethesda Hospital, Hoogeveen, The Netherlands.

Journal of Clinical Oncology 2010;28:e355-6

TO THE EDITOR:

We read with great interest the article by Leyland-Jones et al.[1], in which an intensified trastuzumab loading dose was evaluated in patients with human epidermal growth factor receptor-2 (HER2) positive metastatic breast cancer. They conclude that a trastuzumab loading dose of weekly 6 mg/kg during the first 3 weeks followed by 3-weekly 6 mg/kg proved to be safe and effective, with higher-than-steady-state concentrations during the first cycle. This intensified schedule was based on pharmacokinetic modeling using population based pharmacokinetic parameters from a pooled phase I/II dataset. Pharmacokinetic data with this intensified schedule do indeed show an optimized profile compared to the standard weekly dosing of trastuzumab. However, pharmacokinetic parameters like terminal half-life, area under the concentration-time curve, maximum concentration and minimum concentration do still have remarkably broad ranges: the 5th to 95th percentile ranged 8.23-31.4 days, 1.790-3450 mg x day/L, 173-338 mg/L and 34.8-173 mg/L respectively.[1] This suggests that for optimal trastuzumab treatment, dosing on merely kg bodyweight is probably insufficient, and that other individual patient factors affecting trastuzumab pharmacokinetics should be taken into account. Trastuzumab clearance is highly dose dependent[2] and is increased in case of high tumor load (with ≥4 metastatic sites) or, to a lesser extent, high HER2 extracellular domain (ECD) plasma levels.[3]

For complete understanding of trastuzumab pharmacokinetics and optimal dosing, it is necessary to gain insight in trastuzumab body distribution and blood pharmacokinetics. We have shown that whole body imaging with radiolabeled trastuzumab can indeed provide quantitative data on trastuzumab tumor uptake and organ distribution in addition to blood pool levels.[4;5] Recent striking findings with zirconium-89 (^{89}Zr)-trastuzumab HER2-PET imaging in one patient with extensive tumor load significantly contributed to our knowledge on trastuzumab pharmacokinetics and how these can be influenced by tumor load.

A 41 year old woman was newly diagnosed with HER2-positive breast cancer, with bone- and liver metastases. Brain metastases were suspected but could not be detected by means of conventional techniques. With HER2-PET imaging we have previously shown that ^{89}Zr-trastuzumab accumulates in tumor lesions including HER2-positive brain metastases.[5] Therefore, this patient was referred to our center to exclude presence of HER2-positive brain metastases by means of

HER2-PET. At this stage, the patient had not received therapeutic trastuzumab treatment yet.

In a feasibility study, we found that 50 mg ^{89}Zr-trastuzumab, consisting of 1.5 mg ^{89}Zr-trastuzumab (37 MBq) replenished with non-radioactive trastuzumab, is a dose for optimal HER2 visualization in trastuzumab naive patients. Lower trastuzumab doses resulted in rapid hepato-intestinal excretion.[5] The first HER2-PET scan of the referred patient was acquired two days after injection of 50 mg ^{89}Zr-trastuzumab. It showed massive ^{89}Zr-trastuzumab uptake in the liver metastases (48% of injected dose; Fig. 1A) and presence in the colon ascendens/transversum, indicating intestinal excretion of ^{89}Zr-trastuzumab or its catabolites. ^{89}Zr-trastuzumab blood pool levels were extremely low, bone metastases were hardly visible and no uptake was seen in the brain. This pattern of rapid clearance and low blood pool levels of ^{89}Zr-trastuzumab was unprecedented in our feasibility study.[5] The high ^{89}Zr-trastuzumab uptake in the extensive liver metastases might have reduced uptake in other tumor lesions such as bone or brain and have resulted in a false negative HER2-PET scan for brain

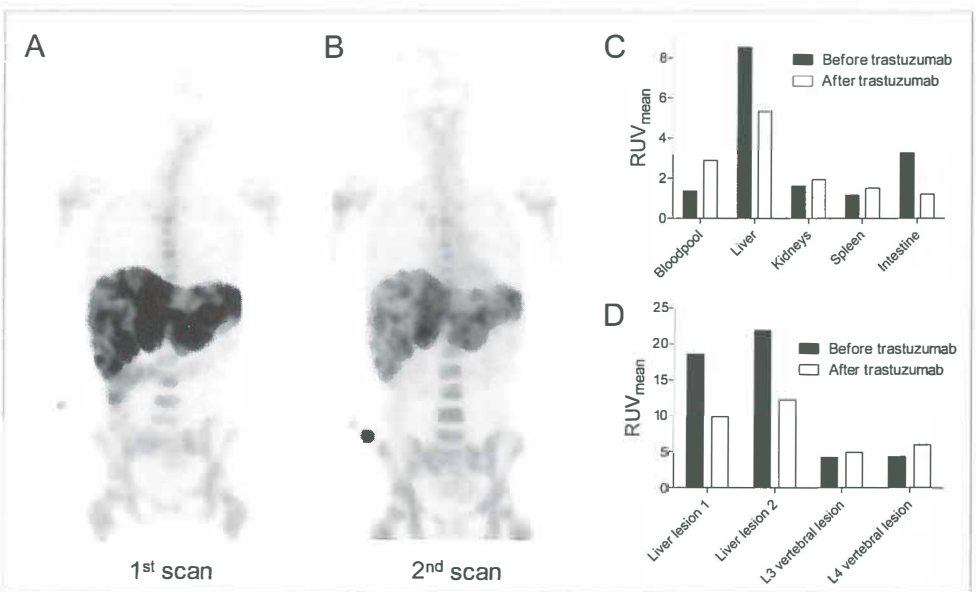

Figure 1. ^{89}Zr-trastuzumab HER2-PET scan was acquired 2 days after injection of 50 mg ^{89}Zr-trastuzumab (A). After a trastuzumab loading dose of 220 mg, this patient was reinjected with 10 mg ^{89}Zr-trastuzumab and a HER2-PET scan was acquired two days later (B; intense spot in right arm is injection site). ^{89}Zr-trastuzumab uptake was quantified as relative uptake value (RUV) for normal tissue (C) and lesions (D).

lesions. Therefore a second ^{89}Zr-trastuzumab dose was injected two days after initiation of treatment with paclitaxel and trastuzumab (220 mg; 4 mg/kg loading dose) and the HER2-PET scan was acquired two days later. The protein dose of ^{89}Zr-trastuzumab was reduced to 10 mg, given the prior start of therapeutic trastuzumab treatment. Compared to the first HER2-PET scan, this scan showed less ^{89}Zr-trastuzumab liver uptake (33% of injected dose), a higher blood pool level and more uptake in other tumor lesions, such as bone metastases (Fig. 1B). Quantification of ^{89}Zr-trastuzumab relative uptake values in tumor and organs (including kidneys and spleen), indicated a reduction in uptake in two liver lesions of respectively 47 and 44%, and increased uptake in vertebrae L3 and L4 of respectively 16% and 37% on the second scan (Fig. 1C and 1D). Treatment was continued with paclitaxel and trastuzumab with an excellent tumor response and all neurological signs disappeared.

In this patient we show that due to an extensive HER2-positive tumor mass, ^{89}Zr-trastuzumab was predominantly taken up by liver metastases and rapidly cleared from the circulation. The rapid ^{89}Zr-trastuzumab clearance in this patient can theoretically be explained as follows. Considering a $2x10^6$ HER2 per tumor cell[6], a liver tumor mass of 1.2 kg (based on patient's enlarged liver volume of 2513 cm^3 on PET scan and a calculated[7] normal healthy liver weight of 1.3 kg) and $1x10^9$ cells/g tumor, the liver metastases alone would already contain ~$2.4x10^{18}$ HER2 molecules. The first ^{89}Zr-trastuzumab dose of 50 mg consists of $2.0x10^{17}$ trastuzumab molecules and can therefore be easily completely bound by the receptors on the tumor cells in the liver metastases, which resulted in a rapid liver uptake and ^{89}Zr-trastuzumab clearance from the circulation as was seen with HER2-PET imaging. The scan after the therapeutic loading dose of 220 mg trastuzumab still showed very low ^{89}Zr-trastuzumab blood pool levels compared to previous results.[5] The total amount of trastuzumab administrated to this patient within one week was 280 mg (both tracer doses plus loading dose), which can only saturate 47% of all HER2 present in the liver metastases based on our calculations. This indicates that it takes more trastuzumab to saturate lesions in case of extensive HER2-positive tumor load.

In conclusion, the current practice of trastuzumab dosing for metastatic breast cancer, may indeed have to be reconsidered. Leyland-Jones et al. showed with their intensified loading schedule an improved pharmacokinetic profile of trastuzumab.[1] In addition, our data indicate that trastuzumab pharmacokinetics and organ distribution can be heavily affected by an extensive tumor load. It

could therefore be considered to perform a study with a more patient tailored trastuzumab dosing schedule based on tumor volume in addition to bodyweight. In such a study, HER2-PET can be used to assess whether this results in more effective trastuzumab levels in all lesions compared to dosing based on a patient's bodyweight.

References

1. Leyland-Jones B, Colomer R, Trudeau ME, et al. Intensive loading dose of trastuzumab achieves higher-than-steady-state serum concentrations and is well tolerated. J Clin Oncol 2010;28:960-6
2. FDA clinical review of BLA 98-0369: Herceptin trastuzumab (rhuMAb HER2). *www.fda.gov*, accessed January 2010
3. Bruno R, Washington CB, Lu JF, et al. Population pharmacokinetics of trastuzumab in patients with HER2+ metastatic breast cancer. Cancer Chemother Pharmacol 2005;56:361-9
4. Perik PJ, Lub-de Hooge MN, Gietema JA, et al. Indium-111-labeled trastuzumab scintigraphy in patients with human epidermal growth factor receptor 2-positive metastatic breast cancer. J Clin Oncol 2006;24:2276-82
5. Dijkers ECF, Oude Munnink TH, Kosterink JG, et al. Biodistribution of ^{89}Zr-trastuzumab and PET imaging of HER2-positive lesions in metastatic breast cancer patients. Clin Pharmacol Ther 2010;87:586-92.
6. Pegram MD, Konecny G, Slamon DJ. The molecular and cellular biology of HER2/neu gene amplification/overexpression and the clinical development of herceptin (trastuzumab) therapy for breast cancer. Cancer Treat Res 2000;103:57-75
7. Yoshizumi T, Gondolesi GE, Bodian CA, et al. A simple new formula to assess liver weight. Transplant Proc 2003;35:1415-20

Chapter 7:

PET imaging with ^{89}Zr labeled transforming growth factor (TGF)-β antibody fresolimumab in tumor models

Thijs Oude Munnink[1]
Marlous Arjaans[1]
Hetty Timmer-Bosscha[1]
Carolina Schröder[1]
Jan Willem Hesselink[1]
Silke Vedelaar[1]
Annemiek Walenkamp[1]
Michael Reiss[2]
Richard Gregory[3]
Marjolijn Lub-de Hooge[4,5]
Elisabeth de Vries[1]

Departments of Medical Oncology[1], Nuclear Medicine and Molecular Imaging[4], Hospital and Clinical Pharmacy[5], University Medical Center Groningen, Groningen, The Netherlands; Departments of Medicine, Molecular Genetics, Microbiology & Immunology[2], Robert Wood Johnson Medical School and Cancer Institute of New Jersey, New Brunswick, NJ, USA; Oncology Research[3], Genzyme Corporation, Framingham, MA, USA.

Journal of Nuclear Medicine 2011; in press

ABSTRACT

Transforming growth factor-β (TGF-β) promotes cancer invasion and metastasis and is therefore a potential drug target for cancer treatment. Fresolimumab, a monoclonal antibody which neutralizes all mammalian active isoforms of TGF-β, was radiolabeled with zirconium-89 (^{89}Zr) for PET imaging to analyze TGF-β expression, antibody tumor uptake and organ distribution.

^{89}Zr was conjugated to fresolimumab using the chelator N-succinyl-desferrioxamine-B-tetrafluorphenol. ^{89}Zr-fresolimumab was analyzed for conjugation ratio, aggregation, (radiochemical) purity, stability and immunoreactivity. ^{89}Zr-fresolimumab tumor uptake and organ distribution was assessed using three protein doses (10, 50 and 100 μg) and compared with ^{111}In-IgG in a human TGF-β transfected CHO xenograft model, a human breast cancer MDA-MB-231 xenograft and metastatic model. Latent and active TGF-β1 expression was analyzed in tissue homogenates with ELISA.

^{89}Zr was labeled to fresolimumab with high specific activity (> 1 GBq/mg), high yield and high purity (> 95%). *In vitro* validation of ^{89}Zr-fresolimumab showed a fully preserved immunoreactivity and long (> 1 week) stability in solution and in human serum. *In vivo* validation showed a ^{89}Zr-fresolimumab distribution similar to IgG in most organs, except for a higher uptake in liver in all mice and higher kidney uptake in the 10 μg group. ^{89}Zr-fresolimumab induced no toxicity in mice. It accumulated in primary tumors and metastases similar to IgG. Both latent and active TGF-β were detected in tumor homogenates, while only latent TGF-β could be detected in liver homogenates. Remarkably high ^{89}Zr-fresolimumab uptake was seen in sites of tumor ulceration and in scar tissue, processes in which TGF-β is known to be highly active.

Conclusion: Fresolimumab tumor uptake and organ distribution can be visualized and quantified with ^{89}Zr-fresolimumab PET imaging. This technique will be used to guide further clinical development of fresolimumab and could possibly identify patients most likely to benefit.

INTRODUCTION

The pleiotropic transforming growth factor-β (TGF-β) is excreted in low amounts by multiple cell types to prevent progression of premalignant lesions.[1;2] In many tumor types the tumor suppressive responses to TGF-β are lost in the malignant phase, where tumor promotive responses to TGF-β (including epithelial-to-mesenchymal transition, angiogenesis, extravasation, migration, invasion and immune suppression) prevail. TGF-β thereby contributes to a more invasive and metastatic tumor phenotype.[1;3] Mechanisms involved in this suppressor to promoter switch are diverse and include mutations (and epigenetic silencing) in the suppressive pathway, and increased TGF-β production, release and activation in the tumor microenvironment.[1;4;5] Activity of TGF-β is locally controlled in the extracellular matrix by cleavage of active TGF-β dimers from the latent precursor.[6;7]

TGF-β is a potential drug target for cancer treatment, especially in case of highly invasive or metastatic tumors such as glioblastomas and metastatic breast cancer.[8;9] Strategies in clinical development for TGF-β inhibition include antisense oligonucleotides, TGF-β neutralizing antibodies and small molecule TGF-β receptor kinase inhibitors.[9;10] Clinical TGF-β imaging can have an unprecedented role in the development of these TGF-β targeted agents, since the dual functions of TGF-β in cancer makes proper patient selection of crucial value. Selection seems especially important in breast cancer. Pathway analysis identified a subset of breast cancer patients with high expression of TGF-β pathway genes and an association with shorter distant-metastasis-free survival, indicating a potential benefit of TGF-β inhibition for these patients.[11] In addition, others have identified a subset of patients with abrogated TGF-β signaling which was associated with reduced relapse-free survival.[12]

Improved insight into the role of TGF-β in breast cancer invasion and metastasis has recently been provided in a number of elegant preclinical optical imaging studies. Live intravital imaging of TGF-β signaling in tumor cells was performed in an orthotopic mouse model using rat breast cancer cells (MTLn3E) transfected with cyan fluorescent protein TGF-β dependent reporter constructs. Here, TGF-β signaling was transiently and locally activated in single moving tumor cells. TGF-β activated single moving cells demonstrated increased tendency to infiltrate surrounding tissues and were consequently responsible for distant metastases.[13] TGF-β bioluminescence imaging using human breast cancer cells (MDA-MB-231) transfected with TGF-β responsive luciferase constructs indicated a temporal

TGF-β dependency of bone metastases and an antimetastatic effect of TGF-β inhibition.[14;15] These TGF-β responsive imaging approaches have provided a great extension of our understanding of TGF-β signaling in metastasis, but regretfully are restricted to preclinical use because of the use of transfections and the poor tissue penetration of optical techniques. Clinically applicable TGF-β imaging techniques would therefore be of value in our clinical understanding of TGF-β, in the development of TGF-β targeting agents and in the selection of patients most likely to benefit.

Fresolimumab is a fully human IgG4 kappa monoclonal antibody capable of neutralizing all mammalian active isoforms of active TGF-β (1, 2, and 3). A phase I study with fresolimumab in 22 patients with advanced melanoma and renal cell carcinoma showed stable disease in one patient, a partial response in one patient and mixed tumor response in three patients, and no dose limiting toxicity.[16] For further clinical development of fresolimumab and to identify the patients most likely to benefit, it will be helpful to know whether TGF-β is being overexpressed and activated in the tumor, and if fresolimumab reaches the target. Labeling fresolimumab with the long-lived positron emitter zirconium-89 (^{89}Zr) should allow for non-invasive monitoring and quantification of fresolimumab tumor and organ distribution using positron emission tomography (PET). Preclinical studies, as well as, ongoing clinical studies with ^{89}Zr-bevacizumab for imaging vascular endothelial growth factor (VEGF), previously demonstrated the feasibility of PET imaging with antibodies against soluble ligands overexpressed in tumors.[17;18]

In this study, we describe the development, quality control and preclinical validation of ^{89}Zr-fresolimumab for non-invasive PET imaging of TGF-β tumor expression and organ distribution of fresolimumab. We used two human TGF-β transfected CHO xenograft models, one with intermediate and one with high TGF-β expression. In addition, we used a MDA-MB-231 xenograft and metastatic model of human breast cancer. The triple negative breast cancer cell line MDA-MB-231 was selected because of the considered role of TGF-β in triple negative breast cancer and the extensive data available concerning the role of TGF-β in this cell line.[14;15]

MATERIALS AND METHODS

Cell cultures

Chinese Hamster Ovary (CHO) clones were generated by transfection of DG44-CHO cells with human latent TGF-β1 (generously provided by Genzyme). Briefly, DG44-CHO cells were transfected with a human latent TGF-β1 cDNA using the SV2DHFR vector, and stable cell lines were generated by methotrexate selection. CHO Clone11S (CHO-Cl11S) and Clone2 (CHO-Cl2) were selected as they produced intermediate (23.3 ng per $1x10^6$ cells per day) and high (189 ng per $1x10^6$ cells per day) levels of human latent TGF-β1, respectively. CHO-Cl11S and CHO-Cl2 were cultured in a humidified incubator at 5% CO_2 and 37 ^{0}C in MEM, supplemented with 10% dialyzed fetal calf serum (FCS) and 2% L-glutamine. The triple negative breast cancer cell-line MDA-MB-231 (from ATCC), and its luciferase transfected bone-tropic clone MDA-MB-231-SCP2luc (provided by Y. Kang and described earlier[19]), were cultured in a humidified incubator at 5% CO_2 and 37 ^{0}C in D-MEM, supplemented with 10% FCS and 1% L-glutamine. Concentrations of active and total TGF-β1 in culture media were assessed using an enzyme-linked immuno sorbent assay (ELISA; R&D Systems) according to the manufacturers' protocol.

Conjugation, ^{89}Zr-labeling and quality control of fresolimumab

Fresolimumab (GC1008; provided by Genzyme) conjugation and labeling was performed as described by Verel et al.[20] Briefly, fresolimumab was first conjugated with the chelator N-succinyldesferrioxamine-B-tetrafluorphenol (N-sucDf-TFP; generously provided by prof.dr. GAMS van Dongen from VUMC) in 5-fold molar excess. After conjugation, the product was purified by ultracentrifugation using a 30 kDa Vivaspin-2 (Sartorius) and stored in water for injection at -20 ^{0}C. In the second step, N-sucDf-fresolimumab was freshly radiolabeled with clinical-grade ^{89}Zr oxalate (IBA Molecular) on the day of use.

N-sucDf-fresolimumab and ^{89}Zr-fresolimumab were analyzed for conjugation ratios, aggregation and (radiochemical) purity by size exclusion high performance liquid chromatography (SE-HPLC). The Waters SE-HPLC system was equipped with a dual-wavelength absorbance detector, an in-line radioactivity detector and a size exclusion column (Superdex 200 10/300 GL; GE Healthcare). Sodium phosphate buffer (0.025 M $Na_2HPO_4{\cdot}2H_2O$ / $NaH_2PO_4{\cdot}H_2O$) was used as mobile

phase. The retention time of fresolimumab was approximately 18 min, ^{89}Zr-N-SucDf and low-weight impurities eluted at 28 min (at a flow of 0.7 mL/min).

Stability of ^{89}Zr-fresolimumab was tested in 0.9% NaCl at 4 ^{0}C and in human serum at 37 ^{0}C using 20% trichloroacetic acid (TCA; Hospital Pharmacy, UMCG) precipitation. TCA precipitation was carried out in phosphate-buffered saline (PBS; 140 mM NaCl, 9 mM Na_2HPO_4, 1.3 mM NaH_2PO_4; pH = 7.4) with 0.5% human serum albumin (HSA; Sanquin) and 20% TCA. Radioactivity in precipitate and supernatant was determined by a calibrated well-type gamma-counter (LKB Wallac).

Immunoreactivity was tested in a competition assay with unlabeled fresolimumab. Recombinant human TGF-β3 (Peprotech) was used as target antigen because fresolimumab has the highest affinity (with a dissociation constant of 1.4 nM) for this TGF-β isoform and therefore binding to TGF-β3 serves as a sensitive indicator for immunoreactivity of ^{89}Zr-fresolimumab. TGF-β3 was diluted in PBS to a concentration of 4 μg/mL (pH was adjusted to 9.2–9.5 with 50 mmol/L Na_2CO_3) and coated to Nunc-Immuno BreakApart ELISA plates (NUNC). Fifty μL was added to the wells, incubated overnight at 4 ^{0}C, and then blocked with 1% HSA in PBS. After blocking, plates were washed with 0.1% polysorbate 80 (Sigma-Aldrich) in PBS. ^{89}Zr-fresolimumab and fresolimumab were mixed and diluted in PBS to result in a fixed concentration of 14 nM ^{89}Zr-fresolimumab and varying concentrations of unlabeled fresolimumab, ranging 14 pM tot 14 μM. These samples were added to the wells, and incubated for 2 h. Samples were collected in 2 wash steps. Both ^{89}Zr-fresolimumab bound to the TGF-β3-coated wells and the collected samples containing unbound ^{89}Zr-fresolimumab were measured for radioactivity. Percentage of TGF-β3 binding was calculated as the fraction of radioactivity bound to TGF-β3-coated wells divided by the total amount of radioactivity added. These percentages were plotted using Prism software (GraphPad), and the concentration that results in 50% inhibition of the maximum binding (IC50) was calculated.

Conjugation and ^{111}In-labeling of control human IgG

Human IgG (Sanquin) conjugation and labeling were performed according to Ruegg et al.[21] Briefly, IgG was first conjugated to the bifunctional conjugating agent 2-(4-Isothiocyanatobenzyl)-diethylenetriaminepentaacetic acid (*p*-SCN-Bn-DTPA; Macrocyclics). After conjugation, the product was purified by

ultracentrifugation using a 30 kDa Vivaspin-2 and stored at -20 °C. Conjugated human IgG was radiolabeled with $^{111}InCl_3$ (Covidien) on the day of use.

Animal studies

In vivo imaging and biodistribution experiments were conducted using male athymic mice (BALB/cOlaHsd nude; Harlan). All experiments were approved by the animal ethics committee of the University of Groningen. Tumor cell inoculation and imaging was performed with isofluran inhalation anesthesia (induction 3%, maintenance 1.5%).

For the CHO xenograft model, mice were injected subcutaneously with 2 x 10^6 CHO-Cl2 or CHO-Cl11S cells suspended in Hank's Buffered Salt Solution (HBSS; Invitrogen). ^{89}Zr-fresolimumab (5 MBq; 10, 50 or 100 μg) and ^{111}In-IgG (3 MBq; 10, 50 or 100 μg) were administered via the penile vein. For the MDA-MB-231 xenograft model, mice were injected subcutaneously with 2 x 10^6 MDA-MB-231 cells mixed equally with Matrigel™ (BD Bioscience). ^{89}Zr-fresolimumab (5 MBq; 10 μg) and ^{111}In-IgG (3 MBq; 10 μg) were administered via the penile vein. For the MDA-MB-231 metastatic model, mice were injected intracardially (left ventricle) with 10^5 MDA-MB-231-SCP2luc cells suspended in PBS. Metastatic tumor growth was measured twice weekly with bioluminescence imaging (BLI). BLI was performed for 30-45 min after intraperitoneal administration of 150 mg/kg D-luciferin with an IVIS100 (Xenogen). When metastatic tumor growth was measurable, approximately 2-4 weeks after inoculation, ^{89}Zr-fresolimumab (5 MBq; 10 μg) and ^{111}In-IgG (3 MBq; 10 μg) were administered via the penile vein.

All animals were imaged using a microPET Focus 220 rodent scanner (CTI Siemens) and subsequent microCT imaging using a MicroCAT II (CTI Siemens). Static images of 15-45 min acquisition time were obtained at 24, 72 and 144 h postinjection. After image reconstruction, *in vivo* quantification was performed with AMIDE Medical Image Data Examiner software (version 0.9.1, Stanford University)[22] and tumor accumulation was calculated as Standardized Uptake Value (SUV). Animals were sacrificed after the last scan and organs were excised, rinsed for residual blood, weighed and counted for radioactivity. Tissue activity was expressed as percentage injected dose per gram tissue (%ID/g). Subsequently, organs of interest were split and partly formalin fixed and paraffin embedded for histological analysis and partly stored at -80 °C for *ex vivo* TGF-β1 measurement.

Ex vivo analyses on organ of interest tissue

Ex vivo TGF-β1 measurement was performed in organs of interest using an enzyme-linked immuno sorbent assay (ELISA; R&D Systems) according to the manufacturers' protocol. This ELISA measures active TGF-β1 quantitatively and latent TGF-β1 was measured after activation by acidification to discriminate between latent and active TGF-β1. Measurement of TGF-β1 was performed because CHO cells were transfected with this isoform. Formalin-fixed, paraffin-embedded organs of interest were stained with hematoxylin and eosin (H&E) and for phospho-Smad2 (Cell Signaling). Staining for phospho-Smad2 (pSmad2) served as a surrogate for active TGF-β, since it is currently not possible to stain for active TGF-β itself.

Statistical analysis

Data are presented as mean ± standard deviation (SD) from at least three individual experiments/animals, unless stated otherwise. Statistical analysis was performed using the Mann-Whitney test for non-parametric data and the unpaired T-test for parametric data. A P value ≤ 0.05 was considered significant.

RESULTS

^{89}Zr-fresolimumab labeling and quality control

HPLC analysis showed an aggregation of 1.4 ± 1.1% after conjugation of fresolimumab with sucDf-TFP and an effective conjugation of 62 ± 9%. N-sucDf-fresolimumab could be labeled with ^{89}Zr to a specific activity of up to 1000 MBq/mg with a radiochemical purity of 97.0 ± 1.2% over all experiments, not requiring further purification. A typical representative HPLC analysis of ^{89}Zr-fresolimumab is shown in Fig. 1A.

^{89}Zr-fresolimumab was highly stable in solution (0.9% NaCl) at 4 ^{0}C and in human serum at 37 ^{0}C over > 168 h. Average decrease in radiochemical purity of ^{89}Zr-fresolimumab per day in human serum at 37 ^{0}C was 0.44 ± 0.13, 0.84 ± 0.11 and 1.21 ± 0.09% for a specific activity of 250, 500 and 1000 MBq, respectively. Average decrease in radiochemical purity of ^{89}Zr-fresolimumab per day in solution (0.9% NaCl) at 4 ^{0}C was 0.42 ± 0.05%.

To proof that labeling fresolimumab did not alter the activity of fresolimumab, a competitive binding experiment was performed with unlabeled fresolimumab in competition with ^{89}Zr-fresolimumab. This resulted in an average IC50 of 18 nM fresolimumab (95% confidence interval of 12-28 nM) for the competition of TGF-β3 binding of 14 nM ^{89}Zr-fresolimumab, indicating fully preserved immunoreactivity (Fig. 1B).

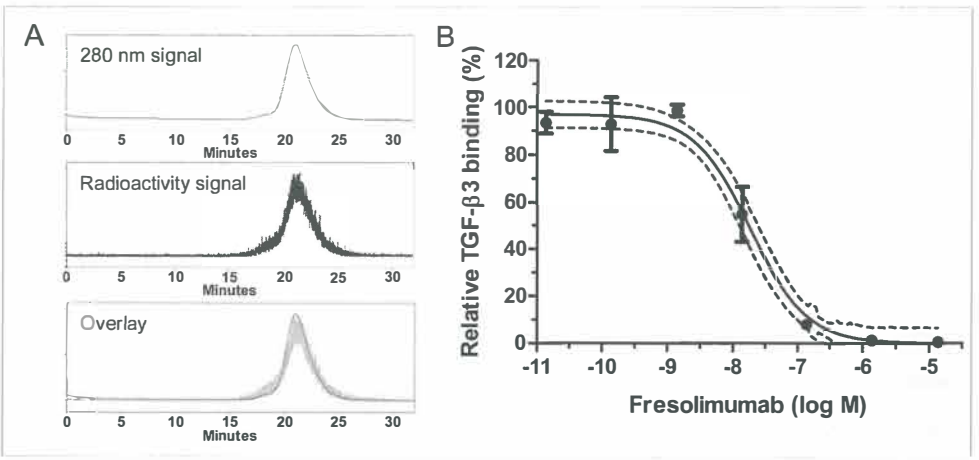

Figure 1. Quality control of ^{89}Zr-fresolimumab. Panel A shows a typical HPLC of ^{89}Zr-fresolimumab with detection at 280 nm for the protein signal and co-registration of radioactive signal. Immunoreactivity of ^{89}Zr-fresolimumab was determined in a competitive binding assay with unlabeled fresolimumab. Competition curve (with 95% confidence interval) for the binding of ^{89}Zr-fresolimumab to TGF-β3 is shown in B.

^{89}Zr-fresolimumab μPET imaging and biodistribution in CHO xenografts

^{89}Zr-fresolimumab μPET imaging was first performed on mice harboring xenograft tumors with CHO clones expressing intermediate and high levels of human latent TGF-β1. Assessment of *in vitro* expression of human latent TGF-β1 in culture media samples with ELISA confirmed the intermediate and high expression of CHO-Cl11S and CHO-Cl2, respectively (data not shown). μPET imaging of mice bearing CHO-Cl11S and CHO-Cl2 tumors with ^{89}Zr-fresolimumab indicated clear tumor accumulation and visualization in both models at 72 and 144 h postinjection, with a slightly higher tumor uptake at 144 h postinjection (Fig. 2A and 2C). No visual difference in ^{89}Zr-fresolimumab tumor uptake between both CHO clones could be detected and also quantification of the tumor uptake as assessed by SUV did not show a difference: SUV in CHO-Cl2

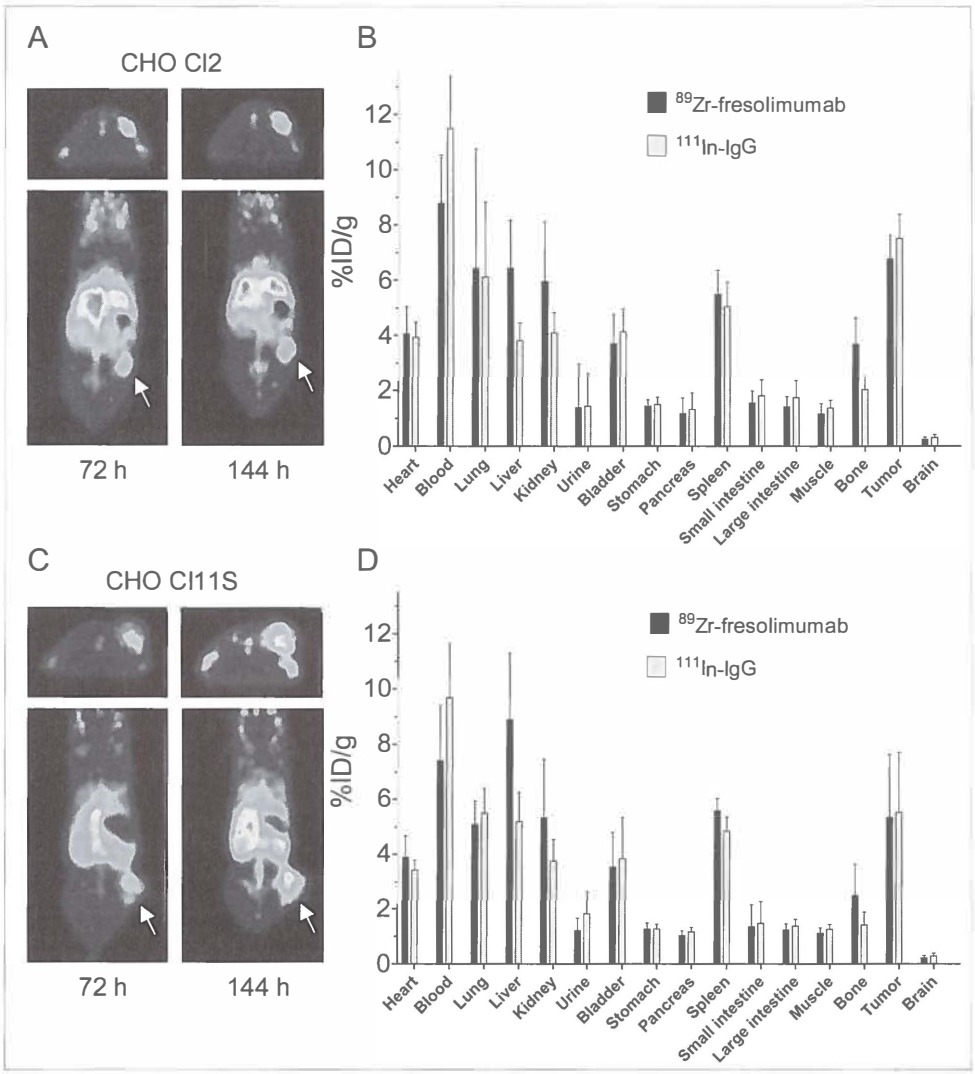

Figure 2. μPET imaging with ^{89}Zr-fresolimumab showed tumor uptake in both CHO-Cl11S and CHO-Cl2 (A and C; arrow indicates tumor). Tumor uptake and organ distribution of ^{89}Zr-fresolimumab and control ^{111}In-IgG as was quantified *ex vivo* (B and D). See page 172 for full color image.

was 2.0 ± 0.1 and 2.3 ± 0.2 at 72 and 144 h postinjection, respectively, and SUV in CHO-Cl11S was 2.0 ± 0.4 and 2.2 ± 0.6 at 72 and 144 h postinjection, respectively. *Ex vivo* analysis of ^{89}Zr-fresolimumab and ^{111}In-IgG biodistribution indicated similar uptake of both tracers in all tumors and comparable distribution over most organs (Fig. 2B and 2D). Organ uptake of ^{89}Zr-fresolimumab was higher than ^{111}In-IgG in liver and bone of both groups of mice. Subgroup analysis of the

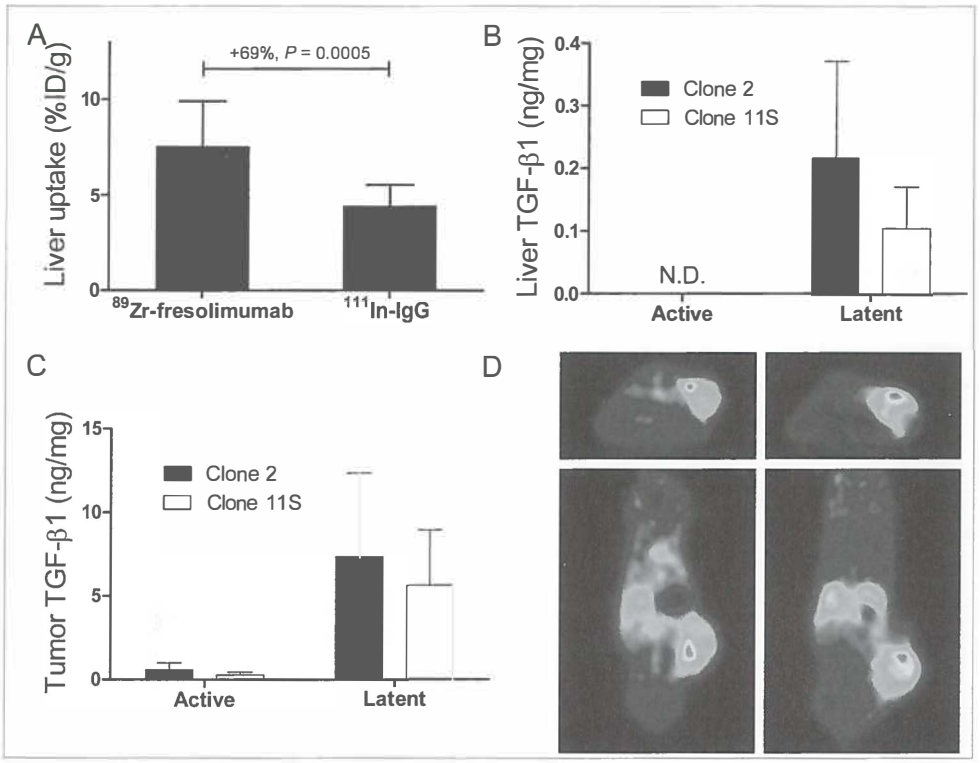

Figure 3. Liver uptake of ^{89}Zr-fresolimumab and ^{111}In-IgG in CHO xenograft mice (A). TGF-β1 levels were determined by ELISA in homogenates of liver (B) and tumor (C) tissue. Two mice with a skin ulceration at the tumor site showed locally increased uptake of ^{89}Zr-fresolimumab (represented by red areas) at the site of ulceration (D). See page 173 for full color image.

different protein doses of ^{89}Zr-fresolimumab showed similar tumor uptake of 10, 50 or 100 μg ^{89}Zr-fresolimumab, with a non-significant trend towards lower liver uptake in the 10 μg dose group (Table 1). Only in the 10 μg group there was a 92 ± 28% higher uptake of ^{89}Zr-fresolimumab than ^{111}In-IgG in kidneys (P = 0.0079). Liver uptake of ^{89}Zr-fresolimumab was 7.6 ± 2.4 %ID/g and was higher than ^{111}In-IgG in all individual mice with a mean difference of 69 ± 28% (P = 0.0005; Fig. 3A). To assess whether this was caused by high TGF-β levels in the liver, we determined TGF-β1 levels in liver homogenates with ELISA. Levels of active TGF-β1 were below the detection limit in all samples and levels of latent TGF-β1 were 0.22 ± 0.16 and 0.10 ± 0.07 ng/mg protein in livers of mice with CHO-Cl2 and CHO-Cl11S xenografts, respectively (Fig. 3B). TGF-β1 levels in tumor homogenates also showed the same pattern of higher levels in tissue from CHO-Cl2 xenografts compared to CHO-Cl11S xenografts, although not significant (Fig.

3C). The highest TGF-β1 levels were found in homogenates of tumors in two mice with skin ulceration at the tumor site. These tumors showed a focally increased ^{89}Zr-fresolimumab uptake at the site of ulceration with μPET imaging (Fig. 3D). This correlated with TGF-β1 levels in homogenates of the ulcerations of 26 and 21 ng latent TGF-β1/mg protein, which were the highest levels of all tissue samples measured (highest latent TGF-β1 level in tumors without ulcerations was 17 ng/mg). High ^{89}Zr-fresolimumab uptake was also present in sites with scar tissue in two mice that were victimized by their dominant congener cage mate prior to ^{89}Zr-fresolimumab injection (data not shown).

Table 1. Dose escalation of ^{89}Zr-fresolimumab and control ^{111}In-IgG.

	10 μg (*n* = 5)		50 μg (*n* = 2)		100 μg (*n* = 6)	
	^{89}Zr-fres*	^{111}In-IgG	^{89}Zr-fres*	^{111}In-IgG	^{89}Zr-fres*	^{111}In-IgG
Heart	3.47 ± 0.59	3.61 ± 0.57	3.53 ± 0.54	3.88 ± 0.63	4.58 ± 0.66	3.72 ± 0.37
Blood	8.23 ± 1.47	10.71 ± 1.93	9.03 ± 2.32	12.29 ± 2.40	7.79 ± 1.84	10.07 ± 1.50
Lung	7.76 ± 3.98	7.27 ± 2.10	4.99 ± 1.31	5.55 ± 1.14	4.46 ± 1.12	4.72 ± 1.05
Liver	6.31 ± 1.71	4.27 ± 0.96	6.69 ± 1.12	3.49 ± 0.09	8.91 ± 2.21	4.93 ± 1.00
Kidney	8.10 ± 0.75	4.32 ± 0.80	4.37 ± 0.18	3.45 ± 0.40	4.08 ± 0.38	3.79 ± 0.54
Urine	1.91 ± 1.55	1.82 ± 1.16	0.68 ± 0.05	0.94 ± 0.09	1.01 ± 0.41	1.65 ± 0.87
Bladder	4.23 ± 1.15	4.83 ± 0.90	3.16 ± 0.64	3.80 ± 0.71	3.29 ± 0.83	3.39 ± 0.89
Stomach	1.40 ± 0.28	1.47 ± 0.32	1.17 ± 0.05	1.18 ± 0.03	1.39 ± 0.16	1.39 ± 0.12
Pancreas	0.96 ± 0.52	1.08 ± 0.57	1.37 ± 0.36	1.54 ± 0.31	1.14 ± 0.20	1.29 ± 0.19
Spleen	5.22 ± 0.65	5.02 ± 0.71	5.43 ± 0.87	4.88 ± 1.02	5.83 ± 0.39	4.93 ± 0.47
Small intestine	1.38 ± 0.52	1.58 ± 0.71	1.38 ± 0.30	1.57 ± 0.31	1.55 ± 0.66	1.73 ± 0.66
Large intestine	1.48 ± 0.35	1.84 ± 0.58	1.39 ± 0.08	1.63 ± 0.05	1.17 ± 0.21	1.33 ± 0.26
Muscle	1.14 ± 0.40	1.34 ± 0.31	0.98 ± 0.04	1.27 ± 0.05	1.18 ± 0.14	1.31 ± 0.18
Bone	4.05 ± 0.77	2.04 ± 0.39	3.50 ± 0.42	1.75 ± 0.48	2.28 ± 0.81	1.50 ± 0.53
Tumor	5.64 ± 1.80	6.22 ± 2.17	5.99 ± 0.24	7.05 ± 0.71	6.56 ± 1.75	6.76 ± 1.58
Brain	0.23 ± 0.08	0.30 ± 0.10	0.21 ± 0.04	0.26 ± 0.04	0.25 ± 0.09	0.32 ± 0.10

Data are expressed as percentage of injected dose per gram tissue (mean ± SD). * ^{89}Zr-fresolimumab is abbreviated as ^{89}Zr-fres.

Histological analysis of CHO xenograft tumors and livers

H&E staining showed no obvious difference in morphology between tumors from xenografts of either of the CHO clones (Fig 4). All tumors largely consisted of vital vascularized tissue with tumor and stromal cells, and minor areas of necrosis. H&E staining of livers from CHO xenograft mice showed a normal morphology. All tested samples showed nuclear staining for pSmad2. Concurring with the μPET data, there was no difference in pSmad2 staining in tumors and livers from xenograft mice of both CHO clones, although liver tissue showed a more intense staining than the CHO tumors.

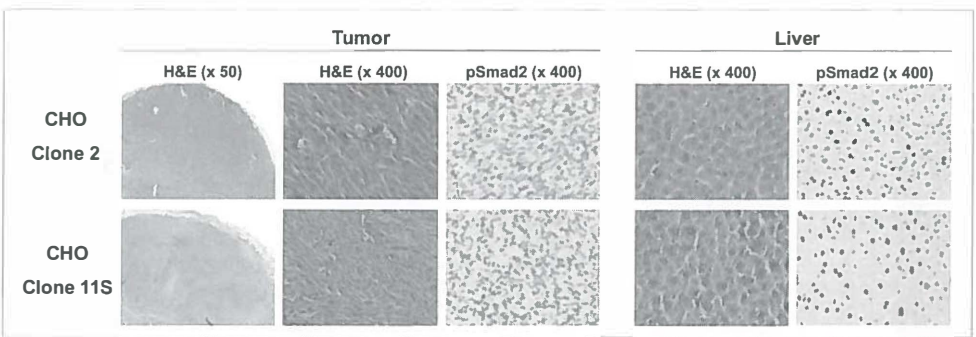

Figure 4. Histological and immunohistochemical staining for hematoxylin and eosin (H&E) and phospho-Smad2 (pSmad2) on tumor and liver material from CHO xenograft mice. See page 173 for full color image.

^{89}Zr-fresolimumab μPET imaging and biodistribution in MDA-MB-231 xenografts

To further investigate the organ and tumor distribution of ^{89}Zr-fresolimumab we used the MDA-MB-231 human breast cancer xenograft model. μPET imaging showed a clear ^{89}Zr-fresolimumab tumor accumulation over time (Fig. 5A). Tumor accumulation was also shown by SUV quantification: 1.5 ± 0.2, 2.3 ± 0.3 and 2.6 ± 0.3 at 24, 72 and 144 h postinjection, respectively. *Ex vivo* biodistribution analysis again showed a similar tumor uptake of non-specific control ^{111}In-IgG at 144 h postinjection (Fig. 5B). Organ uptake of ^{89}Zr-fresolimumab was higher than ^{111}In-IgG in liver (P = 0.0459), kidneys (P = 0.0078) and bone (P = 0.0007) and reflected the biodistribution seen in CHO xenografts.

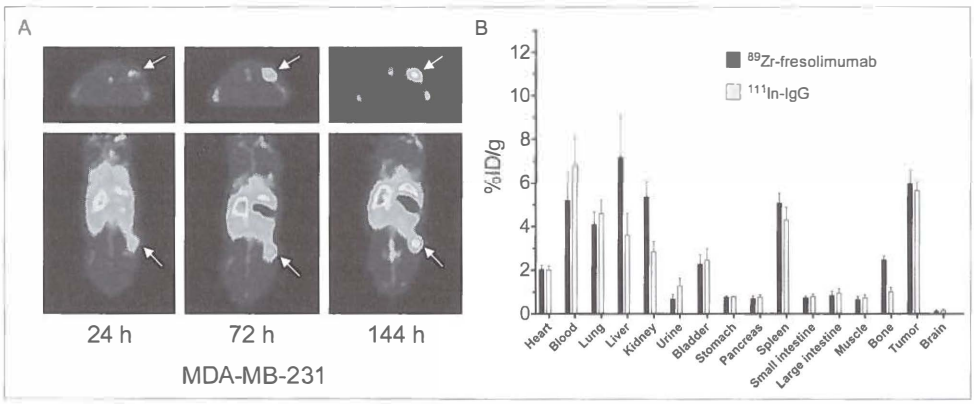

Figure 5. μPET imaging (A) and *ex vivo* biodistribution at 144 h postinjection (B) of ^{89}Zr-fresolimumab in MDA-MB-231 xenografts. See page 174 for full color image.

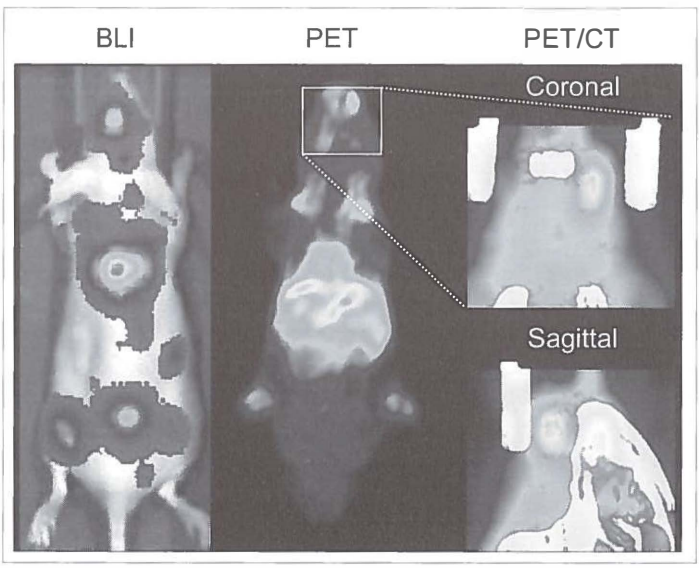

Figure 6. Representative example of bioluminescence (BLI) and μPET/CT imaging of a mouse in which bone metastatic MDA-MB-231-SCP2-luc cells were injected into the left ventricle of the heart in a disseminated model of metastasis. Metastases were visible with BLI in the jaws, skull, sternum, spine, shoulders, hips and lower limbs. See page 174 for full color image.

^{89}Zr-fresolimumab μPET imaging and biodistribution in MDA-MB-231-SCP2luc metastatic model

Because TGF-β is involved in breast cancer metastasis,[13;14] we evaluated ^{89}Zr-fresolimumab imaging in a metastatic breast cancer model as well. All mice had developed multiple (bone) metastases 3-5 weeks after intracardiac injection of MDA-MB-231-SCP2luc cells, as was visualized with bioluminescence imaging (Fig. 6), corresponding with results from others with this model.[19] Metastases were mainly localized in jaws, skull, sternum, spine, shoulders, hips and lower

limbs. Both μCT and ^{89}Zr-fresolimumab μPET imaging did not visualize any of the metastases detected by bioluminescence imaging. Only one mouse showed ^{89}Zr-fresolimumab uptake at a site suspicious for metastasis (Fig. 6). *Ex vivo* ^{89}Zr-fresolimumab biodistribution was similar as was found in CHO and MDA-MB-231 xenograft models with high liver uptake of ^{89}Zr-fresolimumab (data not shown). No toxicity of ^{89}Zr-fresolimumab was seen in any of these mice.

DISCUSSION

In the present study, we describe for the first time the development, quality control and preclinical validation of ^{89}Zr-fresolimumab for non-invasive PET imaging of tumor and organ distribution of fresolimumab.

Development and quality control of ^{89}Zr-fresolimumab provided similar results as we had seen earlier with the ^{89}Zr labeling of antibodies directed at other targets,[17;23] indicating the robustness of this labeling method. μPET imaging with ^{89}Zr-fresolimumab showed tumor uptake in CHO xenografts and in MDA-MD-231 xenografts. Remarkably high ^{89}Zr-fresolimumab uptake was seen in sites of tumor ulceration in two mice and in scar tissue of two other mice, processes in which TGF-β is involved.[24]

Our study showed for ^{89}Zr-fresolimumab a distribution comparable to ^{111}In-IgG in most organs, except for a higher uptake in liver and kidneys. This increased uptake in non-tumor organs was not seen previously with vascular endothelial growth factor (VEGF) directed ^{89}Zr-bevacizumab and human epidermal growth factor receptor-2 (HER2) directed ^{89}Zr-trastuzumab.[17;23] ^{89}Zr-fresolimumab liver uptake was especially increased when higher fresolimumab doses were used. The higher ^{89}Zr-fresolimumab kidney uptake was only seen in the low dose ^{89}Zr-fresolimumab group of 10 μg. High liver uptake of ^{89}Zr-fresolimumab likely is the result of a specific, TGF-β driven, interaction between ^{89}Zr-fresolimumab and TGF-β in the liver and would thus indicate high levels of active TGF-β in the liver. Our analysis of liver homogenates did not show high levels of the active TGF-β1 form. However, immunohistochemical staining for pSmad2 of liver tissues indicated that active TGF-β was present in the liver within hours before tissue collection.[25] This presence of active TGF-β has probably caused the accumulation of ^{89}Zr-fresolimumab in the liver and can be the consequence of rapid hepatic clearance of active TGF-β from the circulation and subsequent lysosomal degradation.[26] This might mean that human TGF-β from CHO or MDA-MD-231 tumors will upon activation be rapidly cleared by the liver, where

it accumulates, is recognized by ^{89}Zr-fresolimumab, and results in ^{89}Zr-fresolimumab accumulation in the liver. In addition to tumor derived human TGF-β, activated mouse TGF-β from non-tumor origin likely will accumulate in the liver and result in high ^{89}Zr-fresolimumab liver uptake, since fresolimumab also binds to mouse TGF-β with high affinity. Another reason for the high liver uptake might be complex formation of ^{89}Zr-fresolimumab with active TGF-β in the tumor micro-environment and in the circulation, subsequently followed by hepatic clearance of this complex. All together, this indicates a TGF-β specific biodistribution of ^{89}Zr-fresolimumab. Additionally, the high ^{89}Zr-fresolimumab liver uptake also matches strikingly the available preclinical data on the biodistribution of ^{111}In-decorin. Decorin, a small proteoglycan from the extracellular matrix, binds TGF-β with high affinity. Intravenous injection of ^{111}In-decorin into mice showed rapid hepatic clearance, especially by accumulation in nonparenchymal cells.[27] The high liver uptake of ^{89}Zr-fresolimumab reported in this preclinical study indicates the relevance of clinical ^{89}Zr-fresolimumab imaging studies to explore not only fresolimumab tumor uptake but also its organ distribution. Increased kidney uptake of ^{89}Zr-fresolimumab likely is not the representation of ^{89}Zr-fresolimumab uptake caused by high TGF-β kidney levels, but uptake of ^{89}Zr-fresolimumab catabolites from hepatic processing. Hepatic processing is often saturable and thus dose-dependent, thereby explaining that increased kidney uptake of ^{89}Zr-fresolimumab catabolites was only seen in the lowest ^{89}Zr-fresolimumab dose of 10 μg. The high bone uptake of ^{89}Zr-fresolimumab, compared to ^{111}In-IgG, can be the result of high TGF-β levels in bone.[28] However, we cannot exclude that this is an artefact due to bone uptake of dissociated ^{89}Zr since we have also seen higher bone uptake of ^{89}Zr-bevacizumab when compared with ^{111}In-bevacizumab.[17]

To study specificity of ^{89}Zr-fresolimumab, tumor uptake results were compared with ^{111}In-IgG. This showed that tumor uptake of ^{89}Zr-fresolimumab was similar to ^{111}In-IgG tumor uptake. Lack of specific, i.e. TGF-β driven, tumor uptake of ^{89}Zr-fresolimumab in our models could be a consequence of the fact that fresolimumab binds selectively to the active form of TGF-β. Our ELISA analysis of TGF-β1 levels in tumor homogenates, as well as clinical ELISA data on tumor homogenates of gastric cancer patients,[29] show that more than 90% of total TGF-β is present in its latent form, leaving little antigen for fresolimumab binding. Our CHO models were generated to produce latent TGF-β1, since this would be more resembling natural conditions than cells that produce active TGF-β1 because all normal and tumor cells only produce TGF-β in its latent form. However, specific

accumulation of ^{89}Zr-fresolimumab requires local activation of TGF-β1 in the tumor, and not all TGF-β activating mechanisms necessarily result in the release of free active TGF-β.[30] Additional to the low levels of free active TGF-β, also the biological half-life of active TGF-β is with 2-3 min much shorter than that of latent TGF-β (110 min),[31] making imaging of TGF-β with an antibody recognizing only the active form even more challenging. Obviously, this does not exclude the therapeutic potential of fresolimumab. Our imaging data clearly show tumor accumulation of fresolimumab, likely because of the enhanced permeability and retention effect,[32] indicating that fresolimumab reaches the target site in high concentrations (6.1 ± 1.6 % of injected dose per gram tumor over all mice). Presence of fresolimumab in the tumor microenvironment inhibits local activation of latent TGF-β, thereby reducing the stimulatory response of the tumor. Therefore, the amount of fresolimumab in the tumor, as visualized and quantified with ^{89}Zr-fresolimumab PET, could be a predictor for outcome.

With respect to absence of specific preferential tumor uptake of ^{89}Zr-fresolimumab, this tracer differed from other targeted antibody based tracers we developed. During imaging of other soluble tumor targets, such as VEGF, we found a 2-fold higher uptake of ^{89}Zr-bevacizumab in SKOV-3 xenografts versus control IgG.[17] With ^{89}Zr-trastuzumab HER2 imaging in the same model, tumor uptake of ^{89}Zr-trastuzumab was 5-fold higher than control IgG.[33] However we also now know that preclinical results can underestimate clinical findings, since with clinical imaging studies, we found with ^{89}Zr-bevacizumab a higher tumor uptake than with ^{89}Zr-trastuzumab.[18;34] These superior differential results in the clinical setting may prove to be the case for ^{89}Zr-fresolimumab as well. This therefore supports further pursuing of TGF-β specific clinical imaging. Furthermore, the lack of ^{89}Zr-fresolimumab visualization of metastases in our model of breast cancer bone metastases is likely caused by the sub-resolution size (< 2 mm) for μPET imaging of these lesions. This further illustrates the potentials of clinical evaluation of ^{89}Zr-fresolimumab for a complete understanding of fresolimumab distribution in cancer patients, and to address the value of fresolimumab in the treatment of (metastatic) cancer. The clear visualization of tumor ulcerations with ^{89}Zr-fresolimumab, together with the high levels of TGF-β1 we measured with ELISA in these ulcerations, encourages the further investigation of the use of fresolimumab in inflammatory diseases like pulmonary fibrosis.

In summary, ^{89}Zr-fresolimumab μPET was shown to be preclinically feasible for imaging and quantification of fresolimumab tumor uptake and organ distribution. ^{89}Zr-fresolimumab PET is ready for clinical evaluation and might contribute to the clinical development of fresolimumab. We will use this technique to quantify the tumor uptake of fresolimumab in patients with high grade gliomas.

Conflict of interest statement

RCG is employee of Genzyme Corporation.

Acknowledgments

Authors would like to thank Guus van Dongen at the VU University Medical Center Amsterdam for providing N-sucDf-TFP. Supported by grants 2007-3739, 2009-4273 and 2010-4739 of the Dutch Cancer Society.

References

1. Massague J. TGFbeta in cancer. Cell. 2008;134:215-230.
2. Markowitz SD, Roberts AB. Tumor suppressor activity of the TGF-beta pathway in human cancers. Cytokine Growth Factor Rev. 1996;7:93-102.
3. Moutsopoulos NM, Wen J, Wahl SM. TGF-beta and tumors-an ill-fated alliance. Curr Opin Immunol. 2008;20:234-240.
4. Stover DG, Bierie B, Moses HL. A delicate balance: TGF-beta and the tumor microenvironment. J Cell Biochem. 2007;101:851-861.
5. Reiss M, Barcellos-Hoff MH. Transforming growth factor-beta in breast cancer: a working hypothesis. Breast Cancer Res Treat. 1997;45:81-95.
6. Khalil N. TGF-beta: from latent to active. Microbes Infect. 1999;15:1255-1263.
7. Annes JP, Munger JS, Rifkin DB. Making sense of latent TGFbeta activation. J Cell Sci. 2003;116:217-224.
8. Wick W, Naumann U, Weller M. Transforming growth factor-beta: a molecular target for the future therapy of glioblastoma. Curr Pharm Des. 2006;12:341-349.
9. Korpal M, Kang Y. Targeting the transforming growth factor-beta signalling pathway in metastatic cancer. Eur J Cancer. 2010;46:1232-1240.
10. Garber K. Companies waver in efforts to target transforming growth factor beta in cancer. J Natl Cancer Inst. 2009;101:1664-1667.
11. Shipitsin M, Campbell LL, Argani P, et al. Molecular definition of breast tumor heterogeneity. Cancer Cell 2007;11:259-273.
12. Bierie B, Chung CH, Parker JS, et al. Abrogation of TGF-beta signaling enhances chemokine production and correlates with prognosis in human breast cancer. J Clin Invest. 2009;119:1571-1582.
13. Giampieri S, Manning C, Hooper S, Jones L, Hill CS, Sahai E. Localized and reversible TGFbeta signalling switches breast cancer cells from cohesive to single cell motility. Nat Cell Biol. 2009;11:1287-1296.
14. Serganova I, Moroz E, Vider J, et al. Multimodality imaging of TGFbeta signaling in breast cancer metastases. FASEB J. 2009;23:2662-2672.
15. Korpal M, Yan J, Lu X, Xu S, Lerit DA, Kang Y. Imaging transforming growth factor-beta signaling dynamics and therapeutic response in breast cancer bone metastasis. Nat Med. 2009;15:960-966.
16. Morris JC, Shapiro GI, Tan AR, et al. Phase I/II study of GC1008: A human anti-transforming growth factor-beta (TGFß) monoclonal antibody (MAb) in patients with advanced malignant melanoma (MM) or renal cell carcinoma (RCC). J Clin Oncol 2008;26 suppl:abstr 9028
17. Nagengast WB, de Vries EG, Hospers GA, et al. In vivo VEGF imaging with radiolabeled bevacizumab in a human ovarian tumor xenograft. J Nucl Med. 2007;48:1313-1319.

18. Oosting SF, Nagengast WB, Oude Munnink TH, et al. ^{89}Zr-bevacizumab PET imaging in renal cell carcinoma patients: feasibility of tumor VEGF quantification. EORTC-NCI-AACR meeting abstracts 2010, #221.
19. Minn AJ, Kang Y, Serganova I, et al. Distinct organ-specific metastatic potential of individual breast cancer cells and primary tumors. J Clin Invest. 2005;115:44-55.
20. Verel I, Visser GW, Boellaard R, Stigter-van WM, Snow GB, van Dongen GA. ^{89}Zr immuno-PET: comprehensive procedures for the production of 89Zr-labeled monoclonal antibodies. J Nucl Med. 2003;44:1271-1281.
21. Ruegg CL, Anderson-Berg WT, Brechbiel MW, Mirzadeh S, Gansow OA, Strand M. Improved in vivo stability and tumor targeting of bismuth-labeled antibody. Cancer Res. 1990;50:4221-4226.
22. Loening AM, Gambhir SS. AMIDE: a free software tool for multimodality medical image analysis. Mol Imaging. 2003;2:131-137.
23. Dijkers ECF, Kosterink JG, Rademaker AP, et al. Development and characterization of clinical-grade ^{89}Zr-trastuzumab for HER2/neu ImmunoPET imaging. J Nucl Med. 2009;50:962-969.
24. Klass BR, Grobbelaar AO, Rolfe KF. Transforming growth factor beta1 signalling, wound healing and repair: a multifunctional cytokine with clinical implications for wound repair, a delicate balance. Postgrad Med J. 2009;88:9-14.
25. Lin X, Duan X, Liang YY, et al. PPM1A functions as a Smad phosphatase to terminate TGFbeta signaling. Cell 2006;125:915-928.
26. Coffey RJ, Jr., Kost LJ, Lyons RM, Moses HL, LaRusso NF. Hepatic processing of transforming growth factor beta in the rat. Uptake, metabolism, and biliary excretion. J Clin Invest. 1987;80:750-757.
27. Masuda H, Takakura Y, Hashida M. Pharmacokinetics and disposition characteristics of recombinant decorin after intravenous injection into mice. Biochim Biophys Acta. 1999;1426:420-428.
28. Hering S, Isken E, Knabbe C, Janott J, Jost C, Pommer A et al. TGFβ1 and TGFβ2 mRNA and protein expression in human bone samples. Exp Clin Endocrinol Diabetes. 2001;109:217-226.
29. Hawinkels LJ, Verspaget HW, van Duijn W, et al. Tissue level, activation and cellular localisation of TGF-beta1 and association with survival in gastric cancer patients. Br J Cancer. 2007;97:398-404.
30. Sheppard D. Integrin-mediated activation of latent transforming growth factor β. Cancer Metastasis Rev. 2005;24:395-402.
31. Wakefield LM, Winokur TS, Hollands RS, Christopherson K, Levinson AD, Sporn MB. Recombinant latent transforming growth factor beta 1 has a longer plasma half-life in rats than active transforming growth factor beta 1, and a different tissue distribution. J Clin Invest. 1990;86:1976-1984.

32. Fang J, Nakamura H, Maeda H. The EPR effect: Unique features of tumor blood vessels for drug delivery, factors involved, and limitations and augmentation of the effect. Adv Drug Deliv Rev 2011;63:136-51.
33. Oude Munnink TH, Korte MA, Nagengast WB, et al. ^{89}Zr-trastuzumab PET visualises HER2 downregulation by the HSP90 inhibitor NVP-AUY922 in a human tumour xenograft. Eur J Cancer. 2010;46:678-684.
34. Dijkers EC, Oude Munnink TH, Kosterink JG, et al. Biodistribution of (89)Zr-trastuzumab and PET Imaging of HER2-positive lesions in patients with metastatic breast cancer. Clin Pharmacol Ther. 2010;87:586-592.

Chapter 8:

Summary, general discussion and future perspectives

Summary

Currently, chemotherapeutic drugs aiming directly or indirectly at DNA damage still most often form the cornerstone of systemic cancer treatment. Meanwhile, molecular targeted drugs of a new generation are increasingly used alone or combined with chemotherapy. Tumor biology research continues to identify new molecular targets involved in uncontrolled tumor growth, invasion and metastasis. For many tumor types, multiple molecular phenotypes have been identified and the next step is translating this rapidly expanding knowledge in tumor biology into new targeted systemic treatments. Tumor growth often depends on a few dysregulated growth signaling pathways and identifying this 'tumor Achilles heel' might reveal the most relevant target for systemic therapy. Among the numerous drugs that target relevant pathways are drugs targeting human epidermal growth factor receptor-2 (HER2), the pro-angiogenic vascular endothelial growth factor (VEGF), the molecular chaperone heat shock protein-90 (HSP90) and the pro-metastatic transforming growth factor β (TGF-β).

It is of interest to identify the best drug candidate(s) in an early phase of development, to identify the patient (sub)populations most likely to benefit and to early predict response. Therefore the development of predictive biomarkers of antitumor efficacy is of relevance. In addition, there is a need for techniques that can rapidly and precisely elucidate the pharmacokinetic and pharmacodynamic profile of new agents. Molecular imaging can potentially fulfill all these tasks and is therefore explored for its use in translating cancer science, and in the discovery, development, evaluation and implementation of targeted anticancer agents. Molecular imaging can be performed in a whole body and repetitive setting, providing information about (changes in) all organs and tumor lesions. Techniques used for molecular imaging include radionuclide imaging with positron emission tomography (PET) or single photon emission computed tomography (SPECT), magnetic resonance imaging (MRI) and optical imaging. Of these techniques, PET currently is the most suitable for whole body imaging and has the best quantification properties.

This thesis aimed at evaluating the role of molecular imaging with zirconium-89 (^{89}Zr) labeled antibodies in the guidance of targeted anticancer agents, with a focus on breast cancer.

Chapter 1 provides a concise background and outline of this thesis. In chapter 2, the current roles and future potentials of molecular imaging in the treatment of

breast cancer patients are reviewed. Data on molecular imaging of breast cancer patients for breast cancer screening, staging, restaging, response evaluation and guiding therapies are summarized. Most clinical data are gathered on the visualization of general processes such as glucose metabolism with the PET-tracer [^{18}F]fluorodeoxyglucose (FDG) and DNA synthesis with [18F]fluoro-L-thymidine (FLT). Increasingly more breast cancer specific targets are imaged such as the estrogen receptor (ER), growth factors and growth factor receptors. There is a good correlation between [^{18}F]fluoroestradiol (FES) tumor uptake on the PET scan and ER density as measured with immunohistochemistry. HER2 imaging with ^{111}In-trastuzumab SPECT showed in most patients with metastatic HER2 overexpressing disease, more lesions than seen with conventional staging procedures. ^{111}In-bevacizumab for SPECT and ^{89}Zr-bevacizumab for PET-imaging have been developed for VEGF imaging as marker for angiogenesis.

The molecular imaging data presented in this thesis, were all obtained by PET imaging with ^{89}Zr labeled antibodies or antibody fragments. In chapters 3, 4 and 5, this technique was used to monitor the molecular effects of therapies *in vivo*, aiming at a better understanding of, and therewith guiding of, these therapies. In chapters 6 and 7, PET imaging with ^{89}Zr labeled antibodies was used for monitoring the pharmacokinetics, organ distribution and tumor uptake of the labeled antibodies and to determine the feasibility of molecular imaging with these antibodies.

One of the therapies for which molecular imaging could serve as an early biomarker is HSP90 inhibition. The HSP90 inhibitor NVP-AUY922 downregulates the expression of many oncogenic HSP90 client proteins (including HER2), and inhibits angiogenesis by downregulating hypoxia inducible factor 1α (HIF-1α) resulting in decreased VEGF excretion. In chapter 3, the effect of NVP-AUY922 on HER2 expression was monitored preclinically with ^{89}Zr-trastuzumab HER2-PET imaging to explore the potentials of this technique as an early predictive biomarker to HSP90 targeted therapy. *In vitro* HER2 membrane expression in NVP-AUY922 treated HER2 positive human ovarian cancer SKOV3 cells showed profound reduction with flow cytometry (80%) and radio immuno assay with ^{89}Zr-trastuzumab (75%). *In vivo* HER2-PET imaging in SKOV3 xenograft bearing mice showed a mean reduction of 41% in ^{89}Zr-trastuzumab tumor uptake after NVP-AUY922 treatment. PET results were confirmed by *ex vivo* ^{89}Zr-trastuzumab biodistribution and HER2 immunohistochemical staining. This technique is currently evaluated in a phase II clinical trial for its role as an early biomarker for

HSP90 inhibition effect in patients with metastatic breast cancer (NCT01081600 and NCT01081613).

In chapter 4, the early anti-angiogenic tumor response after NVP-AUY922 treatment was evaluated with ^{89}Zr-bevacizumab VEGF-PET. In nude mice bearing xenografts of the human ovarian cancer cell line A2780 and its cisplatin resistant CP70 subline, ^{89}Zr-bevacizumab μPET was performed pre- and post NVP-AUY922 treatment. The results were verified with histological response and *ex vivo* tumor VEGF levels. Two weeks of NVP-AUY922 treatment decreased ^{89}Zr-bevacizumab uptake with 44% in A2780 xenografts, while tumor uptake was not affected in CP70 xenografts compared to pre-treatment values. In this setting, the same pattern was observed in A2780 and CP70 tumors for VEGF levels as measured with ELISA, and mean vessel density. These findings coincided in A2780 tumors with a reduction in the proliferation rate. ^{89}Zr-bevacizumab PET imaging results were in line with the antiangiogenic response and direct anti-tumor effects after NVP-AUY922 treatment, supporting the potential of ^{89}Zr-bevacizumab PET to monitor the antiangiogenic response of HSP90 inhibition *in vivo*.

Understanding molecular responses involved in HER2 targeted drugs may improve treatment of HER2 positive cancers. In chapter 5, the effect on HER2 tumor expression was evaluated for two drugs, namely the EGFR/HER2 tyrosine kinase inhibitor lapatinib, which inhibits EGFR/HER2 signaling and stabilizes HER2 at the cell membrane, and the EGFR/HER2 degrading HSP90 inhibitor 17AAG. Effects of lapatinib and 17AAG on survival, EGFR/HER2 expression and EGFR/HER2 signaling were analyzed *in vitro* with the human breast cancer cell line SKBR3 using cytotoxicity assay. EGFR/HER2 expression was studied with flow cytometry and Western blot was used to study EGFR/HER2 signaling. *In vitro*, lapatinib induced upregulation of EGFR (+70 %), but hardly HER2 (+19 %). 17AAG treatment lowered both EGFR (-41 %) and HER2 (-76%) expression. Interestingly EGFR/HER2 reduction by 17AAG was inhibited by lapatinib pretreatment. *In vivo*, ^{89}Zr-trastuzumab-F(ab')$_2$ tumor uptake was 32% lower following lapatinib, 34% after 17AAG and 53% by the combination. The *in vitro* ^{89}Zr-trastuzumab-F(ab')$_2$ internalization assay showed reduced HER2 internalization when the cells were treated with lapatinib (-25 %), explaining the reduced ^{89}Zr-trastuzumab-F(ab')$_2$ tumor uptake. These findings are of relevance for a rational design of combining HER2 targeted drugs, since for example the drug trastuzumab-DM1 requires internalization in order to be effective. This

HER2-PET technique can contribute to improve understanding of (non) efficacy of several combinations of HER2 targeted agents, and ultimately lead to better HER2 positive breast cancer treatment. This study also illustrates that tumor uptake of a HER2 tracer is not only dependent on HER2 expression, but also on cellular HER2 dynamics.

The clinical feasibility of HER2-PET imaging with ^{89}Zr-trastuzumab is shown in the study described in chapter 6A. This study was performed to determine the optimal conditions of ^{89}Zr-trastuzumab antibody dose and timing. HER2-positive metastatic breast cancer patients received a dose of 37 MBq ^{89}Zr-trastuzumab at 3 trastuzumab protein doses (10 or 50 mg when trastuzumab naive and 10 mg while on trastuzumab treatment) and underwent ≥ 2 PET-scans around day two and five post tracer injection. The best time point to assess ^{89}Zr-trastuzumab tumor uptake was 4-5 days postinjection. Trastuzumab naive patients required 50 mg ^{89}Zr-trastuzumab and patients on trastuzumab treatment 10 mg. Accumulation of ^{89}Zr-trastuzumab occurred in most known tumor lesions and some unknown lesions. The relative uptake values were 12.8, 4.1 and 3.5 for liver, bone and brain lesions and 5.9, 2.8, 4.0 and 0.20 in normal liver, spleen, kidneys and brain tissue. ^{89}Zr-trastuzumab PET at appropriate antibody dose allows visualization and quantification of uptake in HER2 positive lesions in metastatic breast cancer patients.

In chapter 6B, the findings with ^{89}Zr-trastuzumab HER2-PET in an exceptional patient are described. Trastuzumab clearance is known to be highly dose dependent and is increased in case of high tumor load. The patient described in this chapter had an exceptional high HER2-positive tumor load and the ^{89}Zr-trastuzumab HER2-PET scans of this patient revealed the impact of tumor load on trastuzumab pharmacokinetics. Due to the extensive HER2-positive tumor mass of liver metastases, ^{89}Zr-trastuzumab was predominantly taken up by liver metastases (48% of injected dose) and rapidly cleared from the circulation, as indicated by very low blood levels already by day 2 after tracer injection. Following a therapeutic loading dose of trastuzumab, the second tracer dose of ^{89}Zr-trastuzumab still showed high uptake in liver metastases (33% of injected dose), although lower than prior to the loading dose. In addition, more ^{89}Zr-trastuzumab was present in the blood pool and more uptake in other tumor lesions was seen. It was concluded that more trastuzumab is required to saturate lesions in case of extensive HER2-positive tumor load.

Chapter 7 describes the development and preclinical validation of PET imaging with ^{89}Zr-labeled TGF-β antibody fresolimumab. The pro-invasive and -metastatic TGF-β is a potential drug target for the treatment of cancer, especially in case of highly invasive and metastatic tumors such as glioblastomas and metastatic breast cancer. Because of the dual roles of TGF-β in cancer, proper patient selection is of crucial value and TGF-β imaging can therefore have an unprecedented role in the development of TGF-β targeted agents. Tumor uptake and organ distribution of ^{89}Zr-fresolimumab was assessed in a human TGF-β transfected chinese hamster ovary (CHO) xenograft model, a human breast cancer MDA-MB-231 xenograft and metastatic model. μPET imaging and *ex vivo* biodistribution analysis showed a ^{89}Zr-fresolimumab distribution similar to IgG to most organs, except for a higher uptake in liver and kidney. The high liver uptake of ^{89}Zr-fresolimumab (69% higher than IgG) was attributed to the fact that active TGF-β is rapidly cleared from the circulation by the liver. Liver uptake of ^{89}Zr-fresolimumab likely was the result of specific binding of ^{89}Zr-fresolimumab to active TGF-β in the liver, or of hepatic clearance of the ^{89}Zr-fresolimumab-TGF-β complex formed in the circulation. A further remarkably high ^{89}Zr-fresolimumab uptake was seen in sites of tumor ulceration and in scar tissue, processes known for their high levels of TGF-β. ^{89}Zr-fresolimumab accumulated in TGF-β transfected CHO xenograft tumors, MDA-MB-231 xenograft tumors and MDA-MB-231 metastases similar to IgG. With ELISA, both latent and active TGF-β were detected in tumor homogenates, while only latent TGF-β could be detected in liver homogenates. In this study, ^{89}Zr-fresolimumab PET imaging showed that: 1) not all specific targeted antibodies are necessarily accumulating specifically in preclinical tumor models; and 2) antibodies can specifically accumulate in non-tumor organs.

Discussion and future perspectives

Molecular imaging with radiolabeled antibodies is still not commonly used in daily clinical practice of cancer care. Its potential application portfolio is however expanding rapidly and it thereby holds promise for improving cancer management. Particularly, ^{89}Zr-antibody imaging with smart and small-scale studies aiming at maximum output has potential in this setting. The expanding number of institutions working with this technique and larger trials will define its precise place in the near future.

The work described in this thesis provides an overview of the possible integration of molecular antibody imaging in cancer drug development (see also Fig. 1).[1]

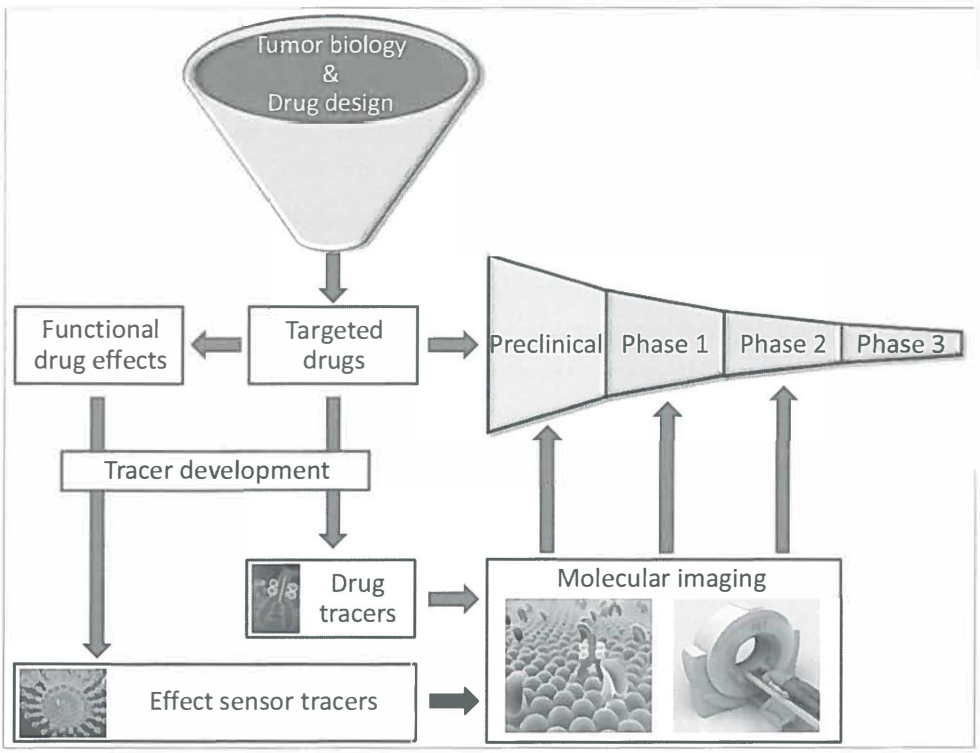

Figure 1. Flow-chart of integrating molecular imaging in drug development. See page 175 for full color image.

New insights in pharmacokinetics and tumor penetration of trastuzumab were derived from the work described in chapters 6A and 6B. This may contribute to understanding of this drug in the clinical setting. For instance, it was hitherto unknown whether antibodies could enter tumor lesions in the brain.[2] Trastuzumab was detected in only very low amounts in cerebrospinal fluid of trastuzumab treated patients with brain metastases (300-fold lower than serum levels).[3] We found ^{89}Zr-trastuzumab uptake in brain metastases to an extent comparable to the uptake in bone metastases. This observation warrants further evaluation of antibody levels in both metastatic and primary brain tumors to indicate the potential of antibody based therapies for these tumors. Secondly, we found dose and tumor load dependent pharmacokinetics of trastuzumab with

^{89}Zr-trastuzumab imaging. Antibodies do not always induce a dose limiting toxicity in dose-escalation studies. Therefore ^{89}Zr-antibody imaging can be of value in dose-finding studies with new antibodies to determine the antibody dose required to saturate the antibody target in the tumor. Likely, this will result in more rational dosing of antibodies instead of the current dosing which is often based on a patient's bodyweight.

In addition, ^{89}Zr-antibody imaging can be investigated for its use as a predictive biomarker for drug effects. Many targeted antitumor drugs have specific effects on protein expression levels in the tumor. When expression of an extracellular membrane bound or excreted protein is affected by a drug (up- or down modulation), imaging with a radiolabeled antibody targeted at this protein can be used to monitor these molecular drug effects. These molecular effects are often detected within hours after the first administration. This would potentially allow for pharmacodynamic evaluation at an early stage of treatment. The preclinical studies performed in chapters 3 and 4 with ^{89}Zr-antibody imaging of the molecular effects of the HSP90 inhibitor NVP-AUY922 are now integrated in a ongoing multicenter phase II study with NVP-AUY922.

A crucial step in the late development phase of an antitumor drug is the implementation in clinical practice. Because of the abundance of new targeted antitumor drugs, it will be impossible to test all drugs in all tumor types or as part of combinations in clinical trials. Combining targeted drugs also demands a clear preclinical mechanistic rationale for studying a given combination in a clinical trial.[4] The observations made in chapter 5 indicated that molecular imaging could potentially assist in providing this rationale for combinations of HER2 targeted drugs.

^{89}Zr-antibody imaging is also a quantitative and (relatively) easy method to study repetitively the effect of a certain drug on the tumor uptake of the labeled antibody. With preclinical small molecule imaging it was recently shown that inhibiting tumor angiogenesis results in an improved chemotherapy delivery to tumors. This effect was attributed to the normalization of the tumor vasculature.[5] However, the abnormal structure of tumor vasculature is essential for the extravasation and retention of macromolecular drugs like antibodies, known as the enhanced permeability and retention (EPR) effect.[6] It will therefore be interesting to image the influence of antiangiogenic drugs on tumor uptake of antibodies since it might well be that such a treatment results in a decreased tumor uptake of antibodies.

Another future challenge with antibody imaging is to translate the clinical know-how from nuclear antibody imaging to nonnuclear antibody imaging approaches. Nonnuclear imaging, for example with fluorescent labeled antibodies, has the advantages of absence of ionizing radiation exposure and the potential to detect smaller lesions than possible with nuclear imaging techniques. Therefore it can replace and complement nuclear imaging in settings were the risks from ionizing radiation (calculated at 18-20 millisievert for 37 MBq ^{89}Zr-antibody) are of particular relevance, such as cancer screening and non-oncological disease, or in settings where detection of small lesions is required, such as during surgery or endoscopy. It is expected that major progress will be made in the clinical translation of optical imaging with fluorescent labeled antibodies in the near future.[7] Preclinical studies with dual labeled antibodies have already shown good correlation between the nuclear and optical signal.[8] In addition, precise *ex vivo* localization of the fluorescent labeled antibody is possible with fluorescence microscopy on tumor sections.[9] Advances in technology of detection systems have now resulted in the first optical cameras for breast, intraoperative and endoscopic imaging.[9-11] By bringing the camera closer to the tumor, these techniques reduce former problems of limited tissue penetration of optical signals, and have potential in molecular imaging with fluorescent antibodies. Undoubtly, this will encourage instrumentation manufacturers, software manufacturers and physicists to develop robust optical quantification methods.

References

1. de Vries EGE, Oude Munnink TH, van Vugt MATM, Nagengast WB. Toward molecular imaging-driven drug development in oncology. Cancer Discovery 2011;1:25-28.
2. Lampson L. Monoclonal antibodies in neuro-oncology: Getting past the blood-brain barrier. MAbs 2011;3:1-8.
3. Pestalozzi BC, Brignoli S. Trastuzumab in CSF. J Clin Oncol 2000;18:2349-51.
4. Verweij J, Disis ML, Cannistra SA. Phase I studies of drug combinations. J Clin Oncol 2010;28:4545-6.
5. Escorcia FE, Henke E, McDevitt MR, et al. Selective killing of tumor neovasculature paradoxically improves chemotherapy delivery to tumors. Cancer Res 2010;70:9277-86.
6. Fang J, Nakamura H, Maeda H. The EPR effect: Unique features of tumor blood vessels for drug delivery, factors involved, and limitations and augmentation of the effect. Adv Drug Deliv Rev 2011;63:136-51.
7. Pysz MA, Gambhir SS, Willmann JK. Molecular imaging: current status and emerging strategies. Clin Radiol 2010;65:500-16.
8. Sampath L, Kwon S, Ke S, et al. Dual-labeled trastuzumab-based imaging agent for the detection of human epidermal growth factor receptor 2 overexpression in breast cancer. J Nucl Med 2007;48:1501-10.
9. Foersch S, Kiesslich R, Waldner MJ, et al. Molecular imaging of VEGF in gastrointestinal cancer in vivo using confocal laser endomicroscopy. Gut 2010;59:1046-55.
10. van de Ven SM, Elias SG, van den Bosch MA, Luijten P, Mali WP. Optical imaging of the breast. Cancer Imaging 2008;8:206-15.
11. Troyan SL, Kianzad V, Gibbs-Strauss SL, et al. The FLARE intraoperative near-infrared fluorescence imaging system: a first-in-human clinical trial in breast cancer sentinel lymph node mapping. Ann Surg Oncol 2009;16:2943-52.

Chapter 9:

Nederlandse samenvatting (Summary in Dutch)

Op dit moment is chemotherapie nog veelal de hoeksteen van de medicamenteuze behandeling van tumoren. In toenemende mate worden ook moleculair gerichte medicijnen van een nieuwe generatie toegepast, al dan niet gecombineerd met chemotherapie. Onderzoek naar de biologie van tumoren identificeert voortdurend nieuwe moleculaire processen die betrokken zijn bij tumorgroei en het uitzaaien van tumoren. Voor vele tumorsoorten zijn er meerdere moleculair verschillende subtypen geïdentificeerd. De volgende stap is deze vooruitgang in biologische kennis verder te vertalen naar nieuwe en betere behandelmethoden.

Aangezien tumorgroei vaak sterk afhankelijk is van slechts enkele ontregelde eigenschappen, lijkt het zinvol om de behandeling te richten op deze eigenschappen die de Achilleshiel van de tumor vormen. Inmiddels zijn er al verscheidene moleculair gerichte antikankermedicijnen beschikbaar gekomen, en daarnaast zijn er nog vele in ontwikkeling. Voorbeelden zijn medicijnen gericht op het remmen van de 'humane epidermale groeifactor receptor-2' (HER2), 'vasculaire endotheliale groeifactor' (VEGF), het chaperone eiwit 'hitteshock proteine-90' (HSP90) en 'transforming groeifactor-β' (TGF-β).

Om de ontwikkeling van en behandeling met deze nieuwe medicijnen te optimaliseren, is het van belang om in een vroege ontwikkelingsfase de meest potente middelen te kunnen selecteren. Daarnaast is er behoefte aan technieken die snel en precies het farmacokinetische en farmacodynamische profiel van een nieuw medicijn in kaart kunnen brengen. Vervolgens is het zaak om de patiënten die het meeste baat zullen hebben bij deze nieuwe medicijnen te kunnen identificeren en/of om het effect van de behandeling in een vroeg stadium vast te kunnen stellen. Hiervoor is het belangrijk om markers te vinden die het antitumor effect van een nieuw medicijn kunnen voorspellen. Moleculaire beeldvorming heeft de potentie om hieraan een belangrijke bijdrage te kunnen leveren. Deze techniek wordt daarom in toenemende mate onderzocht voor de mogelijke toepassingen bij de ontwikkeling, evaluatie en implementatie van nieuwe moleculair gerichte antikankermedicijnen. Omdat moleculaire beeldvorming meerdere malen in de tijd uitgevoerd kan worden en hiermee ook het hele lichaam afgebeeld kan worden, kan de techniek informatie verschaffen over (veranderingen in) alle organen en alle aanwezige tumorlaesies. Technieken die gebruikt kunnen worden voor moleculaire beeldvorming zijn positron emission tomography (PET), single photon emission computed tomography (SPECT), magnetic resonance imaging (MRI) en optische beeldvorming. Van deze

technieken zijn PET en SPECT momenteel het meest geschikt voor moleculaire beeldvorming van het gehele lichaam. Daarnaast kan met PET de opname van de tracer in weefsels het beste gekwantificeerd worden.

Dit proefschrift richt zich op het onderzoeken van de mogelijkheden van moleculaire beeldvorming met PET scans van zirconium-89 (^{89}Zr) gelabelde antilichamen in de ontwikkeling en implementatie van nieuwe moleculair gerichte antikankermedicijnen.

In hoofdstuk 1 wordt een korte inleiding gegeven en worden de verschillende hoofdstukken geïntroduceerd. De in dit proefschrift gepresenteerde resultaten met moleculaire beeldvorming zijn allen verkregen met PET scans van ^{89}Zr gelabelde antilichamen (of fragmenten van radioactief gelabelde antilichamen). In hoofdstukken 3, 4 en 5 is deze techniek gebruikt om het effect van nieuwe moleculair gerichte antikankermedicijnen te evalueren, om zo deze middelen beter te begrijpen en hiermee effectiever in te kunnen zetten. In hoofdstukken 6 en 7 zijn PET scans met ^{89}Zr gelabelde antilichamen gebruikt om de farmacokinetiek, orgaandistributie en tumoropname van de gelabelde antilichamen te bestuderen.

In hoofdstuk 2 wordt een uitgebreidere literatuurbeschrijving gegeven van de huidige rol en toekomstige mogelijkheden van moleculaire beeldvorming bij de behandeling van borstkanker. Studies die gekeken hebben naar het gebruik van moleculaire beeldvorming bij borstkanker voor screening, (her)stadiering, tumorresponse-evaluatie en het gebruik bij de ontwikkeling van nieuwe medicijnen, worden besproken. De meeste studies gebruikten hiervoor de visualisatie van meer algemene cellulaire processen zoals glucosemetabolisme en DNA-synthese met respectievelijk [^{18}F]fluorodeoxyglucose (FDG) en [18F]fluoro-L-thymidine (FLT) PET scans. In toenemende mate wordt moleculaire afbeelding echter ook toegepast voor het afbeelden van specifieke borstkankereiwitten, zoals de hormoonreceptoren, groeifactoren en groeifactorreceptoren.

Remmers van HSP90 vormen een nieuwe groep antikankermedicijnen, die de expressie van vele tumoreiwitten (waaronder HER2 en VEGF) verlagen. Moleculaire beeldvorming kan mogelijk gebruikt worden als een vroege voorspeller van de antitumoreffecten van HSP90 remmers. In hoofdstuk 3 is het effect van NVP-AUY922 (een HSP90 remmer) op de HER2-expressie in een humaan tumormodel gemeten met ^{89}Zr-trastuzumab HER2-PET scans. Experimenten met HER2-positieve humane borstkankercellen toonden allereerst

dat NVP-AUY922 de HER2 expressie met 80% verlaagde en hierdoor de binding van ^{89}Zr-trastuzumab aan deze cellen met 75% verlaagd werd. In het muizenmodel werd een 41% verlaagde tumoropname van ^{89}Zr-trastuzumab gezien na een korte behandeling met NVP-AUY922. Deze PET scan resultaten konden bevestigd worden met *ex vivo* analyses op de tumoren. Mede op basis van deze resultaten wordt deze techniek momenteel toegepast in een studie waarin borstkankerpatiënten behandeld worden met NVP-AUY922.

In hoofdstuk 4 is het effect van NVP-AUY922 op de bloedvatvorming (angiogenese) in HER2-negatieve modellen bekeken met ^{89}Zr-bevacizumab VEGF-PET scans. Twee weken behandelen met NVP-AUY922 verlaagde de ^{89}Zr-bevacizumab tumoropname met 44%, terwijl de opname in een resistent model niet veranderde. Deze PET resultaten werden vergeleken met *ex vivo* analyses voor VEGF-expressie, vaatdichtheid en proliferatie-index. De ^{89}Zr-bevacizumab PET scan resultaten kwamen hierbij overheen met de anti-angiogene effecten van de NVP-AUY922 behandeling. Hoofdstukken 3 en 4 tonen hiermee aan dat het effect van HSP90 remming gemeten kan worden met moleculaire beeldvorming met gelabelde antilichamen.

Door het effect op HER2 tijdens de behandeling met HER2 gerichte medicijnen te bestuderen, kan de behandeling met deze middelen mogelijk verbeterd worden. In hoofdstuk 5 is met behulp van ^{89}Zr-trastuzumab-F(ab')$_2$ PET in een diermodel het effect op de HER2-expressie in tumoren bekeken van twee verschillende medicijnen, namelijk de EGFR/HER2 tyrosinekinaseremmer lapatinib en de HSP90-remmer 17AAG. In celexperimenten werd gezien dat lapatinib de HER2-expressie licht verhoogde en dat 17AAG de HER2-expressie sterk verlaagde. Dit effect van 17AAG op de HER2-expressie kon worden tegengegaan door cellen eerst met lapatinib te behandelen. In het diermodel bleek de tumoropname van ^{89}Zr-trastuzumab-F(ab')$_2$ echter door zowel lapatinib als 17AAG af te nemen. De grootste afname werd zelfs gezien in de dieren die zowel lapatinib als 17AAG kregen. Het effect van lapatinib op de ^{89}Zr-trastuzumab-F(ab')$_2$ tumoropname kon niet verklaard worden door het effect op de HER2-expressie, zoals gezien in de celexperimenten. Daarom is vervolgens het effect van lapatinib op de internalisatie van ^{89}Zr-trastuzumab-F(ab')$_2$ nader bestudeerd. Hierbij bleek dat lapatinib de binding van ^{89}Zr-trastuzumab-F(ab')$_2$ aan de tumorcelmembraan weliswaar verhoogde, maar dat de opname van ^{89}Zr-trastuzumab-F(ab')$_2$ door de cellen geremd was. Hiermee kon de verlaagde tumoropname van ^{89}Zr-trastuzumab-F(ab')$_2$ na lapatinib behandeling verklaard worden. Deze

bevindingen tonen aan dat het signaal op HER2-scans niet alleen afhankelijk is van de expressie van HER2, maar ook van de dynamiek van HER2. Daarnaast kan deze kennis gebruikt worden om combinaties van HER2 gerichte medicijnen effectiever in te zetten, aangezien sommige middelen pas actief zijn na internalisatie door tumorcellen terwijl anderen ook actief zijn op de celmembraan.

De mogelijkheid om de HER2-PET scan met ^{89}Zr-trastuzumab in patiënten toe te passen is beschreven in hoofdstuk 6A. Deze studie werd uitgevoerd om de optimale condities (trastuzumab dosis en tijdstip van de scan) voor de ^{89}Zr-trastuzumab HER2-PET scan te bepalen. Hiervoor kregen patiënten met uitgezaaide HER2-positieve borstkanker een dosis van 10 of 50 mg ^{89}Zr-trastuzumab toegediend waarna op tenminste 2 tijdstippen (variërend van 1 tot 7 dagen na injectie) een PET scan werd gemaakt. De beste HER2-PET scans werden verkregen 4-5 dagen na injectie van ^{89}Zr-trastuzumab, omdat er op dat tijdstip een optimale balans is tussen de opname in de tumor, de hoeveelheid in het bloed en de totaal aanwezige radioactiviteit. Patiënten die al behandeld werden met trastuzumab hadden voldoende aan 10 mg ^{89}Zr-trastuzumab, maar voor patiënten die geen trastuzumab kregen was tenminste 50 mg nodig. Op de HER2-PET scans konden de meeste reeds bekende tumorlaesies worden teruggezien en daarnaast werd een aantal nieuw laesies zichtbaar. De hoogste opname van ^{89}Zr-trastuzumab werd gezien in uitzaaiingen in de lever, gevolgd door uitzaaiingen in bot- en hersenen. In organen zoals lever, nieren en milt werd ook traceropname gezien. Dit werd beschouwd als 'fysiologische' traceropname en passend bij het opname patroon van intacte radioactief gelabelde antilichamen.

In hoofdstuk 6B worden de bevindingen met ^{89}Zr-trastuzumab HER2-PET in een bijzondere patiënt beschreven. Van trastuzumab is het bekend dat de klaring sterk afhankelijk is van de dosis die de patiënt krijgt en dat de klaring versneld is bij patiënten met een grote tumormassa. De patiënt die in dit hoofdstuk beschreven wordt, had een extreem groot totaal volume aan uitzaaiingen in de lever. De ^{89}Zr-trastuzumab HER2-PET scans toonden de invloed hiervan op de farmacokinetiek van trastuzumab. Door de grote tumormassa in de lever was al twee dagen na injectie 48% van de ^{89}Zr-trastuzumab dosis opgenomen door de lever en was er vrijwel niets meer zichtbaar in het bloed. Dit in tegenstelling tot de hoge bloedconcentraties die gezien worden in patiënten met een lagere tumormassa. Nadat de behandeling met trastuzumab was gestart, werd voor de tweede keer een ^{89}Zr-trastuzumab HER2-PET scan gemaakt. Deze scan toonde aan dat, ondanks de behandeldosering, de tumormassa in de lever nog steeds een

zeer groot deel van de ^{89}Zr-trastuzumab dosis had opgenomen en dat deze tumormassa dus nog niet verzadigd was door de therapeutische dosis. Wel was er nu een hogere ^{89}Zr-trastuzumab bloedconcentratie te zien en was de ^{89}Zr-trastuzumab opname in andere tumoren verhoogd. Deze bevindingen suggereren dat de dosering van trastuzumab wellicht beter op basis van tumormassa vastgesteld kan worden, dan op basis van het lichaamsgewicht, zoals het nu gebeurt.

Hoofdstuk 7 beschrijft de ontwikkeling en preklinische validatie van het met ^{89}Zr-gelabelde TGF-β antilichaam fresolimumab. Aangezien TGF-β betrokken is bij tumor invasie en uitzaaiingen, is het een potentiëel aangrijpingspunt voor de behandeling van kanker. Maar omdat TGF-β ook een remmende invloed kan hebben op tumoren, is het van groot belang om de patiënten te kunnen identificeren die baat zouden kunnen hebben bij de behandeling met een TGF-β remmer. Het kunnen afbeelden van de tumorexpressie van TGF-β en van de tumoropname van fresolimumab zou hierbij een rol kunnen spelen. De tumoropname en orgaandistributie van ^{89}Zr-fresolimumab werd daarom getest in meerdere tumormodellen. Zowel de PET scans als de orgaananalyses toonden voor ^{89}Zr-fresolimumab een normale antilichaamdistributie, met uitzondering van een verhoogde opname in lever en nieren. De verhoogde opname in de lever werd waarschijnlijk veroorzaakt doordat TGF-β snel door de lever geklaard wordt vanuit de circulatie. Hierdoor kan ^{89}Zr-fresolimumab binden aan TGF-β in de lever. Daarnaast werd er een opmerkelijk hoge ^{89}Zr-fresolimumab opname gezien in ulcerende gebieden en in helende wonden. Dit zijn beide processen waarvan bekend is dat TGF-β er een belangrijke rol in speelt. De tumoropname van ^{89}Zr-fresolimumab was in alle modellen vergelijkbaar met die van een niet-specifiek controle antilichaam. Hierdoor kan uit deze studie geconcludeerd worden dat niet alle antilichamen een specifieke opname laten zien in preklinische tumormodellen en dat antilichamen specifiek kunnen accumuleren in andere organen dan de tumor.

Samenvattend kan worden gesteld dat moleculaire beeldvorming met radioactief gelabelde antilichamen potentie heeft om een rol te gaan spelen bij de behandeling van tumoren en bij de ontwikkeling van nieuwe behandelingen. Het onderzoek dat beschreven is in dit proefschrift kan worden gezien als een voorbeeld voor de mogelijke toepassingen van moleculaire beeldvorming met gelabelde antilichamen bij de ontwikkeling van nieuwe antikankermedicijnen.

Dankwoord

Toen ik met dit promotieonderzoek begon, werd mij gevraagd wat mij leuk leek aan het eenzame bestaan van een onderzoeker tussen 4 muren. Gelukkig bleek al snel dat er maar weinig elementen van onderzoek in eenzaamheid worden uitgevoerd en dat in 1 van de 4 muren een deur zit die toegang geeft tot de vele mensen die een bijdrage hebben geleverd aan dit onderzoek. Het was zeer inspirerend en motiverend om met een uiterst divers gezelschap aan dit onderzoek te werken, om samen na te denken over waar we nu eigenlijk naar kijken en om samen te genieten van de successen die geboekt werden. Iedereen die een bijdrage in welke vorm dan ook aan dit onderzoek heeft geleverd wil ik hier enorm voor bedanken. Daarnaast verdient een aantal personen hier een speciale vermelding.

Grote dank gaat uit naar het promotieteam bestaande uit de promotores prof. dr. E.G.E. de Vries en prof. dr. R.A.J.O. Dierckx, en de copromotores dr. M.N. Lub-de Hooge, dr. A.H. Brouwers en dr. C.P. Schröder.

Beste Liesbeth, toen ik voor het eerst naar je toe ging om te solliciteren naar deze promotieplek, was mij ingefluisterd dat ik heel goed moest weten wat ik wilde en waar ik het over had, omdat ik anders geen schijn van kans zou maken. Al voordat je me dus ooit gezien had, liet je me al nadenken en maakte je me scherp. Na onze eerste ontmoeting is deze stimulerende invloed van jou nooit verminderd. Bedankt dat je me deze kans hebt gegeven, voor je excellente begeleiding en voor de wijze waarop je me hebt opgenomen in de wetenschappelijke wereld.

Beste Rudi, zonder jou hadden we dit onderzoek nooit kunnen uitvoeren. Door jouw inzet hebben we de beschikking gehad over de beste faciliteiten die je kunt wensen voor dit type onderzoek. Het is indrukwekkend hoe je steeds in staat blijkt te zijn om de (al hoge) kwaliteit van de afdeling Nucleaire Geneeskunde en Moleculaire Beeldvorming weer naar een hoger niveau te brengen. Door je toekomstgerichte aanpak zal dit zeker nog vele vruchten afwerpen.

Beste Marjolijn, wat was het toch fijn om naast alle artsen ook een apotheker in het promotieteam te hebben. Je hebt me tot het einde aan toe enorm geholpen met je gedetailleerde kennis over zowel de farmaceutische aspecten van de labelingen, als ook over de biologische mechanismen betrokken bij de tracer opname, verdeling en uitscheiding.

Beste Adrienne, veel tijd heb je besteed aan het bekijken en uitwerken van de patiëntenscans. Vaak zaten we al binnen een uur nadat de scan was gemaakt

samen achter het scherm voor een eerste indruk. Dit waren altijd spannende en mooie momenten. Daarnaast ben je van onschatbare waarde voor het goed laten verlopen van de klinische studies.

Beste Carolien, je wetenschappelijke inzichten hebben tijdens de vele overleggen die we hadden geleid tot het opzetten van goede experimenten. Ook hebben we samen al veel nieuwe plannen gemaakt. Met veel doorzettingsvermogen is het je gelukt om een complexe patiëntenstudie op te zetten, waarin onze preklinische bevindingen nu in de kliniek worden geëvalueerd. Door je taalkundige inzicht heb je een enorme bijdrage geleverd aan de manuscripten, die elke keer zichtbaar verbeterden als ze van je terugkwamen.

Alle coauteurs veel dank voor jullie bijdrage aan niet alleen de manuscripten, maar ook aan het opzetten, uitvoeren en analyseren van de experimenten. In het bijzonder wil ik hier prof. dr. G.A.M.S. van Dongen, VUMC Amsterdam, bedanken voor de steun bij het opzetten van de ^{89}Zr scans, voor de vele nuttige discussies en voor de waardevolle inhoudelijke bijdrage aan de manuscripten.

Zonder de subsidie van KWF Kankerbestrijding (nr. 2007-3739) had dit onderzoek nooit plaats kunnen vinden en dus ben ik KWF Kankerbestrijding, de collectanten en de donateurs heel dankbaar.

Paranimfen dr. Wouter Nagengast en drs. Harry Kooiker wil ik bedanken voor alle steun. Harry, als mentor in de periode tussen m'n afstuderen en promoveren heb je veel voor me betekend en heb ik veel van je geleerd. En Wouter, zonder jou had ik nu nooit dit dankwoord hoeven schrijven. Je hebt me binnengehaald, me op gang gebracht en me verder laten groeien. Jou gedrevenheid, kennis en inzicht lijken onbegrensd en hierdoor heb je me enorm geïnspireerd tijdens de vele uren die we samen hebben besteed aan alle fasen van de experimenten.

Dr. Hetty Timmer-Bosscha, vanaf het allereerste begin tot nu ben je van grote betekenis geweest voor alle aspecten van het preklinische onderzoek dat in dit proefschrift staat beschreven. Ook de andere collega's van het "imaging dream team" wil ik graag bedanken. Silke Vedelaar, dr. Esther van Straten en Kirsten van Huisstede, zonder jullie toegewijde inzet was ik nu nog aan het pipetteren, labelen en kweken. En drs. Anton Terwisscha van Scheltinga, Marlous Arjaans, drs. Sietske Gaykema, drs. Karin Tamas, Linda Pot, drs. Michel van Kruchten en drs. Frank-Jan Warnders, bedankt voor jullie bijdragen, de vele discussies en natuurlijk de gezelligheid.

Erg veel respect wil ik uiten voor mijn kamergenoten. Jullie houden het al heel lang met me vol en zijn ook voorlopig nog niet van mij af. Ik verheug me dan ook op de tijd die we nog samen zullen doorbrengen.

Het gehele Multidisciplinair Oncologisch Laboratorium wil ik bedanken voor alle ondersteuning, en in het bijzonder dr. Coby Meijer, drs. Sander de Korte, prof. dr. Steven de Jong, prof. dr. Frank Kruyt en dr. Marcel van Vugt bedankt voor jullie bijdragen.

Mede feestcommissiegenoten bedankt voor alle 'vergaderingen' die we tijdens en na ons jaar hebben gehad.

Afdeling Medische Oncologie bedankt voor alle administratieve ondersteuning (Gretha Beuker en Bianca Smit) en voor de input tijdens de discussies over de imaging data en de patiëntenstudies (drs. Sjoukje Oosting, dr. Annemiek Walenkamp, prof. dr. Jourik Gietema en prof. dr. Geke Hospers).

Afdeling Nucleaire Geneeskunde en Moleculaire Beeldvorming bedankt voor alle technische en praktische ondersteuning bij zowel de preklinische als de klinische studies. Dr. Johan de Jong, dank voor alle hulp bij het analyseren van de scans. Jurgen Sijbesma, bedankt voor het in goede banen leiden van de μPET studies. MNW-ers, bedankt voor de zorg rond de patiëntenscans. En Klaas Willem Sietsma, bedankt voor alle computerondersteuning.

Afdeling Klinische Farmacie en Apotheek, in het bijzonder drs. Eli Dijkers, prof. dr. Jos Kosterink, dr. Hendrikus Boersma en drs. Marieke Sturkenboom, bedankt voor jullie bijdrage aan dit proefschrift en voor de samenwerking.

Beste familie en vrienden, bedankt voor al jullie steun, vertrouwen en begrip tijdens mijn promotietraject. Papa en mama, ik ben trots op jullie. Jullie hebben mij, Marloes en Jolijn een heerlijke jeugd gegeven en ons alle mogelijke steun gegeven om te komen waar we nu zijn. Bedankt.

En Marijke, jou zal ik dankbaar zijn gedurende de lange toekomst die we nog voor ons hebben.

Color figures

Chapter 2

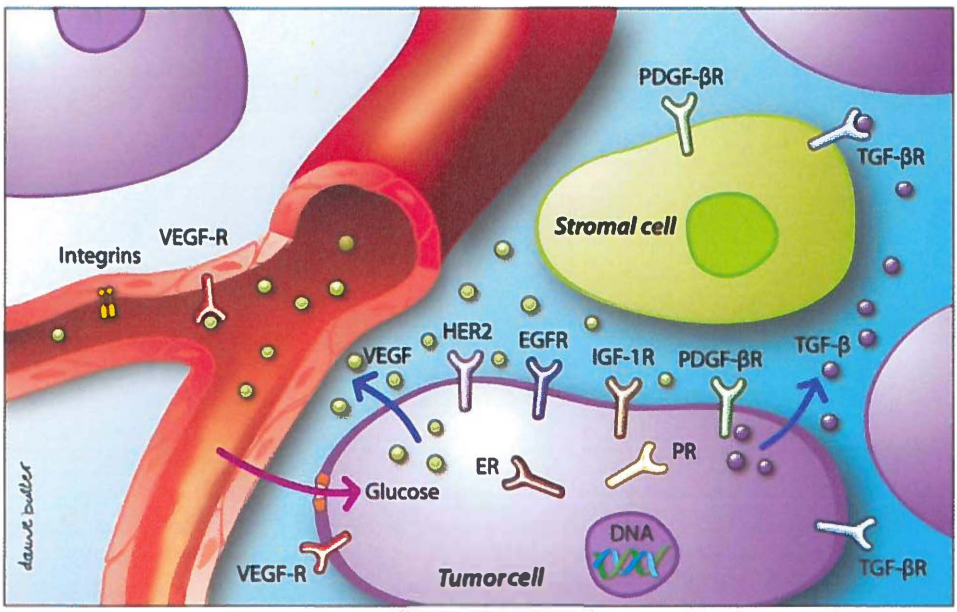

Figure 1. Schematic presentation of the (potential) targets for breast cancer molecular imaging.

Chapter 3

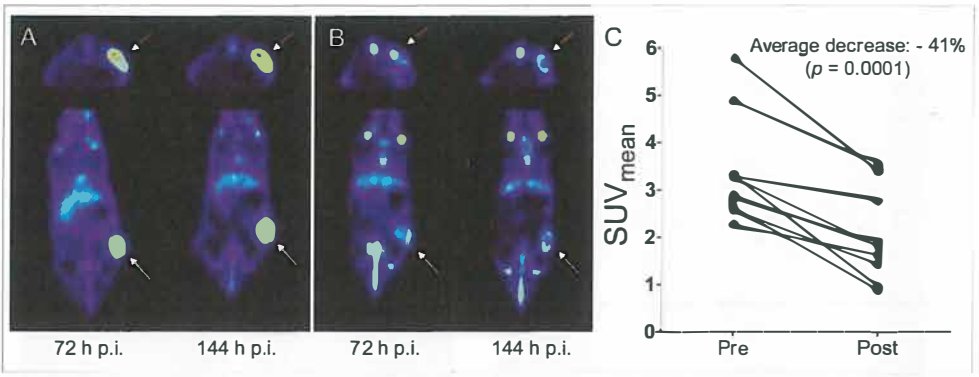

Figure 2. Transversal and coronal PET images of a representative mouse scanned with ^{89}Zr-trastuzumab before (A) and after (B) treatment with NVP-AUY922. Arrows indicate tumor. PET quantification of ^{89}Zr-trastuzumab tumor uptake at 144 h postinjection is shown in C.

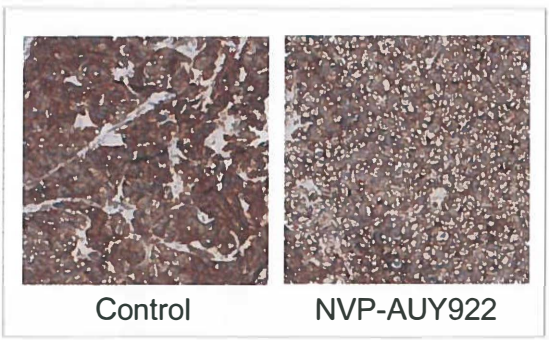

Figure 4. HER2 immunohistochemistry in representative tumors from a control and a NVP-AUY922 treated mouse. Mice were treated with NVP-AUY922 (50 mg/kg, 3qw) or control for 10 days. Tumor samples were collected 2 days after the last dose of NVP-AUY922.

Chapter 4

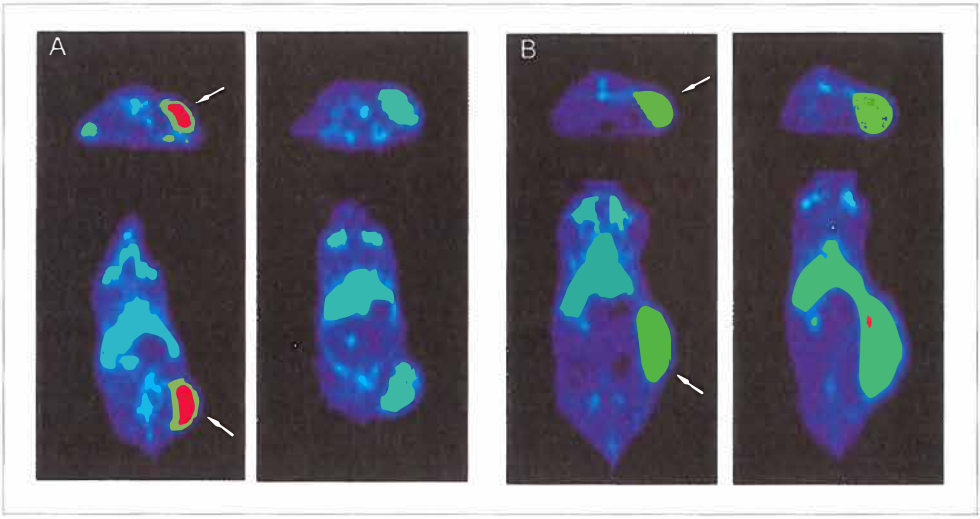

Figure 2. Representative transversal and coronal microPET images of ^{89}Zr-bevacizumab obtained before treatment of A2780 (A) and CP70 (B) xenografts (left panels), and after NVP-AUY922 treatment (right panels). Images were obtained at 144 h after injection of ^{89}Zr-bevacizumab. Tumor is indicated by arrow.

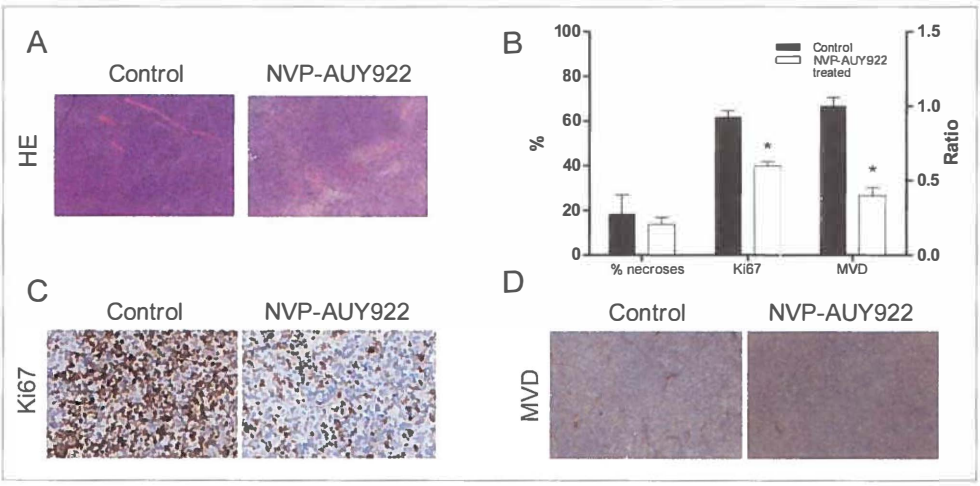

Figure 5. (A) Representative hematoxylin and eosin (HE) staining, (B) percentage necroses, Ki67 staining and MVD (right Y-axis) (* $P < 0.05$), (C) representative Ki67 staining, and (D) representative von Willebrand factor staining for MVD of control and NVP-AUY922 treated A2780 xenograft. Data are presented as mean ± SEM.

Chapter 5

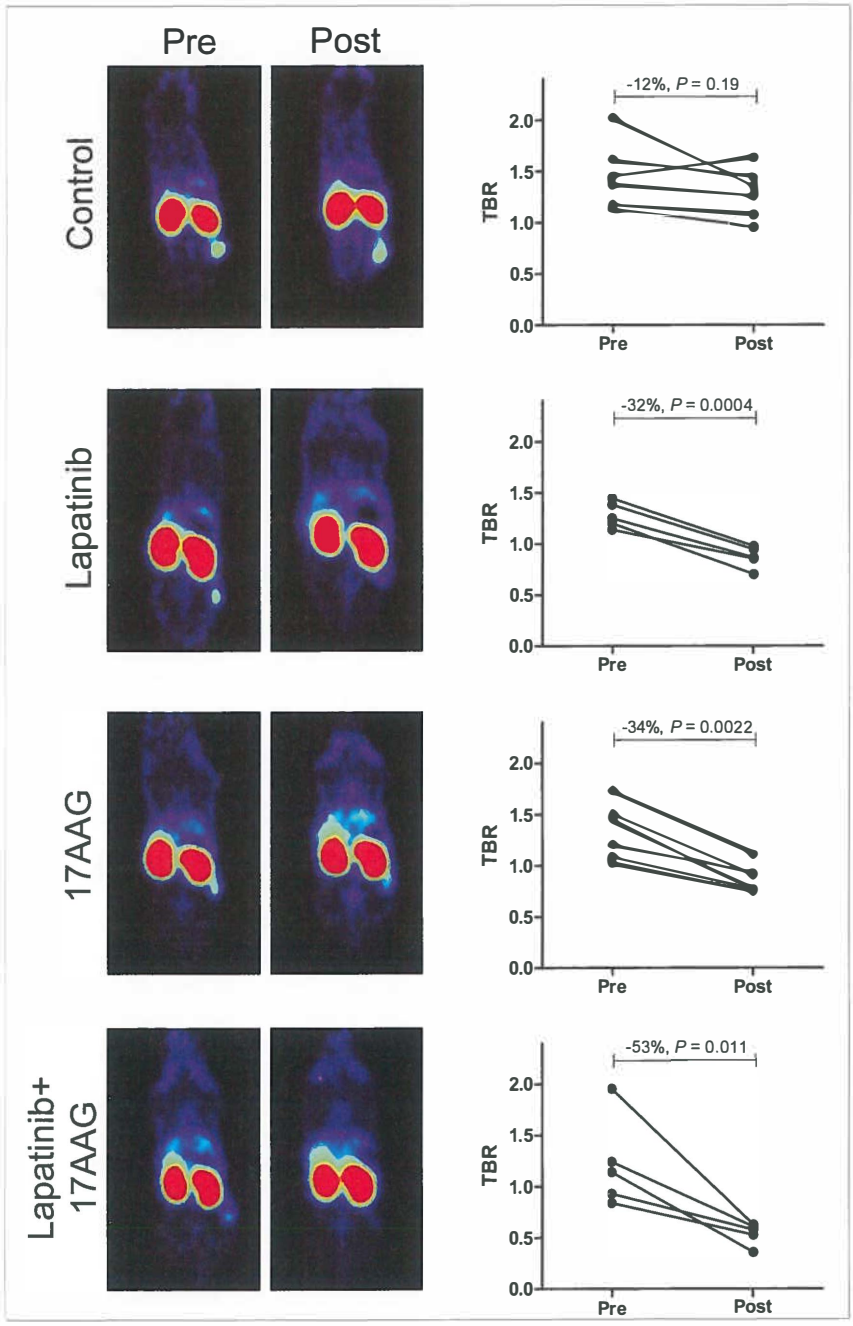

Figure 3. Representative examples of coronal ^{89}Zr-trastuzumab-F(ab')$_2$ PET images acquired pre and post treatment, and PET quantification of ^{89}Zr-trastuzumab-F(ab')$_2$ tumor-to-blood ratios (TBR) in individual mice of the different treatment groups.

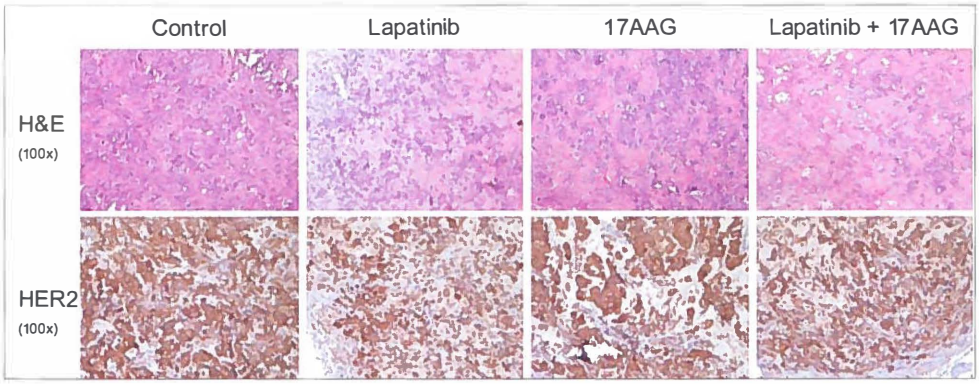

Figure 5. Representative examples of staining for hematoxylin-eosin (H&E) and HER2 in tumors from untreated mice and mice treated with lapatinib, 17AAG or lapatinib + 17AAG.

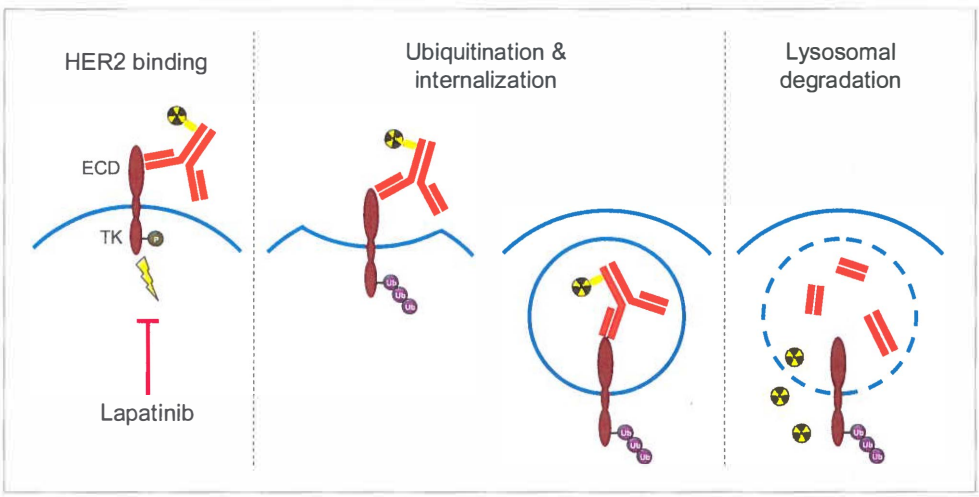

Figure 6. Proposed mechanism of tyrosine kinase triggered HER2 internalization and intracellular uptake of HER2 targeted antibody based imaging tracers and drugs. The HER2 internalization cascade is initiated by phosphorylation of the tyrosine kinase domain. Next step is ubiquitination of the HER2 intracellular domain, followed by internalization of the HER2-antibody complex in a lysosome. Within the lysosome, the HER2 bound antibody based imaging tracer (or drug) is degraded with subsequent intracellular release of the radioisotope (for radioactive tracers), the fluorescent dye (for optical tracers) or the toxin (for antibody-drug conjugates). Most of the internalized HER2 is recycled back to the tumor cell membrane. Lapatinib inhibits HER2 phosphorylation and thereby prevents the first step of the cascade, possibly resulting in hampered intracellular uptake of HER2 targeted antibody based imaging tracers and drugs.

Chapter 6A

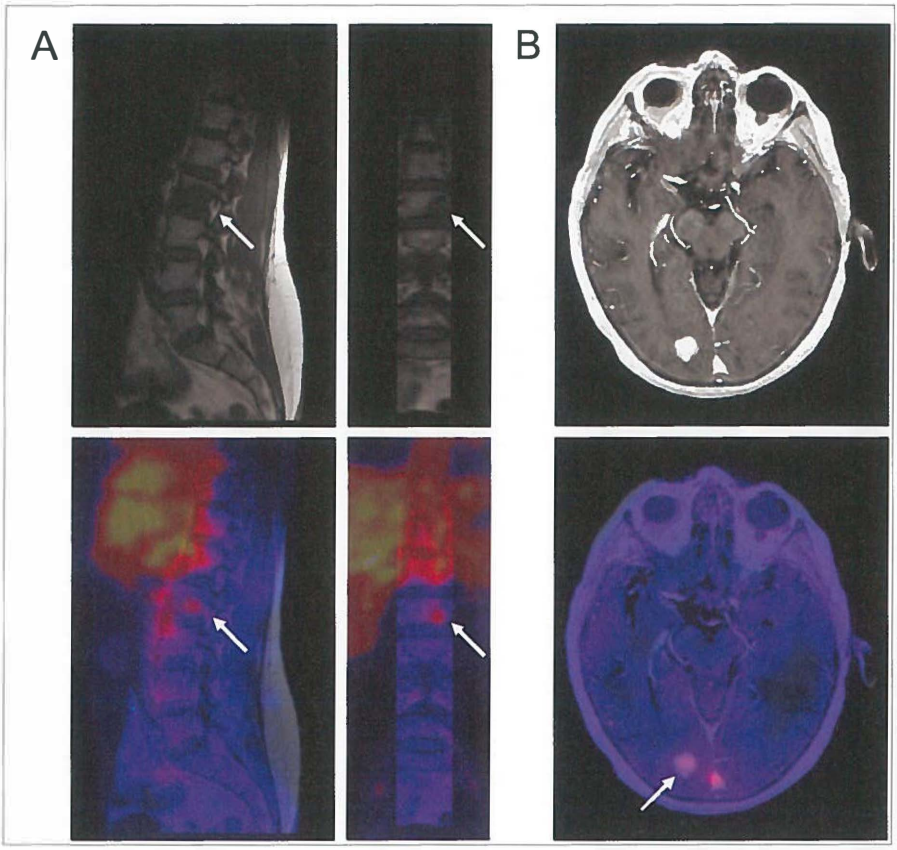

Figure 4. Examples of HER2-PET MRI fusion images. HER2 status of a vertebral metastasis known on MRI unapproachable for biopsy was revealed by ^{89}Zr-trastuzumab uptake on HER2-PET (A). Example of HER2-PET detected unknown brain lesion, which was later confirmed by MRI (B). Arrow indicates lesions.

Chapter 7

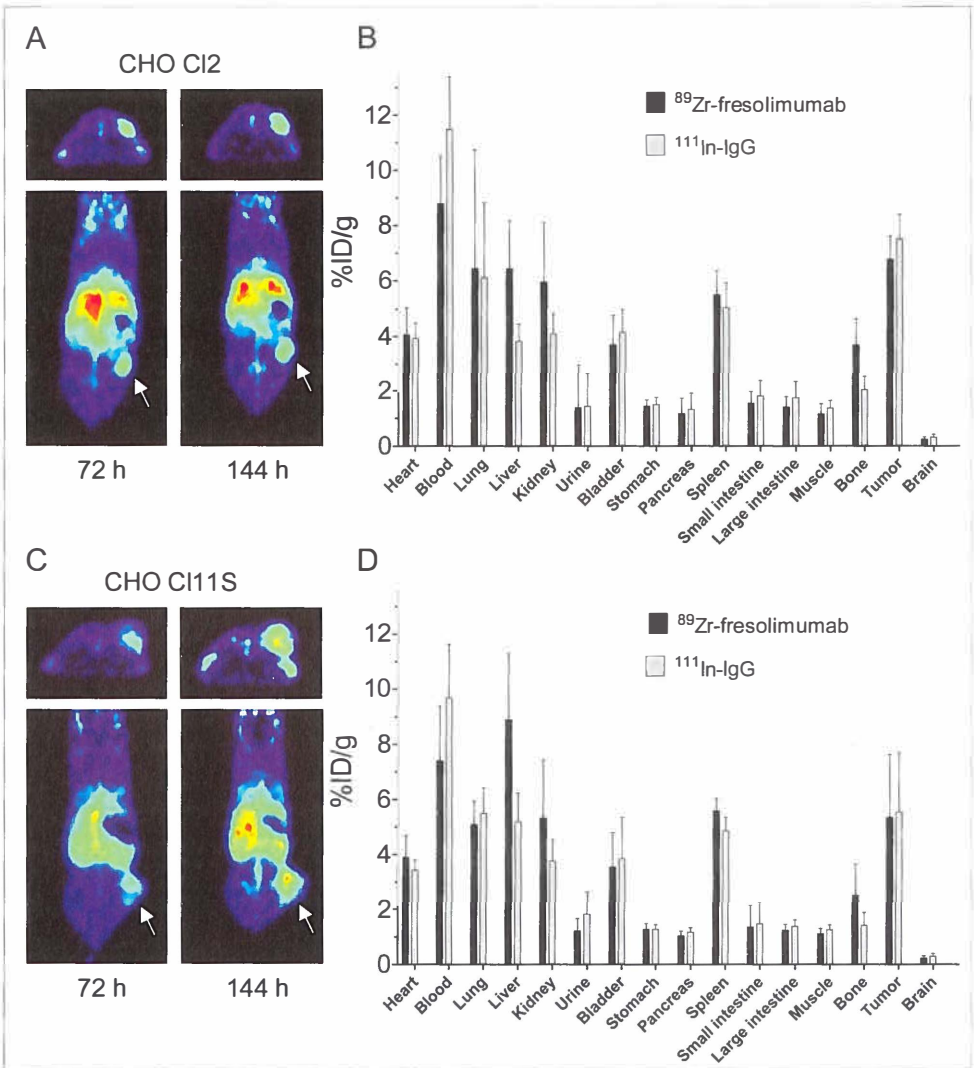

Figure 2. μPET imaging with ^{89}Zr-fresolimumab showed tumor uptake in both CHO-Cl11S and CHO-Cl2 (A and C; arrow indicates tumor). Tumor uptake and organ distribution of ^{89}Zr-fresolimumab and control ^{111}In-IgG as was quantified *ex vivo* (B and D).

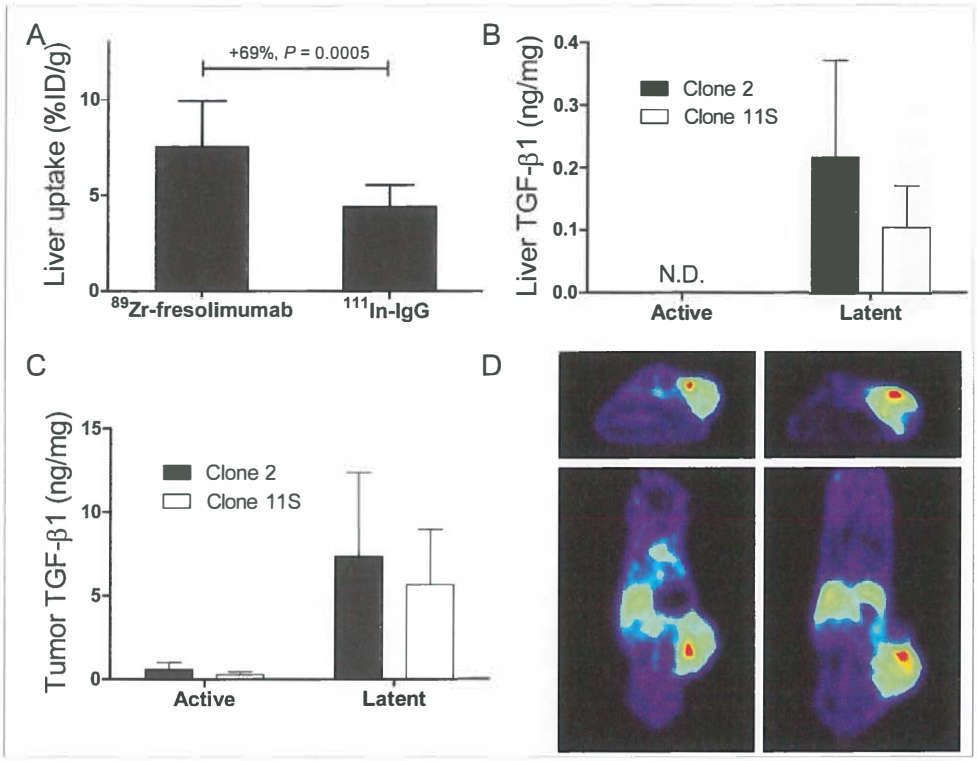

Figure 3. Liver uptake of ^{89}Zr-fresolimumab and ^{111}In-IgG in CHO xenograft mice (A). TGF-β1 levels were determined by ELISA in homogenates of liver (B) and tumor (C) tissue. Two mice with a skin ulceration at the tumor site showed locally increased uptake of ^{89}Zr-fresolimumab (represented by red areas) at the site of ulceration (D).

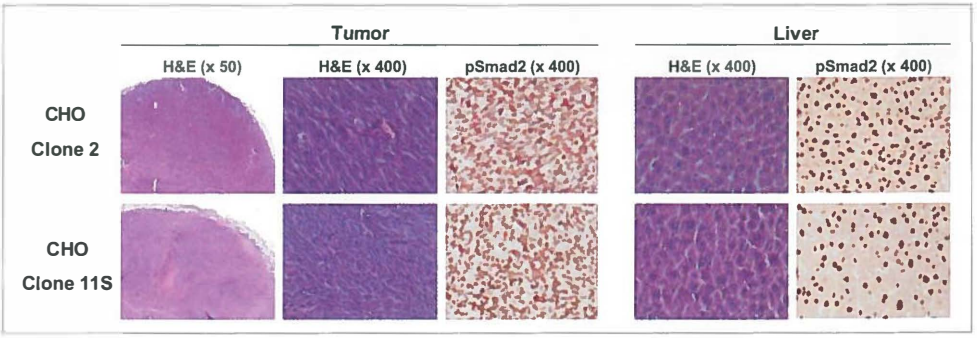

Figure 4. Histological and immunohistochemical staining for hematoxylin and eosin (H&E) and phospho-Smad2 (pSmad2) on tumor and liver material from CHO xenograft mice.

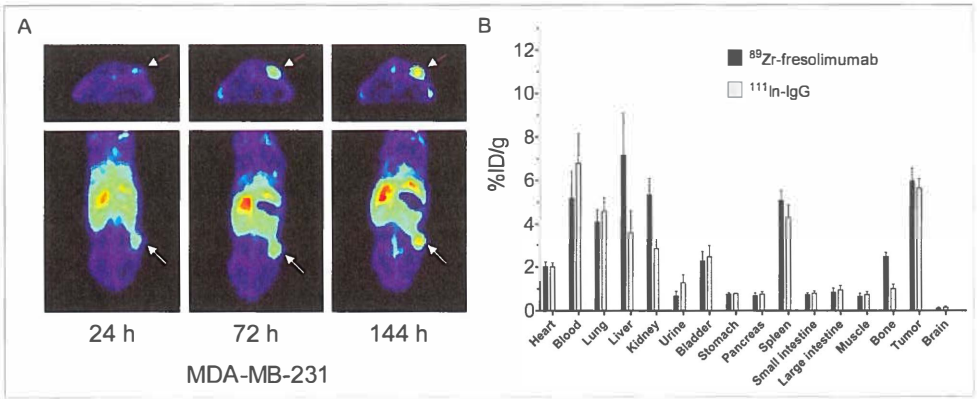

Figure 5. μPET imaging (A) and ex vivo biodistribution (B) of ^{89}Zr-fresolimumab in MDA-MB-231 xenografts.

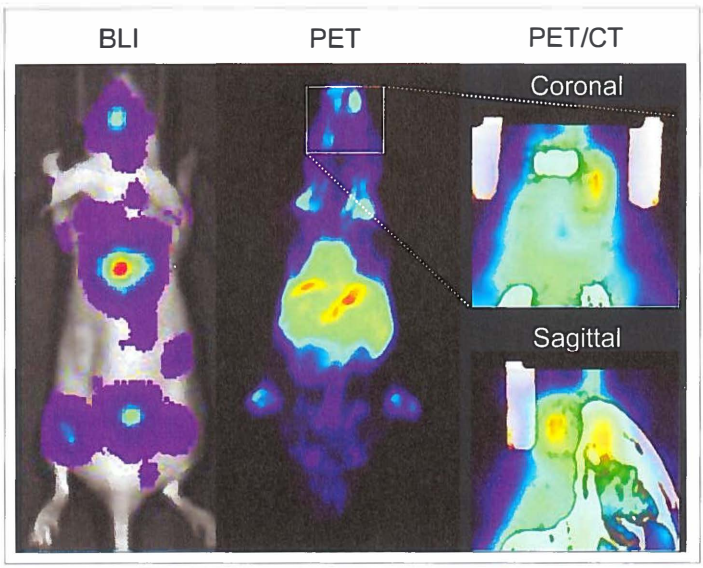

Figure 6. Representative example of bioluminescence (BLI) and μPET/CT imaging of a mouse in which bone metastatic MDA-MB-231-SCP2-luc cells were injected into the left ventricle of the heart in a disseminated model of metastasis. Metastases were visible with BLI in the jaws, skull, sternum, spine, shoulders, hips and lower limbs.

Chapter 8

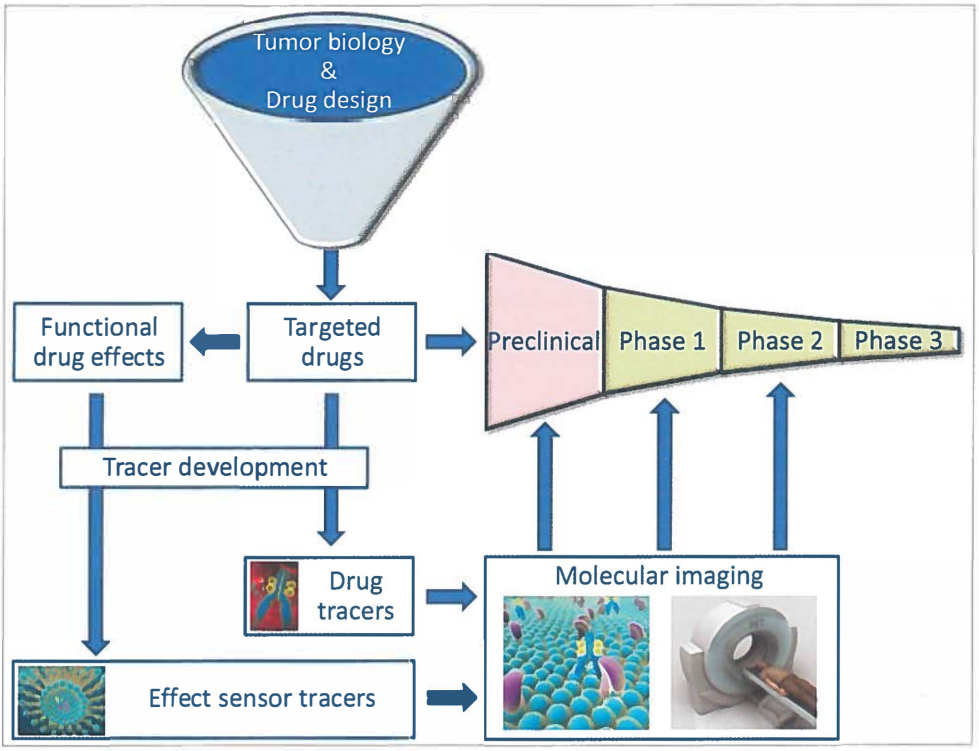

Figure 1. Flow-chart of integrating molecular imaging in drug development.